



Characterizing Ligand-Binding Domains of TRPM2 and the P2X7 Ballast Domain

Dissertation for the Acquisition of a Doctoral Degree (Dr. rer. nat.)

at the Department of Chemistry

Faculty of Mathematics, Informatics and Natural Sciences

University of Hamburg

submitted by

Simon Sander

May 2022

This work was done from December 2018 to May 2022 at the Department of Chemistry,
University of Hamburg under the supervision of Prof. Dr. Henning Tidow.

1st reviewer: Prof. Dr. Henning Tidow

2nd reviewer: Dr. Ralf Fliegert

Date of Disputation: 1st July 2022

TABLE OF CONTENTS

Abstract	I
List of publications	III
List of figures	IV
List of tables	VI
List of abbreviations	VII
1 Introduction	1
1.1 Transient receptor potential melastatin 2 (TRPM2)	1
1.1.1 TRP channels are important signal transducers	1
1.1.2 TRPM2 is involved in various physiological processes	3
1.1.3 Adenine nucleotides activate TRPM2	5
1.1.3.1 Adenosine diphosphate ribose (ADPR) is a TRPM2 agonist	5
1.1.3.2 ADPR derivatives and their effects towards TRPM2 activation	6
1.1.3.3 Does cyclic ADPR (cADPR) activate TRPM2?	7
1.1.3.4 2'-deoxy-ADPR is an endogenous TRPM2 superagonist	7
1.1.4 Overall structure of TRPM2	8
1.1.5 Nucleotide-binding sites of TRPM2	9
1.1.5.1 The NUDT9-H domain differs in function in different species	9
1.1.5.2 The MHR1/2 domain is a conserved site for channel activation	10
1.1.6 TRPM2 is regulated by Ca ²⁺	11
1.1.7 TRPM2 is influenced by Zn ²⁺	12
1.2 P2X purinoreceptor 7 (P2X7)	13
1.2.1 P2X receptors are essential for purinergic signaling	13
1.2.2 P2X7 is involved in various physiological processes	14
1.2.3 Structure of P2X7 and the activation by ATP	15

1.2.4	The C-terminal ballast domain of P2X7 is unique	17
1.2.5	P2X7 interacts with calmodulin (CaM)	18
2	Aim of the thesis	20
<hr/>		
2.1	Characterization of ligand-binding domains of TRPM2	20
2.2	Characterization of the P2X7 ballast domain	20
3	TRPM2	21
<hr/>		
3.1	Results	21
3.1.1	Expression and purification of the zebrafish MHR1/2 domain (<i>drMHR1/2</i>)	21
3.1.2	Characterization of ADPR and ADPR derivatives binding to <i>drMHR1/2</i>	22
3.1.3	The human MHR1/2 domain (<i>hsMHR1/2</i>) does not express in <i>E. coli</i>	23
3.1.4	Crystal structure of <i>drMHR1/2</i>	24
3.1.5	Characterization of a conserved Zn ²⁺ -binding domain in TRPM2	26
3.1.6	The Zn ²⁺ -binding domain is required for TRPM2 structure and function	27
3.1.7	Calmodulin (CaM) binds to <i>drMHR1/2</i>	30
3.1.8	Expression and purification of a TRPM2-CaM complex for cryo-EM	33
3.1.9	Expression, purification and characterization of the NUDT9-H domain	36
3.2	Discussion	39
3.2.1	2'-deoxy-ADPR is no superagonist of zebrafish TRPM2	39
3.2.2	cADPR and 8-Br-cADPR do not interact with TRPM2	43
3.2.3	Conserved Zn ²⁺ -binding domain in MHR1/2	45
3.2.4	TRPM2-CaM interaction	48
3.3	Perspective	50
4	P2X7	52
<hr/>		
4.1	Results	52
4.1.1	P2X7 ballast domain (P2X7BD) contains two CaM-binding regions	52
4.1.2	Expression and purification of human P2X7 ballast domain (P2X7BD)	53

4.1.3	Ca ²⁺ -CaM and GDP have opposite effects on the stability of P2X7BD	54
4.1.4	Ca ²⁺ -CaM binding disrupts the trimeric state of P2X7BD	57
4.2	Discussion	62
4.2.1	CaM-binding regions in the C-terminus of P2X7	62
4.2.2	Interaction of P2X7BD with Ca ²⁺ -CaM and GDP	63
4.3	Perspective	66
5	Material and methods	67
<hr/>		
5.1	Material	67
5.1.1	Chemicals	67
5.1.2	Bacteria and cell lines	67
5.1.3	Solutions and culture media	68
5.1.4	Plasmid vectors	69
5.2	Methods	71
5.2.1	Microbiology	71
5.2.1.1	Preparation and transformation of electrocompetent <i>E. coli</i> cells	71
5.2.1.2	Preparation and transformation of chemically competent <i>E. coli</i> cells	71
5.2.2	Molecular biology	72
5.2.2.1	Polymerase chain reaction (PCR)	72
5.2.2.2	Cloning with restriction enzymes	73
5.2.2.3	Site-directed mutagenesis	74
5.2.3	Protein expression and purification	76
5.2.3.1	Zebrafish MHR1/2 domain (<i>drMHR1/2</i>) of TRPM2	76
5.2.3.2	Human MHR1/2 domain (<i>hsMHR1/2</i>) of TRPM2	77
5.2.3.3	Calmodulin (CaM)	78
5.2.3.4	Anti-GFP nanobody	79
5.2.3.5	Full-length human TRPM2 (<i>hsTRPM2</i>)	79
5.2.3.6	Zebrafish NUDT9-H domain (<i>drNUDT9-H</i>) of TRPM2	81
5.2.3.7	Human P2X7 ballast domain (<i>hsP2X7BD</i>)	82

5.2.4	Protein characterization	83
5.2.4.1	SDS-PAGE	83
5.2.4.2	Western blot	83
5.2.4.3	Mass spectrometry (MS)	84
5.2.4.4	Analytical size-exclusion chromatography (SEC)	84
5.2.4.5	Nano differential scanning fluorimetry (nDSF)	84
5.2.4.6	Isothermal titration calorimetry (ITC)	85
5.2.4.7	Microscale thermophoresis (MST)	86
5.2.4.8	Protein cross-linking	86
5.2.5	Protein crystallization and structure determination	87
5.2.6	Hydrolase assay by high performance liquid chromatography (HPLC)	89
5.2.7	Size-exclusion chromatography small-angle X-ray scattering (SEC-SAXS)	89
5.2.8	Electron microscopy	90
5.2.9	Cell surface biotinylation assay	90
5.2.10	Electrophysiology (patch clamp)	91
5.2.11	Multiple sequence alignment	92
5.2.12	Molecular graphics	92
6	References	93
7	Safety and disposal	106
	Abstract (deutsch)	110
	Danksagung	112
	Eidesstattliche Versicherung	113

ABSTRACT

The ion channels TRPM2 (transient receptor potential melastatin 2) and P2X7 (P2X purinoreceptor 7) are key players in immunity and inflammation and are both activated by adenine nucleotides: TRPM2 by ADPR (adenosine diphosphate ribose), and P2X7 by ATP (adenosine triphosphate), respectively.

TRPM2 is crucial for intracellular Ca^{2+} signaling and contains two nucleotide binding domains: N-terminal MHR1/2 (TRPM homology region 1/2), that harbors a conserved ADPR binding site, and C-terminal NUDT9-H (NUDT9-homology), which has different functionalities in different TRPM2 orthologues. The mechanisms behind the function of these domains are not fully elucidated.

In this dissertation, both domains were expressed and purified in isolated, soluble forms and biophysically characterized. Further experiments with MHR1/2 from zebrafish TRPM2 (*drMHR1/2*) showed that the ADPR derivatives 2'-deoxy-ADPR (a superagonist of human TRPM2) and 8-Br-ADPR (an antagonist of human TRPM2) bind to the isolated domain while cADPR (cyclic ADPR) and 8-Br-cADPR do not, although both cyclic substances had been previously suggested to interact with TRPM2. Additionally, the results demonstrated that 2'-deoxy-ADPR is no superagonist of zebrafish TRPM2. A crystal structure of isolated *drMHR1/2* revealed a novel Zn^{2+} -binding site that is conserved within the TRPM family and essential for structural integrity and function of TRPM2, as shown by electrophysiology. Moreover, calmodulin (CaM) was shown to bind to *drMHR1/2*, confirming a known IQ-like motif from human TRPM2.

P2X7 is an essential component of purinergic signaling and comprises a unique ballast domain (P2X7BD) that is crucial for the cytotoxic action of the receptor but not involved in channel gating. Its interplay with the ligands GDP (guanosine diphosphate) and CaM as well as the modulatory role for P2X7 function are not completely understood.

Here, two putative CaM-binding regions were identified in P2X7BD by a peptide-based binding approach and isolated human P2X7BD was shown to bind Ca^{2+} -CaM. While this interaction destabilized the domain and disrupted its trimeric state, as shown by SAXS, GDP stabilized P2X7BD. This indicates that both ligands reversibly bind to P2X7BD in an equilibrium, providing a possible framework for the regulation of full-length P2X7.

Taken together, this dissertation revealed novel characteristics of important ligand-binding domains of TRPM2 and P2X7, respectively, which paves the way for future investigations regarding functional implications for the respective full-length channels.

LIST OF PUBLICATIONS

Niebling, S., Burastero, O., Bürgi, J., Günther, C., Defelipe, L.A., **Sander, S.**, Gattkowsky, E., Anjanappa, R., Wilmanns, M., Springer, S., Tidow, H., García-Alai, M. (2021). FoldAffinity: binding affinities from nDSF experiments. **Scientific Reports**, *11*, 9572.

Gattkowsky, E., Rutherford, T.J., Möckl, F., Bauche, A., **Sander, S.**, Fliegert, R., and Tidow, H. (2021). Analysis of ligand binding and resulting conformational changes in pyrophosphatase NUDT9. **FEBS Journal**, *288*, 6769-6782.

Kehlenbeck, D., Traore, D.A.K., Josts, I., **Sander, S.**, Moulin, M., Haertlein, M., Prevost, S., Forsyth, V.T., and Tidow, H. (2021). Cryo-EM structure of MsbA in saposin-lipid nanoparticles (Salipro) provides insights into nucleotide coordination. **FEBS Journal**, *289*, 2959-2970.

Riekehr, W.M., **Sander, S.**, Pick, J., Tidow, H., Bauche, A., Guse, A.H. and Fliegert, R. (2022). cADPR does not activate TRPM2. **International Journal of Molecular Sciences**, *23*, 3163.

Sander, S., Pick, J., Gattkowsky, E., Fliegert, R. and Tidow, H. (2022). The crystal structure of TRPM2 MHR1/2 domain reveals a conserved Zn²⁺-binding domain essential for structural integrity and channel activity. **Protein Science**, *31*, 1-12.

Sander, S., Müller, I., García-Alai, M., Nicke, A., Tidow, H. (2022). New insights into P2X7 regulation: Ca²⁺-calmodulin and GDP bind to soluble P2X7 ballast domain. **Unpublished**, under revision.

LIST OF FIGURES

Figure 1.1: Common domain architecture of the TRPM family.	3
Figure 1.2: Adenine nucleotides in the context of TRPM2.	5
Figure 1.3: Structure of tetrameric human TRPM2 in the apo state.	8
Figure 1.4: Common domain architecture of the P2X family.	14
Figure 1.5: Structure of trimeric rat P2X7 in the ATP-bound state.	16
Figure 3.1: Purification and thermal stability of <i>drMHR1/2</i> .	21
Figure 3.2: ADPR and 2'-deoxy-ADPR bind to <i>drMHR1/2</i> .	22
Figure 3.3: Biophysical characterization of ADPR derivatives binding to <i>drMHR1/2</i> .	23
Figure 3.4: The human MHR1/2 domain does not express in <i>E. coli</i> .	24
Figure 3.5: Crystallization and crystal structure of <i>drMHR1/2</i> .	25
Figure 3.6: Novel Zn ²⁺ -binding domain in <i>drMHR1/2</i> .	26
Figure 3.7: Zn ²⁺ -binding domain in MHR1/2 is conserved in TRPM channels.	27
Figure 3.8: Zn ²⁺ -binding domain is important for <i>drMHR1/2</i> protein integrity.	28
Figure 3.9: Zn ²⁺ -binding domain is important for <i>hsTRPM2</i> protein integrity.	29
Figure 3.10: Zn ²⁺ -binding domain is important for <i>hsTRPM2</i> channel activity.	29
Figure 3.11: Ca ²⁺ -CaM binds to <i>drMHR1/2</i> independently of ADPR or 2'-deoxy-ADPR.	30
Figure 3.12: Ca ²⁺ -CaM binds to <i>drMHR1/2</i> which leads to an increase in size.	31
Figure 3.13: SAXS analysis of the <i>drMHR1/2</i> -CaM interaction.	32
Figure 3.14: Expression tests of <i>hsTRPM2</i> in adherent HEK293S GnTI- cells.	33
Figure 3.15: BacMam virus production and <i>hsTRPM2</i> expression.	34
Figure 3.16: Purification of <i>hsTRPM2</i> -CaM complex.	35
Figure 3.17: Analysis of <i>hsTRPM2</i> by negative-stain electron microscopy.	35
Figure 3.18: Purification and thermal stability of <i>drNUDT9-H</i> .	36
Figure 3.19: ADPR and 2'-deoxy-ADPR do not bind to isolated <i>drNUDT9-H</i> .	37
Figure 3.20: HPLC analysis of hydrolase assay with <i>drNUDT9-H</i> .	38
Figure 3.21: The 2'-hydroxyl group of ADPR is exposed in MHR1/2.	40
Figure 3.22: The 2'-hydroxyl group of ADPR is not exposed in <i>hsNUDT9-H</i> .	41
Figure 3.23: 8-Br-cADPR and 8-Br-ADPR both fit into the density of EMDB 20482.	44
Figure 3.24: Importance of Zn ²⁺ -binding site for MHR1/2 stability and ADPR binding.	46

Figure 4.1: CaM-binding regions within the P2X7 ballast domain.	53
Figure 4.2: Expression and purification of human P2X7BD.	54
Figure 4.3: P2X7BD is stabilized by GDP and destabilized by Ca ²⁺ -CaM.	55
Figure 4.4: The opposite effects of GDP and Ca ²⁺ -CaM are concentration dependent.	56
Figure 4.5: GDP and Ca ²⁺ -CaM interact with P2X7BD, apo-CaM does not.	57
Figure 4.6: Ca ²⁺ -CaM cross-linking to P2X7BD.	58
Figure 4.7: CaM binds to P2X7BD which leads to a decrease in size.	59
Figure 4.8: SEC-SAXS analysis of the P2X7BD-CaM interaction.	60
Figure 4.9: SAXS <i>ab initio</i> reconstructions of P2X7BD and P2X7BD-CaM complex.	61
Figure 4.10: Putative CaM-binding regions of P2X7BD.	63
Figure 4.11: Molecular models of P2X7BD.	64
Figure 4.12: Model for ligand binding to P2X7BD.	65

LIST OF TABLES

Table 3.1: SEC-SAXS analysis of the <i>drMHR1/2</i> -CaM interaction.	32
Table 4.1: P2X7BD-GDP binding affinities at different Ca ²⁺ -CaM concentrations.	56
Table 4.2: Mass spectrometric analysis of tryptic digest of bands after cross-linking.	58
Table 4.3: SEC-SAXS analysis of the P2X7BD-CaM interaction.	60
Table 5.1: Expression systems used in this study.	67
Table 5.2: Composition of solutions and culture media.	68
Table 5.3: Plasmid vectors used in this study.	70
Table 5.4: General PCR reaction set-up.	72
Table 5.5: General PCR program.	72
Table 5.6: General DNA digest reaction.	73
Table 5.7: General ligation reaction set-up.	74
Table 5.8: General mutagenesis PCR reaction set-up.	75
Table 5.9: General mutagenesis PCR program.	75
Table 5.10: General mutagenesis ligation reaction set-up.	76
Table 5.11: Crystallographic data collection and refinement statistics of <i>drMHR1/2</i> .	88
Table 7.1: Hazardous and toxic chemicals.	106

LIST OF ABBREVIATIONS

ADP	Adenosine 5'-diphosphate
ADPR	Adenosine 5'-diphosphate ribose
AMP	Adenosine 5'-monophosphate
ART	ADP-ribosyltransferase
ATP	Adenosine 5'-triphosphate
BD	Ballast domain
BSA	Bovine serum albumin
cADPR	Cyclic adenosine diphosphate ribose
CaM	Calmodulin
CMV	Cytomegalovirus
CRC	Collaborative Research Center
cryo-EM	Cryogenic electron microscopy
DDM	Dodecyl- β -D-maltopyranoside
DMEM	Dulbecco's Modified Eagle's Medium
DMSO	Dimethyl sulfoxide
DNA	Deoxyribonucleic acid
<i>dr</i>	<i>Danio rerio</i> (zebrafish)
DSS	Disuccinimidyl suberate
<i>E. coli</i>	<i>Escherichia coli</i>
EC ₅₀	Half maximal effective concentration
ECD	Extracellular domain
EDTA	Ethylenediaminetetraacetic acid
EGFP	Enhanced green fluorescent protein
EGTA	Ethylene glycol-bis(β -aminoethyl ether)-N,N,N',N',-tetraacetic acid
FBS	Fetal bovine serum
GDN	Glyco-diosgenin
GDP	Guanosine 5'-diphosphate
GnTI	N-acetyl-glucosaminyltransferase I
GST	Glutathione S-transferase

LIST OF ABBREVIATIONS

HEPES	4-(2-hydroxyethyl)-1-piperazineethanesulfonic acid
<i>hs</i>	<i>Homo sapiens</i> (human)
IDPR	Inosine 5'-diphosphate ribose
IMAC	Immobilized metal affinity chromatography
IPTG	Isopropyl β -D-1-thiogalactopyranoside
ITC	Isothermal titration calorimetry
kb	Kilo base pair (= 1,000 base pairs)
K _D	Dissociation constant
kDa	Kilodaltons (= 1,000 Daltons = 1,000 g/mol)
LB	Lysogeny Broth
LC	Liquid chromatography
LTRPC2	Long transient receptor potential channel 2 (old name for TRPM2)
MBP	Maltose binding protein
MHR	TRPM homology region
MS	Mass spectrometry
MST	Microscale thermophoresis
NAD ⁺	Nicotinamide adenine dinucleotide
nDSF	Nano differential scanning fluorimetry
NMDG	N-methyl-D-glucamine
NUDT9	Nudix hydrolase 9
NUDT9-H	NUDT9-homologous
<i>nv</i>	<i>Nematostella vectensis</i> (starlet sea anemone)
P2X7	P2X purinoreceptor 7
P2X7BD	P2X7 ballast domain
PAGE	Polyacrylamide gel electrophoresis
PARG	Poly-ADPR glycohydrolase
PARP	Poly-ADPR polymerase
PBS	Phosphate-buffered saline
PCR	Polymerase chain reaction
PDB	Protein data bank

LIST OF ABBREVIATIONS

PMSF	Phenylmethylsulfonyl fluoride
PVDF	Polyvinylidene fluoride
ROS	Reactive oxygen species
SAD	Single-wavelength anomalous dispersion
SAXS	Small-angle X-ray scattering
SDS	Sodium dodecyl sulfate
SEC	Size-exclusion chromatography
SeMet	Selenomethionine
TARG	Terminal ADPR protein glycohydrolase
TB	Terrific Broth
TBST	Tris-buffered saline with Tween-20
TEV	Tobacco Etch Virus protease
TMD	Transmembrane domain
Tris	Tris(hydroxymethyl)aminomethane
TRP	Transient receptor potential
TRPM	Transient receptor potential melastatin
wt	wild type

1 INTRODUCTION

This thesis is part of the collaborative research center ‘Adenine Nucleotides in Immunity and Inflammation’ (CRC1328, financed by the German Research Foundation). Adenine nucleotides, ubiquitous and essential signaling molecules, are involved in regulating nearly all central processes in biology and medicine, including cell-cell communication and intracellular signaling (<http://sfb1328.de>). In this study, two proteins that are activated by specific adenine nucleotides will be discussed in greater detail: transient receptor potential melastatin 2 (TRPM2), which is activated by adenosine diphosphate ribose (ADPR); and P2X purinoreceptor 7 (P2X7), which is activated by adenosine triphosphate (ATP). TRPM2 is essential for intracellular Ca^{2+} signaling and P2X7 plays a central role in mediating extracellular ATP signaling. Both TRPM2 and P2X7 will be introduced in this chapter.

1.1 Transient receptor potential melastatin 2 (TRPM2)

1.1.1 TRP channels are important signal transducers

The 2021 Nobel Prize in Physiology or Medicine was awarded to David Julius and Ardem Patapoutian for their “discoveries of receptors for temperature and touch” (Ernfors et al., 2021). Research on how physical sensation is perceived and transmitted had been of interest since the 17th century, when the philosopher and scientist René Descartes laid the foundation for understanding how reflexes work (DeLeo, 2006). In the 20th century three Nobel Prizes within this field (1906, 1932, 1944) shed light on different types of nerves in the skin that get activated by different physical stimuli. However, the molecular mechanisms were not understood until Julius and Patapoutian identified the transducers responsible for sensing temperature and touch (Ernfors et al., 2021). The first prominent example was the capsaicin receptor, which is activated by an increase in temperature and elicits pain through sensory neurons upon binding of its ligand capsaicin, the ingredient that is responsible for chili peppers being spicy (Caterina et al., 1997). This receptor is now called transient receptor potential vanilloid 1 (TRPV1) and belongs to the class of transient receptor potential (TRP) ion channels.

The TRP superfamily is a group of conserved integral membrane proteins in eukaryotes and can be divided into seven subfamilies: TRPC (“canonical”), TRPV (“vanilloid”), TRPM (“melastatin”), TRPP (“polycystin”), TRPML (“mucolipin”), TRPA (“ankyrin”) and TRPN (“no mechanoreceptor potential C”). They all share a common core architecture of six putative transmembrane helices forming a tetrameric cation pore (reviewed in: (Pedersen et al., 2005; Ramsey et al., 2006; Samata et al., 2018; Venkatachalam and Montell, 2007)). Since TRP channels have many roles in sensory perception as well as in cellular physiology and are predominantly located on the cell surface, they are associated with many diseases and drug discovery efforts (Koivisto et al., 2022).

The TRPM subfamily is the largest within in the TRP superfamily. There are eight members (TRPM1 to TRPM8) which are either permeable to Ca^{2+} or indirectly influence cellular Ca^{2+} signaling. TRPM channels are ubiquitously expressed in various tissues and are crucial for many physiological processes such as the immune response (Schmitz and Perraud, 2005), apoptosis (TRPM2 (McNulty and Fonfria, 2005)), the response to oxidative stress (TRPM2 (Simon et al., 2013)), cardiovascular function (TRPM4 (Abriel et al., 2012)), taste transduction (TRPM5 (Pérez et al., 2002)), Mg^{2+} homeostasis (TRPM6 and TRPM7 (Montell, 2003)), as well as temperature sensing and regulation (TRPM8 (McKemy et al., 2002), TRPM2 (Song et al., 2016; Tan and McNaughton, 2016)). Consequently, they are central targets of many drug discovery efforts (Abriel et al., 2012; Sun et al., 2015; Vennekens et al., 2018). Multiple different factors influence their channel activity, for example voltage, temperature, small molecules, lipids, or varying ion concentrations (reviewed in (Huang et al., 2020)). From a structural point of view, all members of the TRPM family are tetramers with a common domain architecture: N-terminal TRPM homology regions (MHR1-4), six transmembrane helices, a TRP helix, a coiled-coil domain, and a C-terminal domain with characteristic traits that is different for every member (Figure 1.1). The serine/threonine kinase domains of TRPM6 and TRPM7, as well as the NUDT9-H (NUDT9-homologous) domain of TRPM2 are C-terminal domains of special interest since their sequences indicate an enzymatic function (Scharenberg, 2005). The NUDT9-H domain has been studied intensively by many groups since it was first discovered as a part of TRPM2 in 2001 (Perraud et al., 2001).

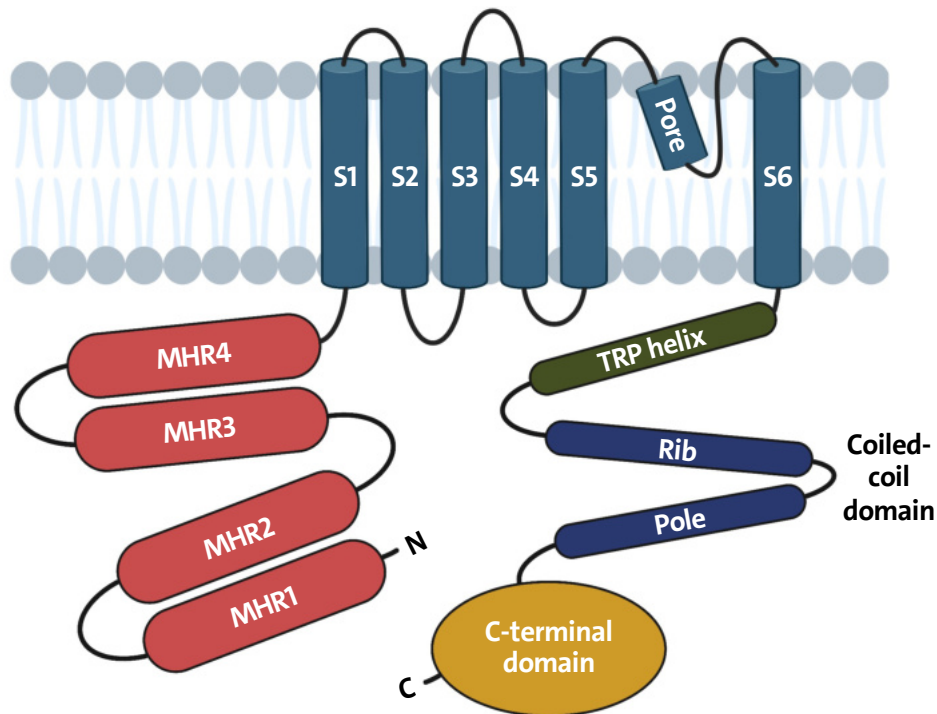


Figure 1.1: Common domain architecture of the TRPM family. From N-terminus to C-terminus (both intracellular): four TRPM homology regions (MHR1-4), six transmembrane helices (S1-6) with the pore formed by the loop between S5 and S6, TRP helix, coiled-coil domain consisting of rib and pole helices and C-terminal domain which is unique for every TRPM member. Created with BioRender.com, adapted from (Huang et al., 2020).

1.1.2 TRPM2 is involved in various physiological processes

TRPM2 is a Ca^{2+} -permeable, non-selective cation channel. It was originally described under the names TRPC7 (Nagamine et al., 1998) and LTRPC2 (Long transient receptor potential channel 2, (Harteneck et al., 2000)). The above-mentioned C-terminal NUDT9-H domain, which exhibits strong homology to the enzyme NUDT9 (Perraud et al., 2001), was one of the reasons why TRPM2 received broad scientific interest. It will be introduced in more detail below alongside a second nucleotide-binding domain of TRPM2, the N-terminal MHR1/2 (see 1.1.5).

TRPM2 is widely expressed in most peripheral tissue regions, with the highest expression level in the brain and relatively high expression levels in macrophage cells and bone marrow (Fonfria et al., 2006). Upon activation by adenine nucleotides (see 1.1.3) and other factors (see 1.1.6 and 1.1.7) the channel opens allowing the permeation of Na^+ , K^+ and Ca^{2+} (Perraud et al., 2001; Sano et al., 2001). Since the resting Ca^{2+} concentration inside the cytoplasm of a typical vertebrate cell (~ 100 nM) is 10,000 times lower than in

the extracellular milieu (~1 mM), TRPM2 activation leads to Ca²⁺ influx into the cell, initiating complex intracellular signaling pathways (Bagur and Hajnóczy, 2017). Although the protein is mainly located at the plasma membrane, it was also found to function as a lysosomal Ca²⁺ release channel (Lange et al., 2009).

Due to its participation in Ca²⁺ mobilization, TRPM2 is involved in diverse physiological processes, for instance cell death through oxidative stress (Hara et al., 2002; Hecquet et al., 2014; Wehage et al., 2002). The connection of its activity with oxidative stress, especially the sensitivity towards reactive oxygen species (ROS, e.g. hydrogen peroxide), explains why it further plays substantial roles in immunity and inflammation. For example, hydrogen peroxide-induced Ca²⁺ influx by TRPM2 into human monocytes leads to the production of chemokines (Yamamoto et al., 2008). TRPM2 is also essential for the production of other inflammatory cytokines upon contact with lipopolysaccharides, the major outer membrane component of gram-negative bacteria (Wehrhahn et al., 2010). Moreover, the immune response of TRPM2-deficient mice is extremely inefficient compared to wild type mice (Knowles et al., 2011). Besides the involvement in immunity and inflammation, the TRPM2 channel is highly expressed in many cancer entities, leading to the idea that it promotes tumor survival (Park et al., 2016). Inhibition of TRPM2 has been shown to improve sensitivity to chemotherapeutic agents and to enhance cell death in various malignancies, for example neuroblastoma (Bao et al., 2016), leukemia (Klumpp et al., 2016), and gastric cancer (Almasi et al., 2018). Furthermore, TRPM2 is important for pancreatic β -cell function as well as insulin secretion (Uchida and Tominaga, 2014), and it acts as a thermal sensor, a trait that many ion channels of the TRP superfamily exhibit. Experiments with TRPM2-deficient mice indicated that the channel is responsive to a temperature signal in the range between 23°C and 38°C (Tan and McNaughton, 2016). Another study showed that TRPM2 is not only involved in sensing temperature but also exhibits a regulatory function by limiting the response to elevated body temperatures (Song et al., 2016). Due to its diverse physiological roles, TRPM2 is considered a promising therapeutic target for various diseases (Zhang et al., 2020).

1.1.3 Adenine nucleotides activate TRPM2

Many neurodegenerative diseases are caused by enduring oxidative stress within the brain and the nervous system (Halliwell, 2006). As mentioned above, TRPM2 activation is connected to oxidative stress through ROS, explaining why the channel contributes to the molecular progression of these diseases. Adenine nucleotides (Figure 1.2), especially adenosine diphosphate ribose (ADPR), act as secondary messengers within cells, linking ROS to TRPM2 activation (Kühn et al., 2005).

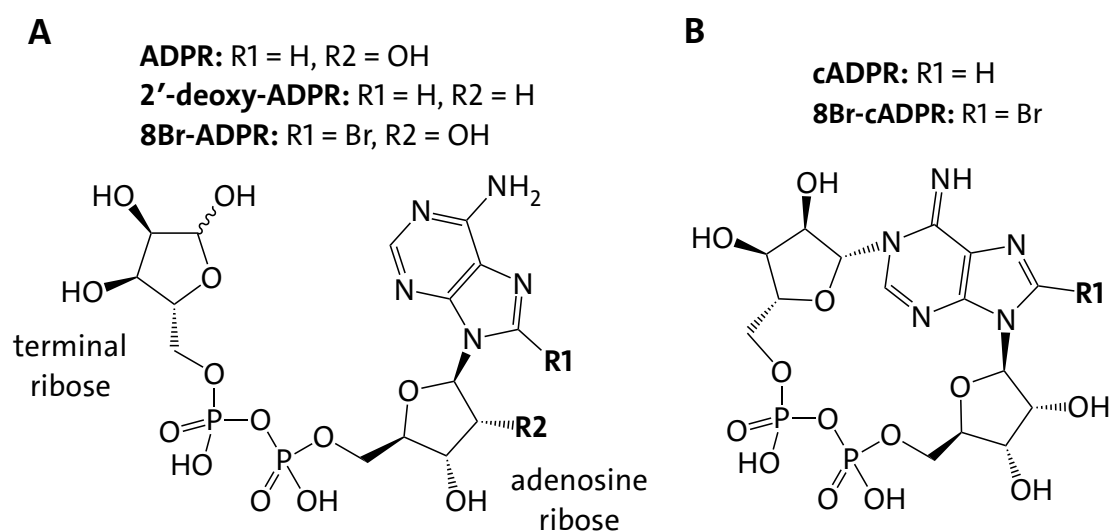


Figure 1.2: Adenine nucleotides in the context of TRPM2. (A) Structural formulas of ADPR, 2'-deoxy-ADPR and 8-Br-ADPR. (B) Structural formulas of the cyclic nucleotides cADPR and 8-Br-cADPR.

1.1.3.1 Adenosine diphosphate ribose (ADPR) is a TRPM2 agonist

ADPR (Figure 1.2 A) is a cellular nucleotide consisting of an adenine nucleobase, a ribose (“adenosine ribose”, attached to the adenine moiety), a pyrophosphate bridge, and a second ribose (“terminal ribose”, attached to the pyrophosphate bridge). It can be generated by the multifunctional enzyme CD38 through hydrolysis of the essential redox coenzyme nicotinamide adenine dinucleotide (NAD⁺) (Howard et al., 1993; Zocchi et al., 1993). Free cellular ADPR can also be derived from post-translational poly-ADPR modifications which play an important role in the regulation of many critical signaling pathways (Cohen and Chang, 2018). Members of the ADP-ribosyltransferase (ART) superfamily assemble poly-ADPR chains by the consecutive attachment of ADPR monomers onto proteins using NAD⁺ as a precursor (Koch-Nolte et al., 2001). Poly-ADPR

polymerases (PARPs), as members of the ART superfamily, are crucial for DNA damage response, base-excision repair, and DNA strand break pathways (Schiewer and Knudsen, 2014). The poly-ADPR glycohydrolase (PARG) and the terminal ADPR protein glycohydrolase (TARG) produce free ADPR by catalyzing the hydrolysis of poly-ADPR chains (Nikiforov et al., 2015). The PARP/PARG pathway is activated by oxidative stress and the resulting DNA damage. This connects the production of free ADPR with rising levels of ROS (Blenn et al., 2011; Buelow et al., 2008).

ADPR at micromolar cytosolic concentrations ($EC_{50} \sim 1 \mu\text{M}$ - $90 \mu\text{M}$ (Faouzi and Penner, 2014)) specifically activates TRPM2 and consequently triggers Ca^{2+} entry into cells that express the protein (Perraud et al., 2001). TRPM2 contains different ADPR binding sites (see 1.1.5). The Ca^{2+} ions entering the cell are an additional cofactor, providing positive feedback to maintain an open channel (see 1.1.6). Taken together, the agonistic effects of ADPR and Ca^{2+} form the basis of the molecular pathway for TRPM2 activation. A direct effect of ROS on TRPM2 is unlikely as shown by inside-out patch clamp studies with hydrogen peroxide (Tóth and Csanády, 2010).

1.1.3.2 ADPR derivatives and their effects towards TRPM2 activation

Besides ADPR, the TRPM2 channel can also be activated by synthetic ADPR derivatives as long as they contain the terminal ribose (Fliegert et al., 2017a). It was shown that small structural modifications within the ADPR molecule can cause drastic changes in agonist activity. The removal of hydroxyl groups from the terminal ribose for example leads to a loss of the agonistic effect. The resulting derivatives are antagonists of ADPR-dependent TRPM2 activation (Baszczyński et al., 2019). Furthermore, the introduction of an 8-bromo substituent at the adenine moiety (8-Br-ADPR, Figure 1.2 A) also generates a TRPM2 antagonist (Partida-Sanchez et al., 2007). Replacement of the pyrophosphate bridge of ADPR by a phosphonoacetate linker leads to ADPR analogues with neither agonist nor antagonist activity, revealing the importance of the pyrophosphate motif for TRPM2 activation (Baszczyński et al., 2020).

1.1.3.3 Does cyclic ADPR (cADPR) activate TRPM2?

Cyclic ADPR (cADPR, Figure 1.2 B) is a physiological ADPR derivative which can be generated by CD38 as an intermediate between NAD⁺ and ADPR (Howard et al., 1993; Zocchi et al., 1993). It acts as a second messenger releasing Ca²⁺ from intracellular stores via the ryanodine receptor (Galione et al., 1991; Ogunbayo et al., 2011). Various studies proposed that cADPR is also a direct modulator of TRPM2 activation (Kolisek et al., 2005; Togashi et al., 2006; Yu et al., 2019). Structural studies have shown that ADPR binds to one of the nucleotide binding sites of TRPM2 in a horseshoe-like conformation, which is similar to the cyclic structure of cADPR (Huang et al., 2018), further supporting this idea. However, it was also shown that commercial cADPR is often contaminated with ADPR. This suggests that cADPR does not bind to and activate TRPM2, explaining the observed agonistic effects which are abolished with purified cADPR (Heiner et al., 2006; Tóth and Csanády, 2010). Nevertheless, the cADPR antagonist 8-Br-cADPR (Figure 1.2 B) was identified to bind to TRPM2 in a recent structure (Huang et al., 2019). This could imply that cADPR binds in the same cavity as 8-Br-cADPR and activates the channel. Thus, the role of cADPR for TRPM2 activation is still controversially discussed.

1.1.3.4 2'-deoxy-ADPR is an endogenous TRPM2 superagonist

In contrast to the terminal ribose and the pyrophosphate bridge of ADPR, the adenosine ribose is more permissive to modifications. The resulting molecules maintain agonistic activity towards TRPM2 (Fliegert et al., 2017b; Moreau et al., 2013). The introduction of a phosphate group at the 2' position of the adenosine ribose for instance results in the partial agonist ADPR-2'-phosphate (Tóth et al., 2015). Another prominent example is 2'-deoxy-ADPR (Figure 1.2 A), which lacks the hydroxyl group at the 2' position. It proved to be an even better agonist (a superagonist) of human TRPM2 than ADPR by inducing ~10-fold higher currents in whole-cell patch clamp experiments. This effect is due to a decreased rate of channel inactivation as well as a higher open probability. Furthermore, since 2'-deoxy-ADPR was endogenously detected in Jurkat T lymphocytes, it may act as a second messenger molecule in cells, activating TRPM2 in different physiological contexts compared to ADPR (Fliegert et al., 2017b).

1.1.4 Overall structure of TRPM2

Structurally, TRPM2 shares the common TRPM domain architecture (cf. Figure 1.1) with the addition of a unique C-terminal NUDT9-H domain (see 1.1.5.1). The physiological fold within biological membranes comprises four subunits (171 kDa each) forming a functioning homotetrameric ion channel. To date, structures of the human (Huang et al., 2019; Wang et al., 2018; Yu et al., 2021), zebrafish (Huang et al., 2018; Yin et al., 2019a) and starlet sea anemone (Zhang et al., 2018) orthologues have been solved by cryogenic electron microscopy (cryo-EM). This method, for which small amounts of purified sample are flash-frozen and subsequently analyzed in a transmission electron microscope, allows structure determination at near-atomic resolution (Kuhlbrandt, 2014). The overall architecture of TRPM2 (Figure 1.3, PDB: 6PUO (Huang et al., 2019)) consists of four layers: transmembrane domain (TMD), MHR3/4, MHR1/2 and NUDT9-H. The characteristic TRP helix is located at the interface between the TMD and the intracellular MHR3/4. The ion-conducting pore in the TMD is formed by a loop (P-loop) next to the pore helix interacting with the lower end of the transmembrane helix S6.

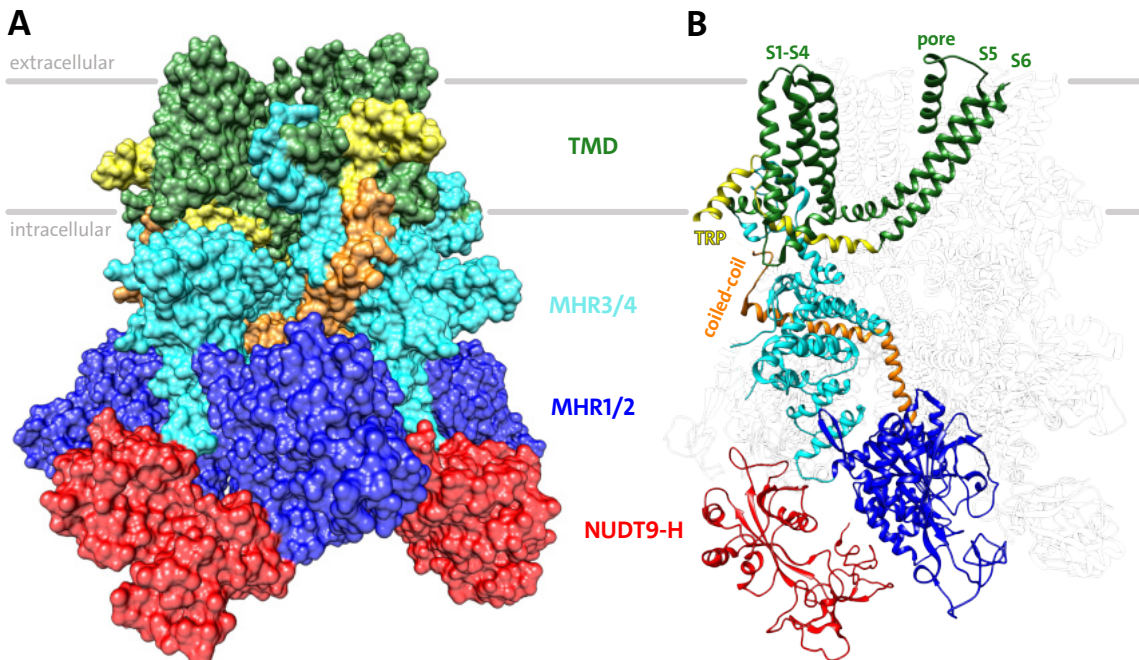


Figure 1.3: Structure of tetrameric human TRPM2 in the apo state. From N-terminus to C-terminus: MHR1/2 domain (blue), MHR3/4 domain (cyan), transmembrane domain (TMD, green) consisting of six helices (S1-S6) and a pore helix between S5 and S6, TRP helix (horizontal, yellow) with TRP re-entrant (protruding, yellow), coiled-coil (orange) consisting of rib helix (horizontal) and pore helix (vertical), NUDT9-H domain (red). **(A)** Solid surface representation. **(B)** Cartoon representation with one monomer highlighted in color. PDB: 6PUO (Huang et al., 2019).

1.1.5 Nucleotide-binding sites of TRPM2

Activation of TRPM2 by ADPR and the subsequent opening of the ion-conducting pore has been studied extensively. Functional data derived from mutagenesis investigations showed that several residues within the C-terminal NUDT9-H domain (Figure 1.3 red) of *hsTRPM2* (human TRPM2) are crucial for the activation by ADPR (Fliegert et al., 2017a; Kühn and Lückhoff, 2004; Yu et al., 2017). However, structural information revealed that NUDT9-H is not the only nucleotide-binding site of TRPM2. The N-terminal MHR1/2 domain (Figure 1.3 blue) is also involved in channel activation and ADPR binding (Huang et al., 2018, 2019).

1.1.5.1 The NUDT9-H domain differs in function in different species

As mentioned above, the C-terminal NUDT9-H (NUDT9-homologous) domain of TRPM2 is unique within the TRPM family and its sequence is suggestive of an enzymatic function due to homology (39% sequence identity, 50% sequence similarity) with the enzyme NUDT9. NUDT9 is a soluble pyrophosphatase with a so-called Nudix box motif which is responsible for binding ADPR and subsequently hydrolyzing it to adenosine monophosphate (AMP) and ribose 5-phosphate (Shen et al., 2003). Due to the homology, the NUDT9-H domain was predicted to harbor an ADPR binding site which activates the TRPM2 channel (Perraud et al., 2001).

In the invertebrate *nvTRPM2* (starlet sea anemone TRPM2), the NUDT9-H domain can both bind and hydrolyze ADPR. Direct channel gating however is independent from the domain in this species and relies purely on the MHR1/2 domain (Kühn et al., 2016; Tóth et al., 2020). Although NUDT9-H of *hsTRPM2* is not an active ADPR hydrolase, probably due to a substitution within the Nudix box (catalytic residues REF → RIL) (Iordanov et al., 2016; Kühn et al., 2016), recent cryo-EM structures revealed that it binds ADPR, supporting the functional data mentioned above. Previous studies showed that ADPR binding to the NUDT9-H domain is required for the activation of *hsTRPM2*, but the domain does not seem to act as the primary nucleotide-binding site (Huang et al., 2019). In *drTRPM2* (zebrafish TRPM2), NUDT9-H is also indispensable for channel gating similarly to *hsTRPM2* and contains a mutated Nudix box, indicating lack of enzymatic

activity (Huang et al., 2018; Iordanov et al., 2019). Although one study has shown weaker binding of ADPR to isolated *dr*NUDT9-H compared to *hs*NUDT9-H (Wang et al., 2018), the role of *dr*NUDT9-H in context of the full-length channel remains elusive since none of the *dr*TRPM2 structures could resolve if the nucleotide was bound to the domain. Taken together, the NUDT9-H domain changed its function from exerting enzymatic activity (in *nv*TRPM2) to assisting channel gating (in *hs*TRPM2). Gradually larger interfaces with the adjacent MHR1/2 domain over the course of evolution from invertebrates to mammals indicate that *dr*TRPM2 could be an intermediate in this evolutionary shift (Huang et al., 2019).

1.1.5.2 The MHR1/2 domain is a conserved site for channel activation

The first cryo-EM structures of *dr*TRPM2 unambiguously identified the N-terminal MHR1/2 domain as an ADPR-binding site (Huang et al., 2018). Since this work also produced the only available TRPM2 structure with an open channel pore so far (PDB: 6DRJ), a molecular activation mechanism was proposed based on this model: Upon ADPR binding in MHR1/2, the bi-lobed shape of the domain closes inducing a rotation. This rotation as well as the NUDT9-H domain moving towards the pore center leads to an MHR3/4 movement and a repositioning of the TRP helix, unlocking part of the TMD. The final channel opening due to an outward tilt of the transmembrane helix S6 is mediated by Ca²⁺ binding at the membrane-cytosol interface (Huang et al., 2018).

The MHR1/2 site was structurally confirmed to bind ADPR in *hs*TRPM2 and is crucial for channel activation in both vertebrate orthologues as shown by electrophysiology (Huang et al., 2018, 2019; Kühn et al., 2019a). While there is no structural proof of the site in invertebrate TRPM2, functional experiments confirmed it to be the only one responsible for *nv*TRPM2 channel activation by ADPR (Tóth et al., 2020). Therefore, the N-terminal MHR1/2 domain is a nucleotide-binding site of TRPM2 which is essential for channel gating. The residues involved in ADPR binding are highly conserved throughout the evolution of TRPM2 orthologues (Huang et al., 2018; Lü and Du, 2020).

1.1.6 TRPM2 is regulated by Ca²⁺

TRPM2 activation relies on Ca²⁺ binding to maintain an open channel through a positive feedback mechanism (McHugh et al., 2003). Functional patch clamp studies showed that Ca²⁺ ions bind in four shielded crevices near the pore entrance on the intracellular site of the tetrameric membrane protein (Csanády and Törőcsik, 2009). Biochemical and structural investigation have shown that a putative Ca²⁺ ion can be coordinated between acidic residues at the cytosolic ends of the transmembrane helices S2 and S3. This leads to a shift in S3, which is responsible for a movement of the S4-S5 loop, supporting channel opening (Huang et al., 2018). The crucial residues for Ca²⁺ coordination (in *hsTRPM2*: E843, Q846 in S2, N869, D872 in S3, E1073 in TRP helix (Huang et al., 2019)) are conserved, not only in TRPM2 orthologues (drTRPM2 (Huang et al., 2018)) but also in other Ca²⁺-sensitive members of the TRPM family (TRPM4 (Autzen et al., 2018), TRPM5 (Yamaguchi et al., 2019), TRPM8 (Yin et al., 2019b)). In addition to the Ca²⁺ binding site near the membrane interface, an EF-loop within the MHR1/2 domain (D267-D278 of *hsTRPM2*) was discovered to play a critical role in Ca²⁺-induced TRPM2 activation (Luo et al., 2018). EF-loops in general are part of typical helix-loop-helix structure units with conserved residues that are capable of chelating Ca²⁺ ions (Gifford et al., 2007).

Additionally, Ca²⁺-dependent regulation of TRPM2 is possible by calmodulin (CaM), which enhances ADPR-induced channel activation (Starkus et al., 2007). CaM can bind up to four Ca²⁺ ions with its four EF-hand motifs, resulting in a conformational change and subsequent recognition and modulation of target proteins (Crivici and Ikura, 1995). There is a wide range of CaM-binding motifs and the prediction of CaM binding sites remains challenging (Mruk et al., 2014). Nevertheless, a so-called IQ-like motif (named according to the first two amino acids) was identified in the MHR1/2 domain of *hsTRPM2* (I406-L416), which proved to be of functional relevance for channel activation. Thus, CaM binding to TRPM2 seems crucial for the positive feedback mechanism to maintain an open channel (Tong et al., 2006). Another CaM-binding site was identified in the NUDT9-H domain of *hsTRPM2* (W1355-I1368), which contributes to the temperature sensitivity of TRPM2 activation (Gattkowski et al., 2019).

1.1.7 TRPM2 is influenced by Zn²⁺

Besides activation by adenine nucleotides and Ca²⁺, the TRPM2 channel is additionally influenced by Zn²⁺ ions. The essential trace metal Zn²⁺ is involved in many physiological processes, for example as cofactor for enzymatic reactions, as a structural component for protein stability or as intra/intercellular signaling molecule (Kochańczyk et al., 2015). High concentrations of Zn²⁺ have a cytotoxic effect and influence pathological processes in the brain like excitotoxicity, a form of neuronal death upon sustained exposure to excitatory neurotransmitters (Granzotto et al., 2020). TRPM2 is inhibited by high extracellular concentrations of Zn²⁺, which makes it difficult to assess whether the channel is permeable to the ion (Yang et al., 2011). Surprisingly, in a study analyzing the connection between TRPM2 and ROS/Zn²⁺-induced Ca²⁺ signaling in microglial cells, free extracellular Zn²⁺ was also shown to activate TRPM2 through the oxidative stress machinery involving ROS and the PARP/PARG pathway (Mortadza et al., 2017). Cytosolic Zn²⁺ levels as well seem to influence the oxidative stress response and TRPM2 activity. The underlying mechanisms however are unknown (Abuarab et al., 2017; Ye et al., 2014). A direct modulatory role of Zn²⁺ on TRPM2 function seems conceivable since another member of the TRP family, TRPC5, harbors an intracellular Zn²⁺-binding motif that is conserved within TRPC channels (Park et al., 2019; Wright et al., 2020).

1.2 P2X purinoreceptor 7 (P2X7)

1.2.1 P2X receptors are essential for purinergic signaling

Until Geoffrey Burnstock used the term ‘purinergic’ for the first time in a review in 1972 (Burnstock, 1972), the adenine nucleotide adenosine triphosphate (ATP) was only established as an intracellular energy source. Although it seemed unlikely at the time that this ubiquitous molecule could exert extracellular signaling functions, Burnstock and colleagues showed that ATP is indeed a neurotransmitter, relaying signals through the extracellular synaptic cleft (Burnstock et al., 1964, 1970). The purinergic hypothesis further proposed that after the release from the pre-synaptic cell and the activation of its receptors on the post-synaptic cell, extracellular ATP is enzymatically broken down to adenosine, which is subsequently reincorporated into cells and used for ATP re-synthesis (Burnstock, 1972, 1976). Despite the initial controversy, the hypothesis turned out to be true. In addition, purinergic signaling is not only important for neurotransmission but is also involved in a lot of other physiological processes like immune response, carcinogenesis and the pathology of several diseases (Gomez-Villafuertes and Adinolfi, 2020). There are different receptor classes that bind either adenosine and AMP (P1 receptors), or ADP and ATP (P2 receptors) (Burnstock, 1978). The ATP-binding P2 receptors are subdivided into two main types: ionotropic P2X receptors (ion channels) and metabotropic P2Y receptors (G-protein-coupled receptors) (Burnstock and Kennedy, 1985).

P2X receptors are non-selective cation channels that are only found in eukaryotes and were first cloned in 1994 (Brake et al., 1994; Valera et al., 1994). The physiological protein channels are assembled either as homotrimers or heterotrimers of seven subtypes (P2X1-P2X7). P2X receptors are widely expressed within the organism and important for many physiological processes (Surprenant and North, 2009). Structurally, a P2X monomer comprises a large extracellular domain and two pore-forming transmembrane helices. Both termini are located in the cytosol, forming cytoplasmic domains of different sizes (Figure 1.4). The first crystal structure of a P2X receptor in 2009 (P2X4) laid the foundation for the mechanistic understanding of ligand gating, allosteric modulation and ion permeation of the P2X family (Kawate et al., 2009).

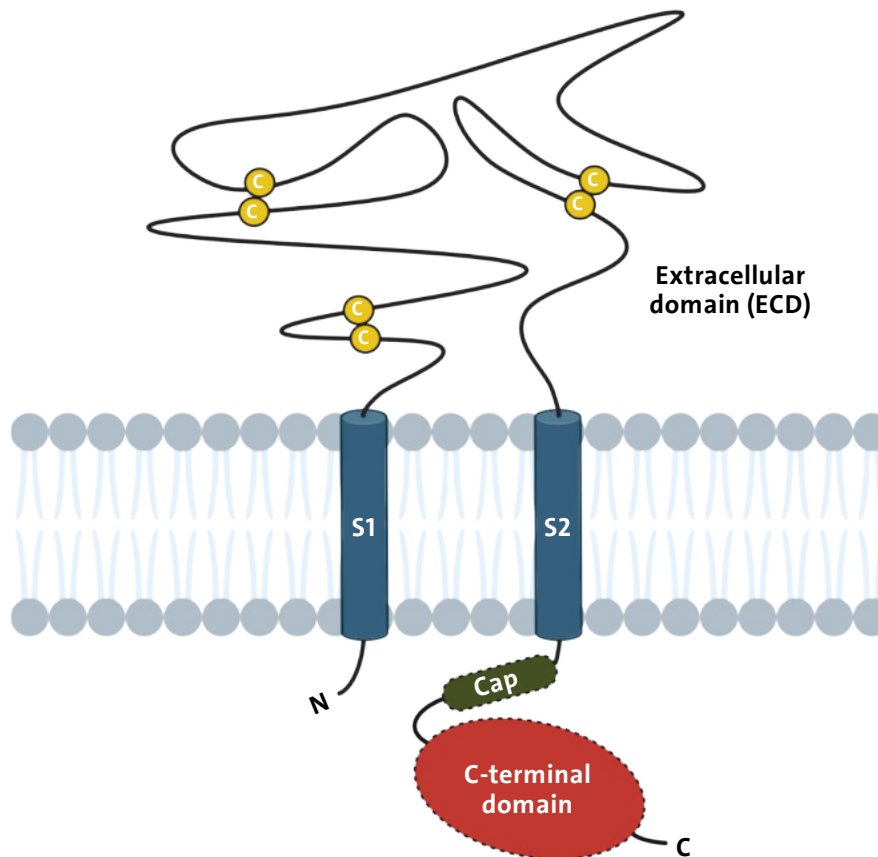


Figure 1.4: Common domain architecture of the P2X family. From N-terminus to C-terminus (both intracellular): short intracellular N-terminus, transmembrane helix S1, large extracellular domain (ECD) with at least three conserved disulfide bridges (C-C), transmembrane helix S2, C-terminal cap domain (in some P2X members), C-terminal domain of different size. Created with BioRender.com, adapted from (North, 2002).

1.2.2 P2X7 is involved in various physiological processes

The P2X purinoreceptor 7 (P2X7) is the largest within the P2X family (595 amino acids) because it contains a significantly longer intracellular C-terminal domain compared to all other members (see 1.2.4). The homotrimeric ion channel was first characterized under its former name P2Z (Surprenant et al., 1996) and contains unique functional properties: It requires hundreds of micromolar ATP for activation, which is one to three orders of magnitude higher compared to other P2X receptors. This low affinity suggests that it acts as a sensor for high ATP concentrations that are typically limited to areas of severe inflammation (Linden et al., 2019). P2X7 activation allows the influx of Ca^{2+} and Na^{+} as well as efflux of K^{+} , resulting in rapid membrane depolarization (Surprenant et al., 1996). While the response of most other P2X receptors diminishes quickly after

activation (P2X1, P2X3: milliseconds; P2X2, P2X4: seconds), P2X7 shows a complete lack of desensitization (Jarvis and Khakh, 2009; Koshimizu et al., 1999). Furthermore, prolonged stimulation of P2X7 with ATP results not only in cation channel opening, but in addition induces formation of a larger, non-selective plasma membrane pore. This ‘macropore’ allows the passage of molecules up to ~800 Da in size (Surprenant et al., 1996). Since the available structures of P2X7 do not show any evidence of a dilated pore (Karasawa and Kawate, 2016; Kasuya et al., 2017; McCarthy et al., 2019), it seems feasible that the macropore is formed by recruited auxiliary proteins like Pannexin-1 (Pelegri and Surprenant, 2006). However, there is also functional proof pointing towards pore dilation of the receptor itself (Karasawa et al., 2017; Di Virgilio et al., 2018; Yan et al., 2008).

P2X7 is the only P2X member that can act as a receptor inducing cell lysis (Rassendren et al., 1997; Surprenant et al., 1996). This cytotoxic function, for which the formation of the macropore is required, begins with plasma membrane blebbing (Adinolfi et al., 2010) and is linked to many physiological processes concerning innate immunity and inflammation (Adinolfi et al., 2018). For example, due to its role in IL-1 processing and release (Ferrari et al., 2006), P2X7 is one of the central purinergic receptors that drive the formation of a multiprotein complex (the inflammasome) that activates the inflammatory enzyme caspase-1 and ultimately induces cell death (Martinon et al., 2002; Pelegrin, 2021). Besides inflammation, P2X7 is also associated with a worsening disease prognosis in different cancer entities, for example in neuroblastoma (Amoroso et al., 2015), prostate cancer (Slater et al., 2004), and colorectal cancer (Calik et al., 2020). The receptor is expressed in nearly all organs and tissues (Burnstock and Knight, 2004). Its involvement in cancer therapy (Roger et al., 2015) and its role in neurodegenerative diseases (Bhattacharya and Biber, 2016) makes P2X7 a promising pharmacological target (Bartlett et al., 2014; Burnstock and Knight, 2018).

1.2.3 Structure of P2X7 and the activation by ATP

All P2X receptors share a common fold that was first observed and characterized in the crystal structure of P2X4 (Kawate et al., 2009). The existing P2X7 structures were either

solved by X-ray crystallography (chicken P2X7 (Kasuya et al., 2017) and panda P2X7 (Karasawa and Kawate, 2016)) or by cryo-EM (rat P2X7 (McCarthy et al., 2019)). While truncated receptors were used for the crystallographic studies, the cryo-EM structures of apo/ATP-bound P2X7 also include the unique C-terminal ballast domain. The overall architecture (Figure 1.5, PDB: 6U9W (McCarthy et al., 2019)) consists of four layers: extracellular domain (ECD) responsible for ATP binding, transmembrane domain (TMD), cytoplasmic cap domain (Cap), cytoplasmic ballast domain (BD). The hydrophilic ECD contains numerous β -sheets and is stabilized by three disulfide bonds which are conserved within the P2X family (cf. Figure 1.4). There are three inter-subunit binding sites for ATP in a U-shaped conformation between the three ECDs of the homotrimer (Figure 1.5 B).

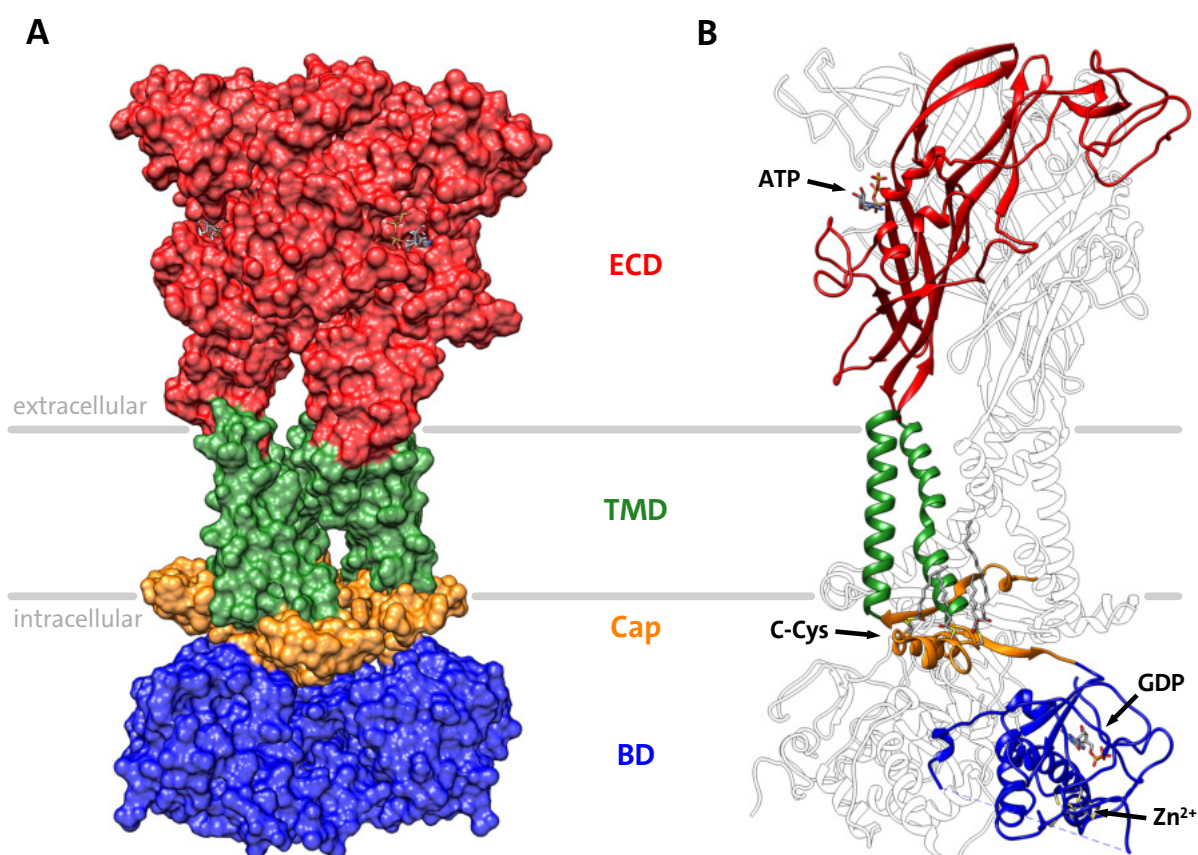


Figure 1.5: Structure of trimeric rat P2X7 in the ATP-bound state. From top to bottom: hydrophilic extracellular domain (ECD, red) with ATP, transmembrane domain (TMD, green) consisting of two α -helices per protomer, cytoplasmic cap domain (orange) including cytoplasmic cysteine-rich anchor (C-Cys), C-terminal ballast domain (blue) with GDP and Zn²⁺. **(A)** Solid surface representation. **(B)** Cartoon representation with one monomer highlighted in color. PDB: 6U9W (McCarthy et al., 2019).

When the ATP agonist binds to apo P2X7, the upper parts of the ECD undergo cleft closure motions that induce the opening of the lower ECD areas. This leads to a rearrangement of the TMD, resulting in channel opening (McCarthy et al., 2019). Due to the pharmacological importance, various P2X7 inhibitors and their structural effects on the receptor were analyzed. One ATP analogue was found to bind in the same site as the agonist (orthosteric) in a different conformation, leading to an 'incompletely activated' channel (Kasuya et al., 2017). Different allosteric inhibitors bind in a common site located above the orthosteric binding pocket. These promising drug targets interrupt the ATP-induced conformational changes within the ECD and thus inhibit channel opening (Karasawa and Kawate, 2016).

The TMD consists of two membrane-spanning α -helices per monomer and forms the ion-conducting pore (Figure 1.5 B, green). Below the TMD, a cytoplasmic cap domain acts as a structural scaffold (Figure 1.5 B, orange). This function stands in striking contrast to the one of the cytoplasmic cap of the fast-desensitizing P2X3 receptor, which is reported to be important for the kinetics of desensitization (Mansoor et al., 2016). The non-desensitizing P2X7 receptor is anchored to the membrane by palmitoyl groups on the cytoplasmic cysteine-rich anchor of the cap domain (Figure 1.5 B, C-Cys). The palmitoylation is thought to prevent receptor desensitization since P2X7 mutants lacking a palmitoylated C-Cys anchor exhibit desensitizing features (McCarthy et al., 2019). The cap domain is connecting the TMD to the C-terminal ballast domain (Figure 1.5B, BD, blue). This cytoplasmic element coordinates a Zn^{2+} ion complex and has a binding site for guanosine diphosphate (GDP) (McCarthy et al., 2019).

1.2.4 The C-terminal ballast domain of P2X7 is unique

The ballast domain comprises the C-terminal ~200 residues ($\alpha 9$ - $\alpha 16$, $\beta 16$ - $\beta 18$) of each P2X7 protomer. It is unique within the P2X family and its fold has no significant structural homology to any other protein in the PDB. Its sequence originates from a protein family present in all Metazoa which was fused to a P2X4-like gene, resulting in P2X7 (Rump et al., 2020). To date, only one structural study could resolve the domain, and this work could not conclude whether it is formed by a single protomer chain (as

shown in Figure 1.5 B) or by two intertwined protomers. The trimeric ballast domain forms a 'cytoplasmic plug' below the cap area (McCarthy et al., 2019). The functional significance of the binding sites for Zn^{2+} and GDP is unclear. Previous investigations suggested that the cysteine residues forming the Zn^{2+} -binding site play a role in the cell surface localization of the P2X7 receptor. This study suggested palmitoylation of these residues, but they are structurally not near the membrane. However, this indicates an involvement in proper receptor processing and trafficking (Gonnord et al., 2009). The GDP-binding pocket, located at exposed interfaces between two ballast protomers, selectively binds guanosine nucleotides with nanomolar affinities (McCarthy et al., 2019). Its role regarding P2X7 receptor function is unknown.

Functional studies with P2X7 lacking the entire ballast domain show that it has no influence on ATP binding in the ECD and subsequent channel gating, including current facilitation (a P2X7-specific property describing the increase of current amplitude upon repeated agonist application) and ion selectivity (Cheewatrakoolpong et al., 2005; McCarthy et al., 2019; Surprenant et al., 1996). Nevertheless, its importance for the cytotoxic action of P2X7 was previously established with the discovery of the receptor (Surprenant et al., 1996) and confirmed by further work with naturally occurring truncated forms (Adinolfi et al., 2010) as well as with splice variants of P2X7 (Cheewatrakoolpong et al., 2005). Moreover, the C-terminal region was found to affect pore dilation and membrane blebbing prior to inducing apoptosis (Wilson et al., 2002).

1.2.5 P2X7 interacts with calmodulin (CaM)

Many proteins interact with P2X7 physically or functionally and consequently influence its diverse properties and signaling pathways (Kopp et al., 2019). One of these proteins is the multifunctional messenger protein calmodulin (CaM). The interaction with CaM was discovered functionally by pull-down experiments with rat P2X7. A 1-5-16 CaM-binding motif (IX₃LX₁₀W) within the C-terminal ballast domain (I541-W556 of rat P2X7) was identified (Roger et al., 2008). This Ca^{2+} -dependent motif is a CaM-binding sequence which exhibits a specific spacing of bulky, hydrophobic anchor residues (Tidow and Nissen, 2013). While the mutation of this motif or chelation of Ca^{2+} inhibits P2X7-induced

membrane blebbing and current facilitation, a dye uptake assay suggested that P2X7-induced membrane permeabilization is unaffected (Roger et al., 2008). In human P2X7, where the above-mentioned CaM-binding motif is not complete, no Ca²⁺-dependent facilitation could be detected. However, replacement of three crucial residues with the respective amino acids of the rat version (T541I, C552S, G559V) reconstituted current facilitation (Roger et al., 2010). It remains elusive if CaM interacts with the human P2X7 orthologue.

2 AIM OF THE THESIS

The ion channels TRPM2 and P2X7, as crucial players of the immune response as well as of inflammatory processes, are both activated by adenine nucleotides. The ligand-binding domains of TRPM2 as well as the C-terminal ballast domain of P2X7 are of special interest since the mechanisms behind their functions are not fully understood. In order to gain more structural and functional insight into their functionality, the aim of this dissertation is the further characterization of these domains.

2.1 Characterization of ligand-binding domains of TRPM2

The N-terminal MHR1/2 domain and the C-terminal NUDT9-H domain of TRPM2 are involved in binding the TRPM2 agonist ADPR. MHR1/2 contains the suggested conserved binding site while NUDT9-H has different functions in different orthologues. Interestingly, in the *hs*TRPM2 structures the nucleotide shows different molecular shapes: a horseshoe-like conformation in MHR1/2 and an extended shape in NUDT9-H. The TRPM2 antagonist 8-Br-cADPR is only observed in the MHR1/2 domain, probably due to its naturally fixed horseshoe-like conformation (Huang et al., 2019). It is not known where the superagonist 2'-deoxy-ADPR and other ADPR analogues (e.g. 8-Br-ADPR) bind. Consequently, both ligand-binding domains of TRPM2 will be expressed in soluble forms and their interactions with nucleotide ligands, Zn²⁺ and CaM will be characterized. The influence on channel function will be studied by electrophysiology. The TRPM2-CaM interaction will be further analyzed in context of the full-length channel.

2.2 Characterization of the P2X7 ballast domain

P2X7 channel activation and gating is independent of the C-terminal ballast domain. However, the domain is important for the cytotoxic action of P2X7. In order to further understand its modulatory rule, it will be expressed in a soluble form and characterized biochemically and biophysically. Specially, the binding of GDP and CaM will be investigated using various biophysical methods.

3 TRPM2

This chapter is dedicated to the functional and structural analysis of the ligand-binding domains of TRPM2. Although both domains were characterized, the central element of the experiments was the N-terminal MHR1/2 domain of zebrafish TRPM2. Results regarding this domain are published (Riekehr et al., 2022; Sander et al., 2022a) and were obtained by the author of this thesis. Furthermore, CaM binding to TRPM2 was analyzed in context of the MHR1/2 domain and the full-length channel.

3.1 Results

3.1.1 Expression and purification of the zebrafish MHR1/2 domain (*drMHR1/2*)

The N-terminal MHR1/2 domain of zebrafish TRPM2 (*drMHR1/2*, residues 1-419 of *drTRPM2*) was expressed in BL21 Gold *E. coli* and subsequently purified by two steps of immobilized metal affinity chromatography (IMAC, classical as well as reverse after TEV cleavage of His₆-tag) and size exclusion chromatography (SEC). The purification resulted in a monodisperse, pure sample of monomeric *drMHR1/2* (Figure 3.1 A). Analysis by nano differential scanning fluorometry (nDSF) revealed that the purified protein is stable with a melting temperature of 50.8°C (Figure 3.1 B).

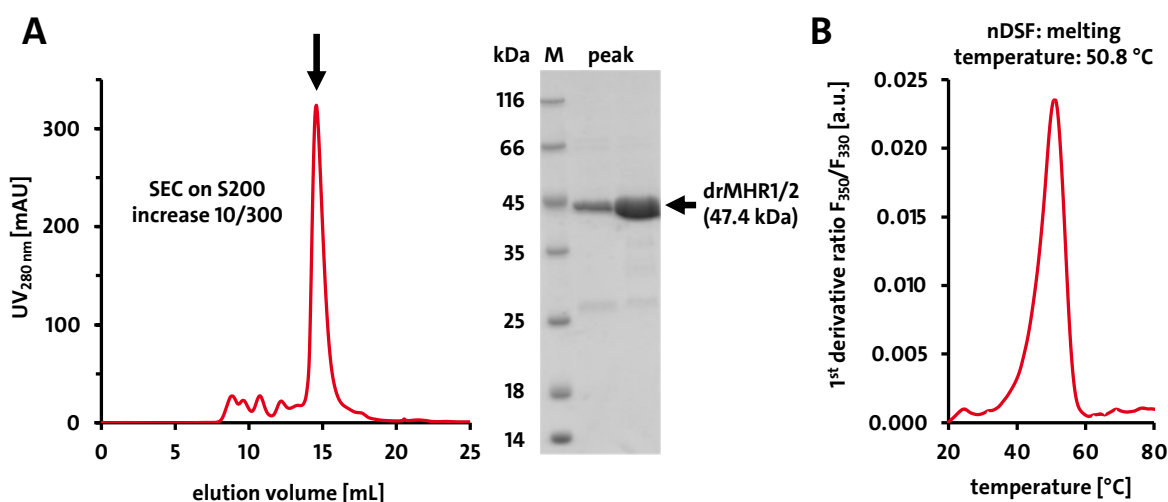


Figure 3.1: Purification and thermal stability of *drMHR1/2*. (A) SEC profile of *drMHR1/2* on an S200 increase 10/300 column with a monodisperse peak at ~15 mL (indicated by arrow) that corresponds to pure, monomeric *drMHR1/2* (47.4 kDa) as shown by SDS-PAGE (4-20%, Coomassie-stained), M: marker. (B) nDSF melting analysis of 10 μ M *drMHR1/2*. First derivative of fluorescence intensity ratio F_{350}/F_{330} with maximum at 50.8°C (melting temperature).

3.1.2 Characterization of ADPR and ADPR derivatives binding to *drMHR1/2*

The MHR1/2 domain contains a binding site for the TRPM2 agonist ADPR, which was identified in cryo-EM structures from human and zebrafish (Huang et al., 2018, 2019). It is currently unknown whether the TRPM2 superagonist 2'-deoxy-ADPR (Fliegert et al., 2017b) binds to the same site. Consequently, binding of ADPR and 2'-deoxy-ADPR to the isolated *drMHR1/2* domain was biophysically analyzed. Titration to the domain and subsequent analysis by nDSF showed that the melting temperature shifts compared to apo-*drMHR1/2* (cf. Figure 3.1 B) and both compounds concentration-dependently stabilize it (Figure 3.2 A). Isothermal titration calorimetry (ITC) revealed endothermic binding in the low micromolar range for both ligands with 2'-deoxy-ADPR ($1.1 \mu\text{M} \pm 0.4 \mu\text{M}$) showing slightly tighter binding than ADPR ($2.4 \mu\text{M} \pm 1.1 \mu\text{M}$) (Figure 3.2 B-C).

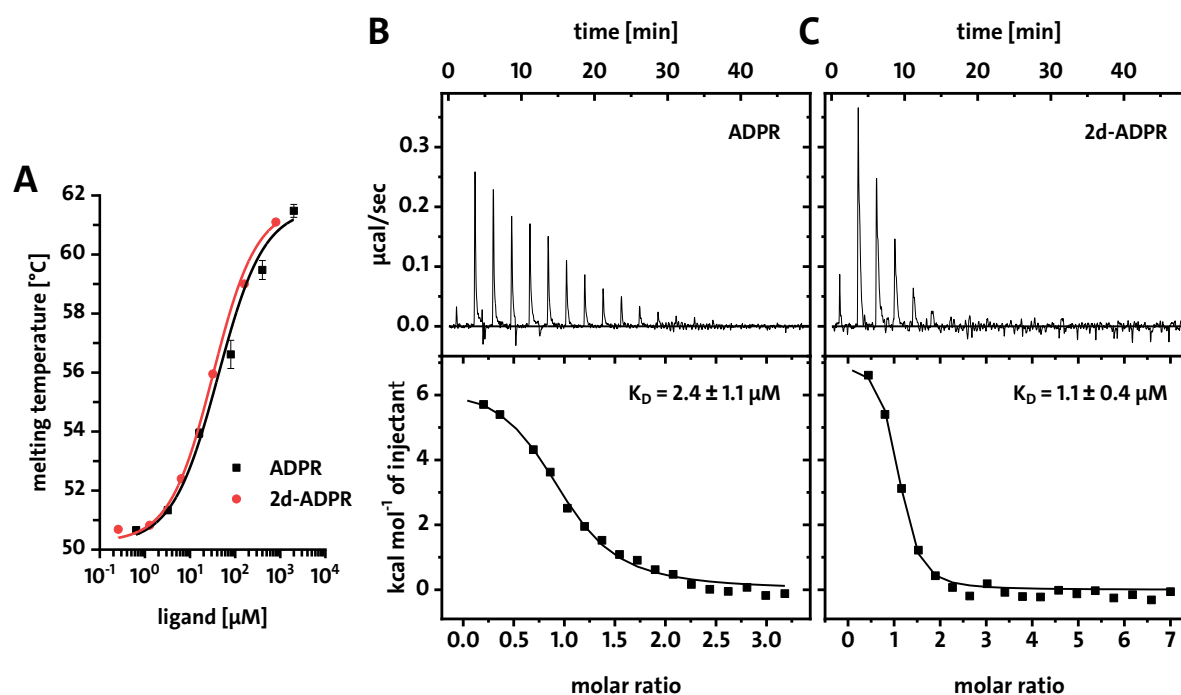


Figure 3.2: ADPR and 2'-deoxy-ADPR bind to *drMHR1/2*. (A) Binding of *drMHR1/2* (10 μM) and ADPR / 2'-deoxy-ADPR (2d-ADPR) shown by shift of melting temperature observed by nDSF (triplicates). (B) Binding of *drMHR1/2* (20 μM) and ADPR (300 μM) as measured by ITC. K_D value is an average of three independent experiments. (C) Binding of *drMHR1/2* (10 μM) and 2'-deoxy-ADPR (500 μM) as measured by ITC. K_D value is an average of three independent experiments. Same y-scales as in (B).

The ADPR derivatives 8-Br-ADPR (Partida-Sanchez et al., 2007) and 8-Br-cADPR (Kolisek et al., 2005) were suggested to exhibit an antagonistic effect on TRPM2 and the role of cADPR regarding TRPM2 activation is controversially discussed. Therefore, all three compounds were subjected to ITC experiments with *drMHR1/2*. Due to the instability problems of cyclic ADPR derivatives, a new aliquot was used for every measurement. For 8-Br-ADPR, the assay showed binding with similar affinity as ADPR and 2'-deoxy-ADPR ($1.4 \mu\text{M} \pm 0.5 \mu\text{M}$, Figure 3.3 A). Interestingly, the cyclic nucleotides cADPR and 8-Br-cADPR both clearly did not bind to *drMHR1/2* (Figure 3.3 B-C).

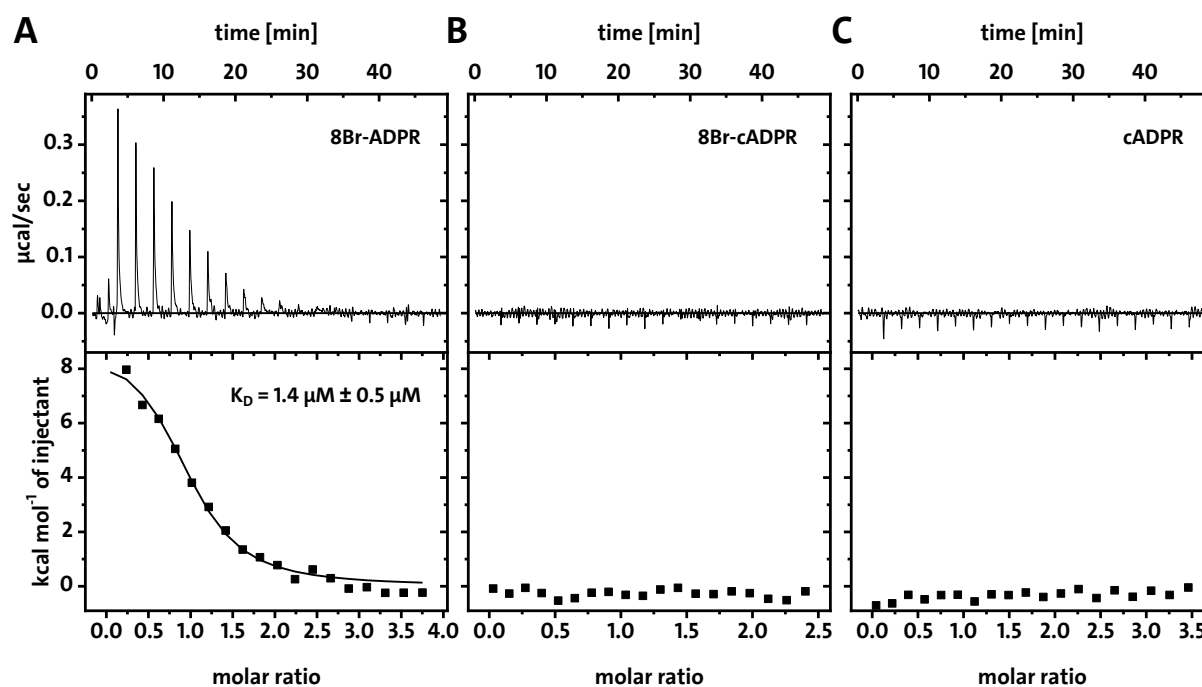


Figure 3.3: Biophysical characterization of ADPR derivatives binding to *drMHR1/2*. Binding of *drMHR1/2* ($20 \mu\text{M}$) and ADPR derivatives ($300 \mu\text{M}$) as measured by ITC. K_D values are averages of three independent experiments. Same y-scales in all panels. **(A)** 8-Br-ADPR binds to *drMHR1/2*. **(B)** 8-Br-cADPR does not bind to *drMHR1/2*. **(C)** cADPR does not bind to *drMHR1/2*.

3.1.3 The human MHR1/2 domain (*hsMHR1/2*) does not express in *E. coli*

To assess whether the MHR1/2 domain is in fact a conserved nucleotide binding site throughout evolution or whether there are differences between the zebrafish and human orthologues, human MHR1/2 (*hsMHR1/2*) was expressed in *E. coli* and purified by IMAC. Three different constructs were used (N-terminal His₆-tag, N-terminal GST-His₆-tag, N-terminal Lipo-His₆-tag) to test the expression in different *E. coli* strains.

Unfortunately, neither system showed protein bands of the correct size in the SDS-PAGE analysis of the subsequent purification (Figure 3.4). The IMAC test elution fractions only contained impurities from *E. coli* or possibly break-down products of the target protein. This suggests that the *hsMHR1/2* domain does not express in *E. coli*, not even when coupled to N-terminal solubility fusions like GST or the Lipo-tag.

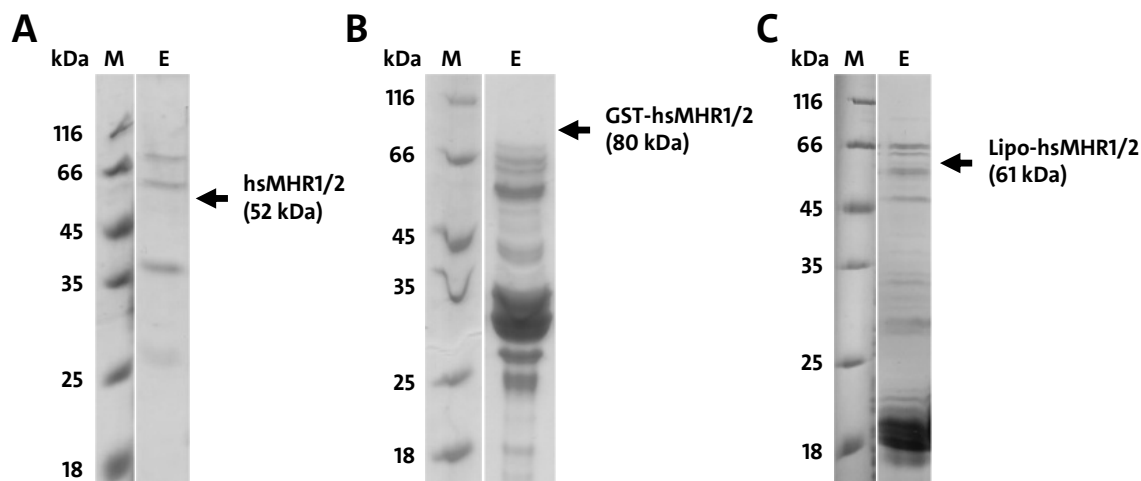


Figure 3.4: The human MHR1/2 domain does not express in *E. coli*. Test expressions and purifications of different constructs of *hsMHR1/2* in various *E. coli* strains. Shown are representative examples of the IMAC elution (E) of one representative example strain. Analysis by SDS-PAGE (4-20%, Coomassie-stained). Arrows indicate the expected molecular weight of the constructs. M: marker. **(A)** *hsMHR1/2* in BL21 Gold *E. coli*. **(B)** *GST-hsMHR1/2* in Rosetta 2 *E. coli*. **(C)** *Lipo-hsMHR1/2* in BL21 Gold pLysS *E. coli*.

3.1.4 Crystal structure of *drMHR1/2*

The MHR1/2 domain of *drTRPM2* was further analyzed structurally by means of X-ray crystallography. The protein was expressed in the methionine-auxotrophic *E. coli* strain B834 (DE3), which allowed selenomethionine labeling for Se-SAD (Selenium single-wavelength anomalous dispersion) phasing. Protein crystals of *drMHR1/2* had triangular shape, reached sizes of approximately 50-120 μm , and appeared after one to three days (Figure 3.5 A). Two molecules were visible in the asymmetric unit and crystal contacts were generated through the exposed loops. Almost an entire MHR1/2 domain could be resolved at 2.0 \AA resolution with unambiguous side chain information (residues 33-418, missing the loop comprising residues 201-209). The overall structure (Figure 3.5 B) revealed a bi-lobed, clamshell-like shape that superimposed well with the MHR1/2 domain of the published cryo-EM structure of apo *drTRPM2* (Figure 3.5 C-D, PDB: 6DRK).

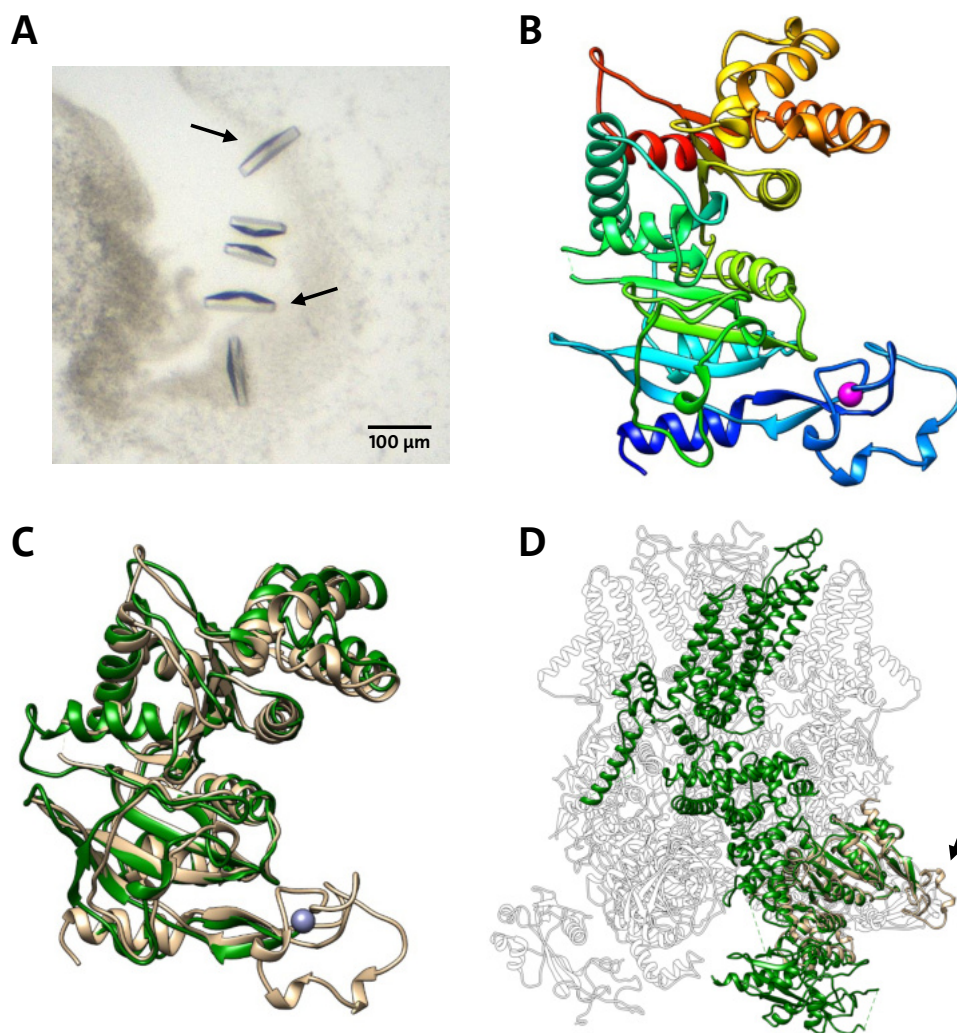


Figure 3.5: Crystallization and crystal structure of *drMHR1/2*. (A) Representative image of *drMHR1/2* crystals of triangular shape with diameters of 50-120 μm , examples marked by arrows. (B) Overall fold of *drMHR1/2* with a bi-lobed clamshell-like structure (color-coded from blue (N-terminus) to red (C-terminus)). Zn^{2+} ion is shown as magenta sphere. (C) Overlay of the *drMHR1/2* crystal structure (wheat) with the MHR1/2 domain from a *drTRPM2* cryo-EM structure (green, PDB: 6DRK). Zn^{2+} ion is shown as blue sphere. (D) Superposition of the *drMHR1/2* crystal structure (wheat) on the tetrameric *drTRPM2* cryo-EM structure (white with one monomer highlighted in green, PDB: 6DRK), arrow indicates the location of the Zn^{2+} -binding site.

Crystallization trials of ligand complexes with ADPR and 2'-deoxy-ADPR were performed to obtain better structural insights into ligand binding to *drMHR1/2*. However, no crystal growth was observed with the protein-ligand complexes in various crystallization conditions. Furthermore, ADPR was soaked into existing *drMHR1/2* crystals, which was unfortunately also not successful since it led to crystal dissolution.

3.1.5 Characterization of a conserved Zn²⁺-binding domain in TRPM2

Due to the high resolution (2.0 Å) of the *drMHR1/2* crystal structure, unambiguous model building was possible and led to the identification of a domain (residues 53-95, located between β1 and β2) that had not been resolved in the lower resolution cryo-EM structures of *drTRPM2* (Huang et al., 2018). Surprisingly, clear electron density within this novel domain indicated an ion that is coordinated by three cysteines and one histidine (Figure 3.6 A). The structure of the interacting residues (C53, C65, C67, H74) revealed geometry and bond lengths that are typical for tetrahedral Zn²⁺ ion coordination (Figure 3.6 B, according to *CheckMyMetal* server (Zheng et al., 2017)). An X-ray fluorescence energy scan of the protein crystal was performed near the zinc absorption K edge (9.6586 keV), which unambiguously confirmed the presence of a Zn²⁺ ion (Figure 3.6 C).

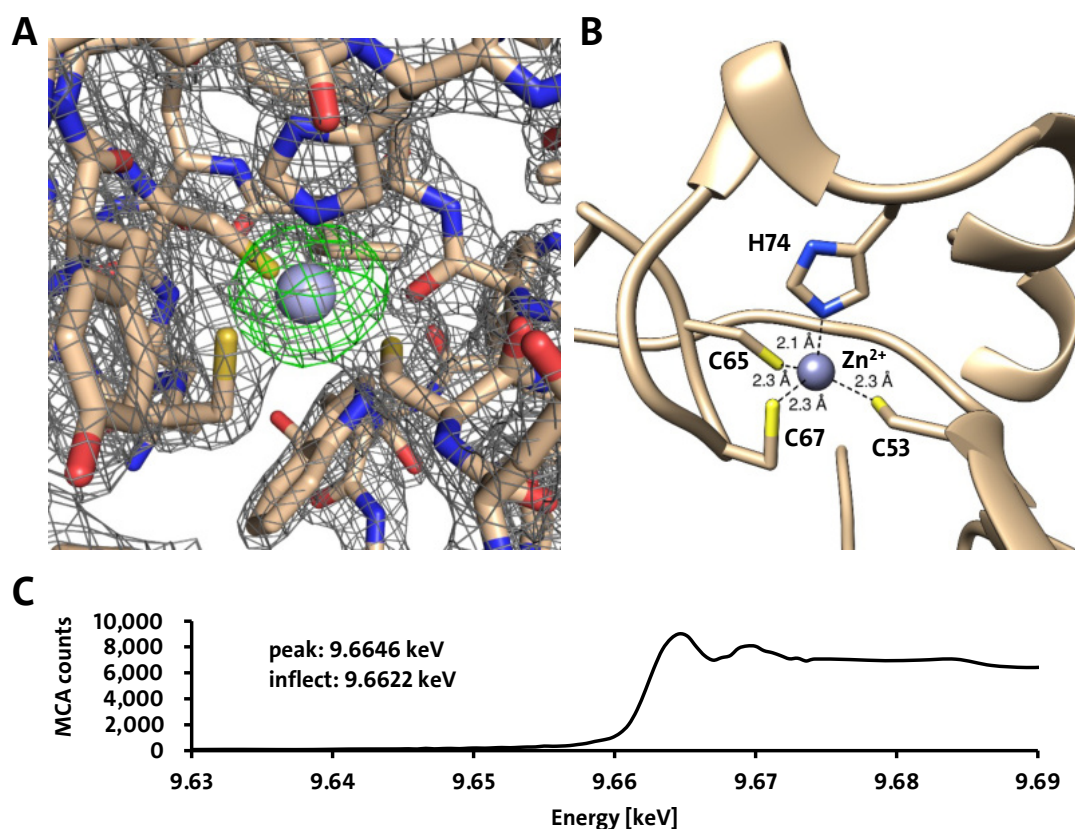


Figure 3.6: Novel Zn²⁺-binding domain in *drMHR1/2*. (A) Electron density of the novel Zn²⁺-binding site (grey mesh) and PHENIX POLDER electron density after omission of the Zn²⁺ ion (green mesh) with the atomic model (wheat) and the Zn²⁺ ion (grey). (B) Detailed structure view of the Zn²⁺-binding domain with a tetrahedral coordination of the Zn²⁺ ion by C53, C65, C67, H77. (C) X-ray energy scan of the fluorescence emitted by the sample near the zinc absorption K edge (9.6586 keV) confirming ion identity.

To investigate whether the identified Zn²⁺-binding site is of relevance not only for *dr*TRPM2 but also for other members of the TRPM family, sequence homologies were analyzed. A multiple sequence alignment showed that all four residues involved in Zn²⁺ binding (C53, C65, C67, H74) are conserved between TRPM2 orthologues from different species and most human TRPM channels (Figure 3.7). This stringent evolutionary conservation from invertebrates (e.g. *N. vectensis*) to mammals (e.g. *H. sapiens*) strongly suggests a physiological relevance for the novel Zn²⁺-binding domain.

<i>dr</i> TRPM2	49	KKKE	C	CFYVEDGR	-----	-----	EGI	C	K	C	GYPKVQ	H	CDEA	78
<i>hs</i> TRPM1	3	-----	-----	DSN	-----	-----	R	C	C	GQFTNQ	H	IPL	20	
<i>hs</i> TRPM2	68	KKKE	C	VYFVSSKLS	DAG	-----	KVV	C	C	GYTHEQ	H	LEEA	102	
<i>hs</i> TRPM3	70	YKRE	C	VHIIIPSTKDPH	-----	-----	R	C	C	GRLIGQ	H	VGLT	100	
<i>hs</i> TRPM4	16	KKKT	C	TTFIVDSTDPG	-----	-----	GTL	C	C	GRPRTA	H	PAVA	48	
<i>hs</i> TRPM5		-----	-----	-----	-----	-----	-----	-----	-----	-----	-----	-----		
<i>hs</i> TRPM6	22	DKRE	C	STIIPSSKNPHR	CTPVCQVCQNLIR	-----	C	C	GRLIGD	H	HAGID	65		
<i>hs</i> TRPM7	12	TKRE	C	VYIIPSSKDPHR	CLPGCQICQQLVRC	-----	F	C	GRLVKQ	H	HACFT	55		
<i>hs</i> TRPM8	50	KKRE	C	VFFTKDSKAT	-----	-----	ENV	C	K	GYAQSQ	H	MEGT	81	
<i>nv</i> TRPM2	41	SRRE	C	IRFVVPKSHDVS	-----	-----	R	C	K	GRPRER	H	SQQA	71	
<i>gg</i> TRPM2	77	RKKE	C	TYFVSSQTS	SDSG	-----	RVV	C	C	GYLREQ	H	LEDA	111	
<i>mm</i> TRPM2	67	KKKE	C	VYFVSSKLS	DAG	-----	KVV	C	C	GYTHEQ	H	LEVA	101	
<i>rn</i> TRPM2	67	KKKE	C	VYFVSSKLS	DAG	-----	KVV	C	C	GYTHEQ	H	IEVA	101	
<i>pp</i> TRPM2	67	KKKE	C	VYFVSSKLS	DAG	-----	KVV	C	C	GYTHEQ	H	LEEA	101	

Figure 3.7: Zn²⁺-binding domain in MHR1/2 is conserved in TRPM channels. Multiple sequence alignment of novel Zn²⁺-binding domain in TRPM channels. Conservation of the four Zn²⁺-coordinating residues (marked in red) in the N-terminus of most TRPM channels. Alignment of all human (*Homo sapiens*) TRPM channels and TRPM2 from sea starlet anemone (*Nematostella vectensis*), chicken (*Gallus gallus*), mouse (*Mus musculus*), rat (*Rattus norvegicus*), chimpanzee (*Pan pansicus*), zebrafish (*Danio rerio*).

3.1.6 The Zn²⁺-binding domain is required for TRPM2 structure and function

As Zn²⁺ ions often function as structural components for the stability of proteins (Kambe et al., 2015), experiments analyzing protein integrity of *dr*MHR1/2 Zn²⁺-binding site mutants were performed. Two of the cysteine residues involved in coordinating the Zn²⁺ ion were mutated to alanine (C65A and C67A), either individually or as a double mutant. The mutant *dr*MHR1/2 sequences were recombinantly expressed in *E. coli*, but the proteins seemed to be insoluble (Figure 3.8), probably due to incorrect folding, suggesting the novel Zn²⁺-binding site to be of importance for protein integrity.

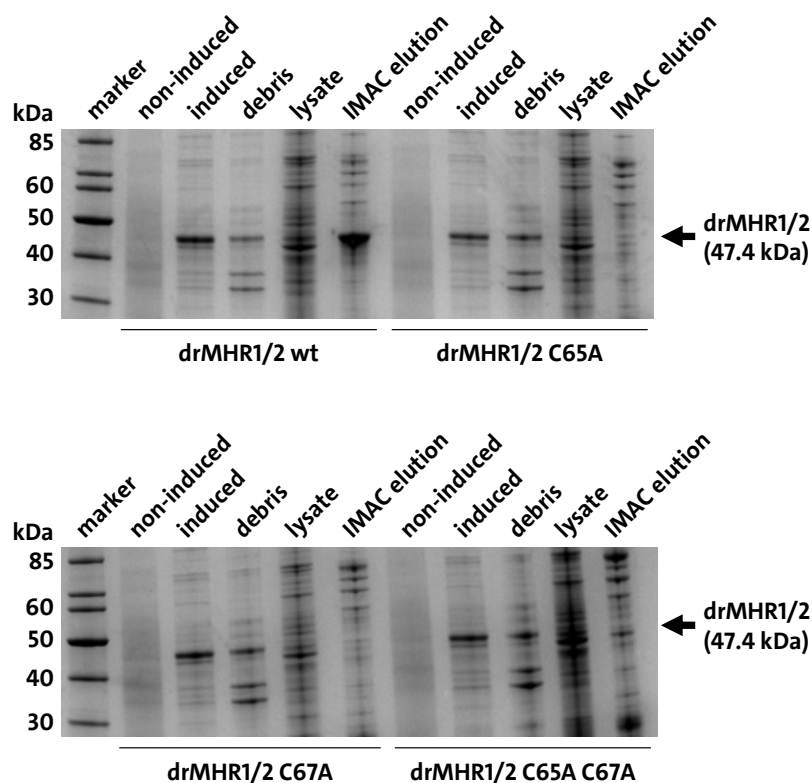


Figure 3.8: Zn²⁺-binding domain is important for *drMHR1/2* protein integrity. Coomassie-stained SDS-PAGE gels (4-20%) show that *drMHR1/2* mutants (C65A, C67A and C65A C67A double mutant) are expressed like the wild-type (induced cells lane), but do not seem to be soluble (missing *drMHR1/2* bands in lysate and IMAC elution lanes).

Next, a cell surface biotinylation assay with Zn²⁺-binding site mutants was performed to examine whether protein integrity is also affected in the context of full-length TRPM2. For this, the sequences coding for *hsTRPM2* variants that contained the equivalent mutations of the Zn²⁺-coordinating residues (in human: C89A and C91A) were transiently expressed in HEK293 cells. Western blot analysis of total membrane fractions and biotin cell surface pull-downs revealed that all mutants were successfully expressed and transported to the cell membrane, albeit with reduced levels compared to the wild type protein (Figure 3.9).

Whole-cell patch clamp experiments were performed to analyze if the remaining fraction of the TRPM2 variants with Zn²⁺-binding site mutations in the cell membrane still exhibit normal channel activity. HEK293 cells were transiently transfected with the *hsTRPM2* variants and channel function was evaluated by measuring currents upon activation by ADPR and Ca²⁺ (Figure 3.10).

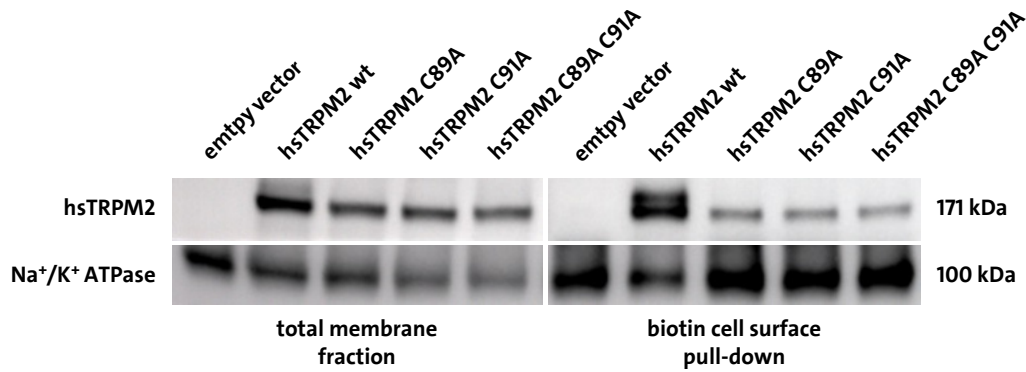


Figure 3.9: Zn²⁺-binding domain is important for *hsTRPM2* protein integrity. Cell surface biotinylation assay of HEK293 cells transfected with *hsTRPM2* Zn²⁺-binding site variants (wild type (wt), C89A, C91A, C89A C91A double mutant) highlighting the importance of the motif. The expression level of the TRPM2 mutants is lower than TRPM2 wt on the cell surface (biotin pull-down) as well as in the total membrane fraction as shown by western blot. Loading control: Na⁺/K⁺ ATPase.

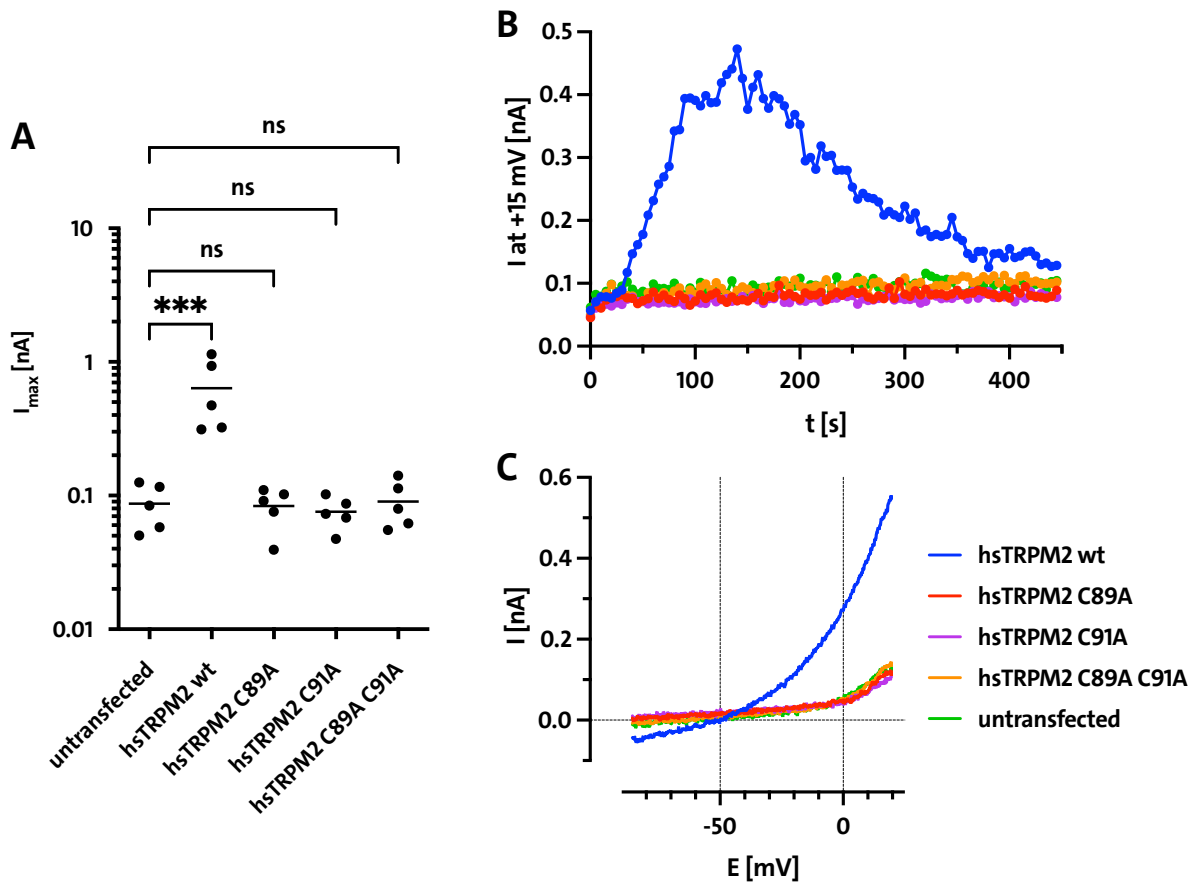


Figure 3.10: Zn²⁺-binding domain is important for *hsTRPM2* channel activity. Whole-cell patch clamp measurements of HEK293 cells transfected with *hsTRPM2* variants (wild type (wt), C89A, C91A, C89A C91A double mutant). The remaining fraction of mutant protein on the cell surface does not invoke a current upon infusion of 200 nM free Ca²⁺ with 100 μ M ADPR via the patch pipette. The extracellular solution contained 1 mM Ca²⁺. **(A)** Maximum outward currents at +15 mV. Shown is the mean of five measurements per group. Significance compared to untransfected group (Dunnett test) indicated by ns (not significant) or *** ($p < 0.001$). **(B)** Kinetics of outward current at +15 mV from representative measurement. Color code as in (C). **(C)** Current-voltage relationship obtained from the voltage ramp (between -85 mV and +20 mV) where maximum current was observed (see panel (B)).

During the experiments, neither mutant evoked a current comparable to the wild type protein, indicating that a properly folded Zn²⁺-binding site is required for channel activity. Taken together, the novel motif is crucial for protein folding, which subsequently probably affects channel gating.

3.1.7 Calmodulin (CaM) binds to *drMHR1/2*

The isolated *drMHR1/2* domain, which was used for the identification of the Zn²⁺-binding site, was further analyzed regarding its interaction with CaM. An IQ-like motif in the MHR1/2 domain responsible for CaM-binding was identified in *hsTRPM2* (Tong et al., 2006). This motif is predominantly conserved in the zebrafish orthologue. In order to decipher its functional role, the binding of CaM to *drMHR1/2* was biophysically analyzed. Microscale thermophoresis showed clear binding of Ca²⁺-CaM to *drMHR1/2* in the micromolar range (Figure 3.11). Due to the fact that CaM does not contain any tryptophan or tyrosine residues affecting the measurement, label-free MST was used which relies on the intrinsic tryptophan fluorescence of *drMHR1/2*. Binding parameters were unaffected when the protein was pre-saturated with the ligands ADPR or 2'-deoxy-ADPR.

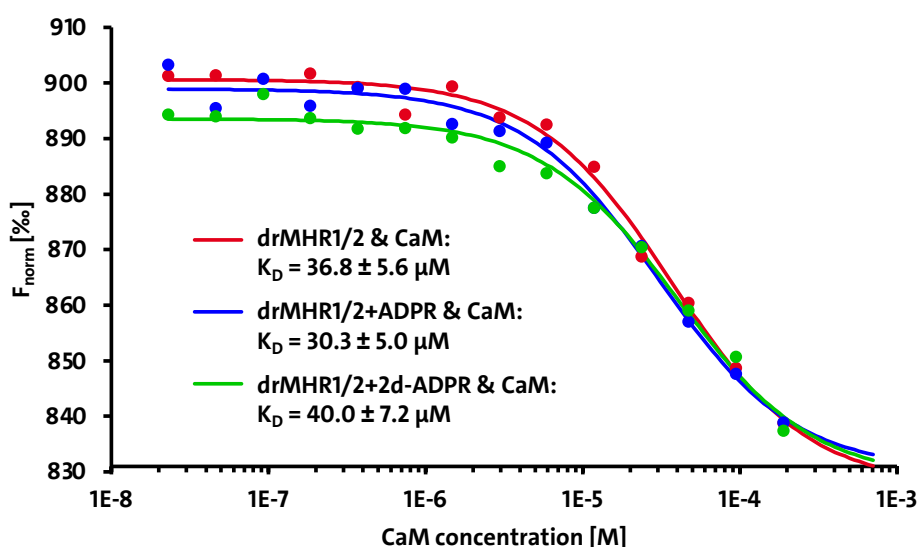


Figure 3.11: Ca²⁺-CaM binds to *drMHR1/2* independently of ADPR or 2'-deoxy-ADPR. Binding of Ca²⁺-CaM to *drMHR1/2* as shown by label-free microscale thermophoresis (MST), *drMHR1/2* (500 nM) was either used in apo form or pre-incubated with ADPR / 2'-deoxy-ADPR (2d-ADPR) (500 μM). Buffer contained 5 mM Ca²⁺.

Moreover, the *drMHR1/2*-CaM interaction was shown by SEC (Figure 3.12): When the two binding partners were mixed before the injection onto the column, the observed peak eluted earlier compared to *drMHR1/2* alone. This indicates that CaM binds to *drMHR1/2* and the complex consequently has a larger molecular weight than apo-*drMHR1/2*. Since CaM was applied with five times molar excess compared to *drMHR1/2* to ensure saturation, unbound CaM also eluted from the column when the complex sample was injected.

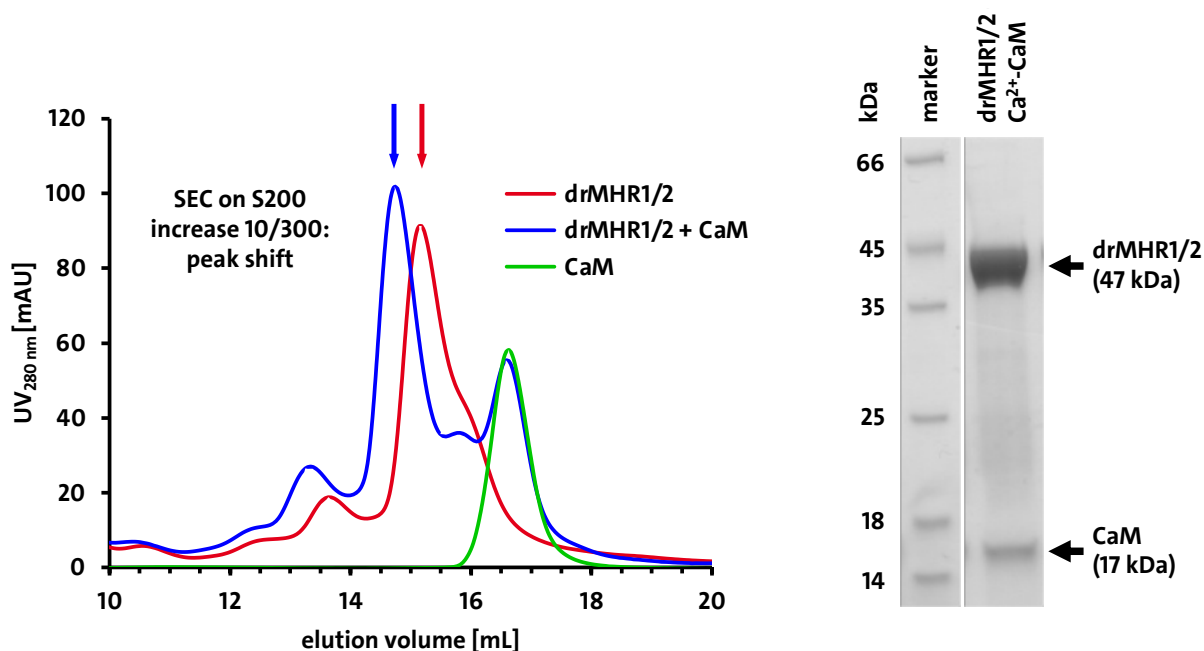


Figure 3.12: Ca²⁺-CaM binds to *drMHR1/2* which leads to an increase in size. Binding of Ca²⁺-CaM to *drMHR1/2* as shown by SEC on an S200 increase 10/300 column by peak shift (*drMHR1/2*: 15.1 mL, *drMHR1/2* + CaM: 14.7 mL), *drMHR1/2* (120 μ M) and CaM (600 μ M) were run in the presence of 5 mM Ca²⁺ either individually or pre-incubated together before injection. SDS-PAGE (4-20%) inlet shows the peak fraction of the complex (indicated by blue arrow in chromatogram) with bands for *drMHR1/2* and CaM (Coomassie-stained).

The *drMHR1/2*-CaM interaction was further investigated by size exclusion chromatography small-angle X-ray scattering (SEC-SAXS). For this, the peaks obtained from SEC (see Figure 3.12) were directly subjected to SAXS analysis. The raw buffer-subtracted SAXS data revealed visible changes in the low q -range upon CaM addition to *drMHR1/2*, indicating alterations of the overall particle shape (Figure 3.13 A). The distance distribution function also suggests slight conformational changes within the molecule due to different profiles of the right shoulder of the curves (Figure 3.13 B).

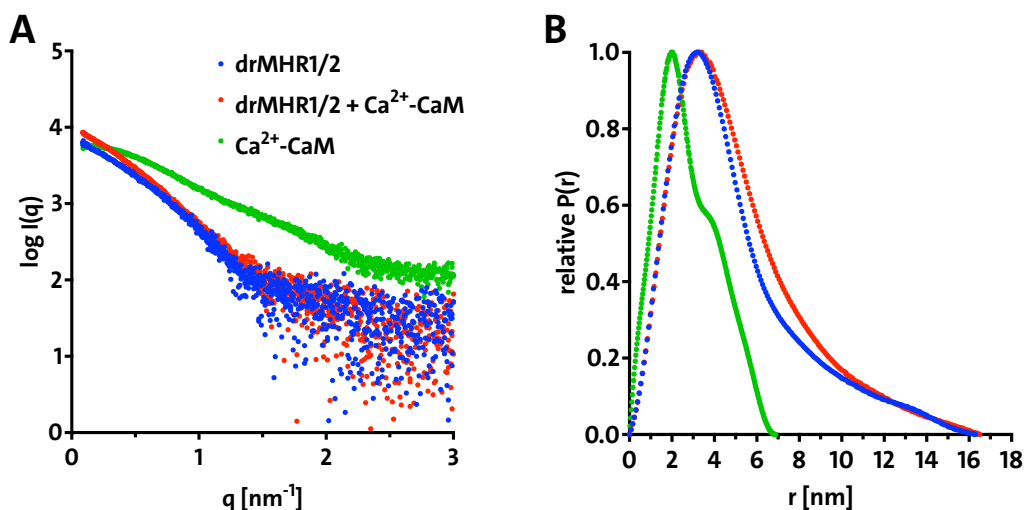


Figure 3.13: SAXS analysis of the *drMHR1/2*-CaM interaction. (A) Size exclusion chromatography small-angle X-ray scattering (SEC-SAXS) raw data of buffer-subtracted samples. **(B)** Distance distribution plot as calculated from the raw data by the program GNOM. Same color code as in (A).

Quantitative analysis of the SAXS data show that the molecular weight estimate of *drMHR1/2* alone roughly fits the actual value of the monomeric state. The data supports the idea that *drMHR1/2* and CaM form a complex since molecular weight and the Porod volume both increase when CaM is added to *drMHR1/2* (Table 3.1). The maximal protein diameter and the radius of gyration are relatively unchanged which points to intramolecular changes upon CaM binding. Taken together, the experiments showed that the isolated MHR1/2 domain of zebrafish TRPM2 binds CaM.

Table 3.1: SEC-SAXS analysis of the *drMHR1/2*-CaM interaction. Radii of gyration (R_g), Porod volumes (V_{Porod}) and molecular weight estimates (MW) were calculated from buffer-subtracted scattering curves via the Guinier approximation. The distance distribution function ($P(r)$) which yielded the maximal protein dimension (D_{max}) was obtained from the entire scattering curve using the program GNOM.

Sample	R_g [nm]	D_{max} [nm]	V_{Porod} [\AA^3]	MW [kDa]
Ca ²⁺ -CaM	2.1	6.9	21,024	15.9
<i>drMHR1/2</i>	3.6	16.3	78,539	62.4
<i>drMHR1/2</i> -CaM complex	3.7	16.5	109,648	85.7

3.1.8 Expression and purification of a TRPM2-CaM complex for cryo-EM

The influence of CaM on TRPM2 was further analyzed in the context of the full-length channel. In order to investigate the interaction in detail, *hsTRPM2* was expressed in HEK293S GnTI⁻ cells. This human cell line exhibits no N-acetyl-glucosaminyltransferase I (GnTI) activity and consequently lacks complex N-glycans, which is of advantage for structural studies since it reduces structural heterogeneity. Two constructs with a C-terminal His₆-EGFP or His₆-MBP tag were cloned into the pEG BacMam plasmid and tested for expression rates in adherent HEK293S GnTI⁻ cells by transient transfection (Figure 3.14). The construct with the EGFP tag indicated a higher expression rate in this cell line. In contrast to untagged *hsTRPM2*, both variants only showed a *hsTRPM2* monomer band and no *hsTRPM2* tetramer band.

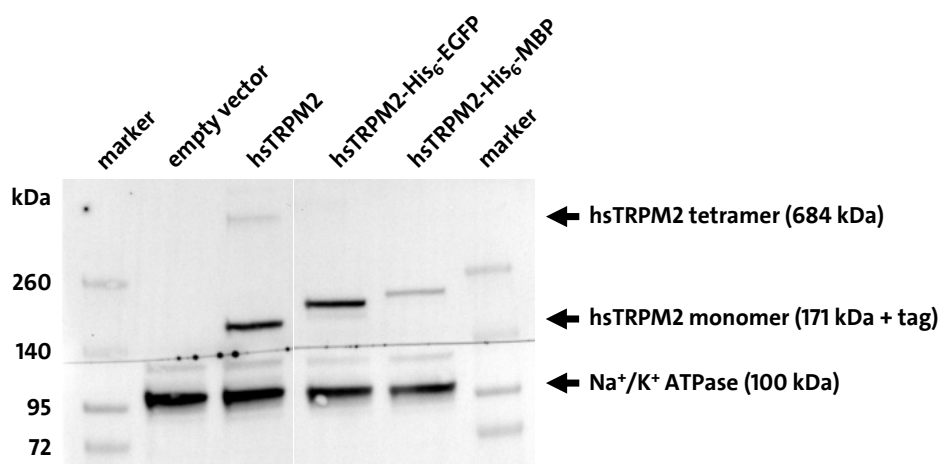


Figure 3.14: Expression tests of *hsTRPM2* in adherent HEK293S GnTI⁻ cells. HEK293S GnTI⁻ cells were transiently transfected with different *hsTRPM2* constructs in pEG BacMam: *hsTRPM2* (171 kDa), *hsTRPM2*-His₆-MBP (213 kDa), *hsTRPM2*-His₆-EGFP (200 kDa). Analysis by whole-cell lysis with 2% DDM and subsequent western blot (after SDS-PAGE (4-20%) separation). Detection of *hsTRPM2* (upper part of blot) and Na⁺/K⁺ ATPase (lower part of blot, loading control).

Both constructs were transformed into DH10BacTM *E. coli* to generate bacmids encoding for a BacMam virus which was used for large-scale protein expression in mammalian cells. Adherent Sf9 insect cells were transfected with the bacmids to induce BacMam P1 virus production. High-titer P2 virus was generated by re-infecting dense Sf9 suspension cell cultures with virus from the adherent cells. Due to a construct-independent EGFP control behind an insect P10 promoter on the backbone of pEG BacMam, virus

production could be followed by EGFP fluorescence of Sf9 cells. The virus originating from the construct with the EGFP tag was used for infection of HEK293S GnTI- suspension cell cultures since it showed a higher virus titer compared to the MBP-tagged construct (Figure 3.15, Sf9). This variant further showed a higher expression rate in the adherent cell tests (cf. Figure 3.14) and also simplified tracing of the subsequent purification due to the fluorescent EGFP tag on the protein. The target construct was predominately expressed in the cell membrane of the suspension HEK293S GnTI- cells (Figure 3.15, HEK293S GnTI-).

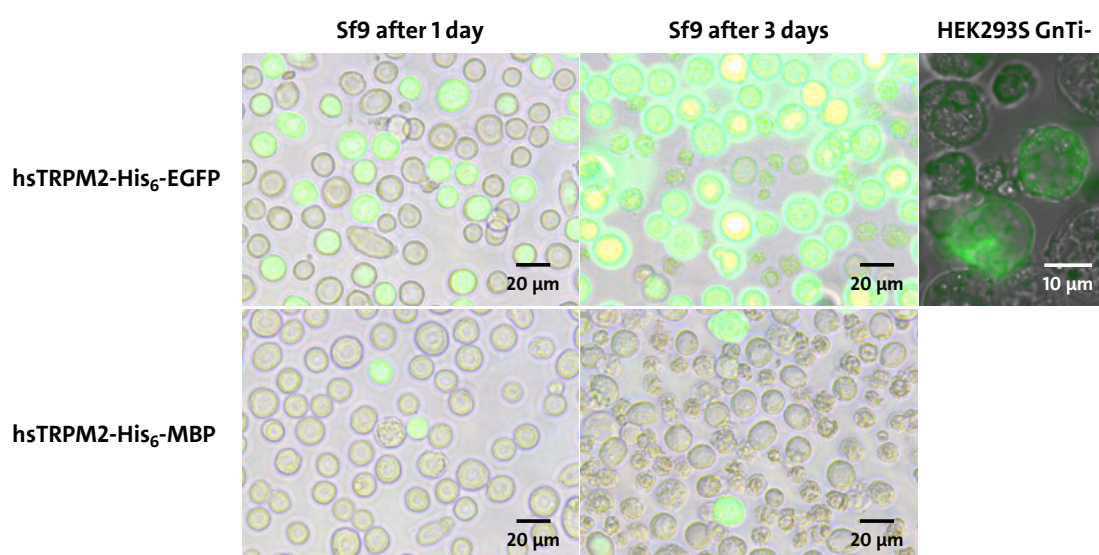


Figure 3.15: BacMam virus production and *hsTRPM2* expression. BacMam P2 virus production in Sf9 suspension cells 1 day and 3 days after infection with P1 virus. *hsTRPM2-His₆-EGFP* has a higher virus titer compared to *hsTRPM2-His₆-MBP* due to more cells showing EGFP fluorescence (indicating virus infection due to EGFP behind P10 promoter on pEG BacMam). *hsTRPM2-His₆-EGFP* P2 virus was used to infect HEK293S GnTI- cells to express the protein, which is found in the cell membrane. Overlay of bright field microscopy with EGFP fluorescence.

Purification was carried out in glyco-diosgenin (GDN) detergent after membrane isolation by ultracentrifugation. Since IMAC trials were unsuccessful, probably due to inaccessibility of the His₆-tag, the protein was purified using an anti-GFP nanobody coupled to sepharose beads via GST. After elution from the beads with glutathione and the addition of excess Ca²⁺-CaM, the tetrameric CaM-*hsTRPM2*-EGFP-nanobody-GST complex (~1,000 kDa) was further purified by SEC (Figure 3.16). The proteins eluted in multiple peaks, but the peak corresponding to the expected molecular weight (peak “1”)

contained both *hs*TRPM2-EGFP and nanobody-GST. Unfortunately, CaM was not detected as a part of this peak and thus TRPM2 and CaM did not seem to form a stable complex in these conditions. Furthermore, multiple other bands of smaller molecular weights indicated proteolytic activity which requires optimization of the purification process. Nevertheless, analysis by negative-stain electron microscopy revealed particles of the expected size for TRPM2 (~20 nm) amongst visible aggregates (Figure 3.17).

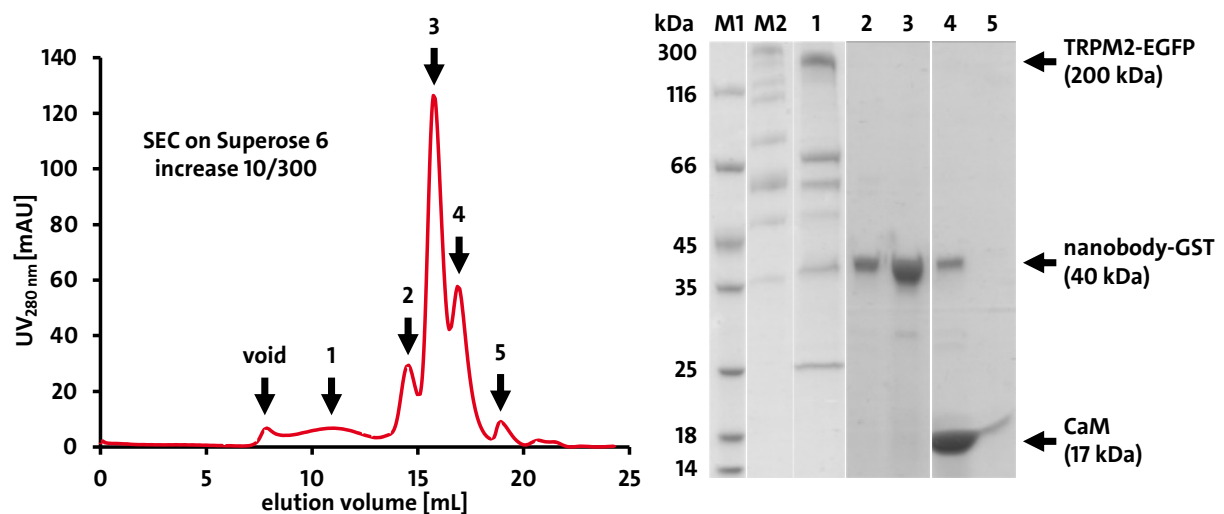


Figure 3.16: Purification of *hs*TRPM2-CaM complex. SEC profile of CaM-*hs*TRPM2-EGFP-nanobody-GST on an S6 increase 10/300 column. Peaks are numbered and the corresponding fractions were analyzed by SDS-PAGE (4-20%, Coomassie-stained). Peak “1” corresponds to the expected size of the tetrameric complex (~1,000 kDa) and reveals bands for *hs*TRPM2-EGFP (200 kDa), nanobody-GST (40 kDa) and multiple proteolysis products. M1, M2: marker.

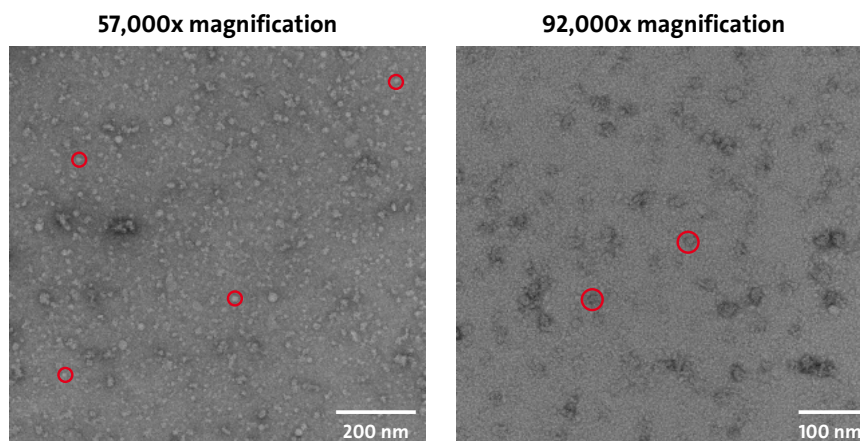


Figure 3.17: Analysis of *hs*TRPM2 by negative-stain electron microscopy. The sample was applied onto a carbon-coated grid and stained with uranyl formate. Analysis in a TALOS 120C electron microscope at 57,000x and 92,000x magnification revealed particles of the expected size (20 nm, examples marked with red circles) and aggregates.

3.1.9 Expression, purification and characterization of the NUDT9-H domain

Besides the N-terminal MHR1/2 domain, the C-terminal NUDT9-H domain of TRPM2 can also act as a nucleotide-binding site and can consequently bind or even hydrolyze the pyrophosphate in ADPR. Its role varies between different TRPM2 orthologues (Kühn et al., 2016). In order to improve the understanding of its modulatory function, isolated NUDT9-H domains from different species were expressed and purified. The work with human NUDT9-H (*hsNUDT9-H*) was performed by former Tidow lab member Ellen Gattkowski and is mostly published (Gattkowski et al., 2019). Unfortunately, no binding of ADPR or 2'-deoxy-ADPR to *hsNUDT9-H* could be detected by means of any biophysical method (Gattkowski, unpublished). In this study, the respective domain from zebrafish (*drNUDT9-H*) was expressed in BL21 Gold pLysS *E. coli* and purified by IMAC. Subsequent SEC purification resulted in a pure, stable sample with a melting temperature of 45.6°C (Figure 3.18). The SEC elution volume indicated a multimeric, probably tetrameric, form of *drNUDT9-H*.

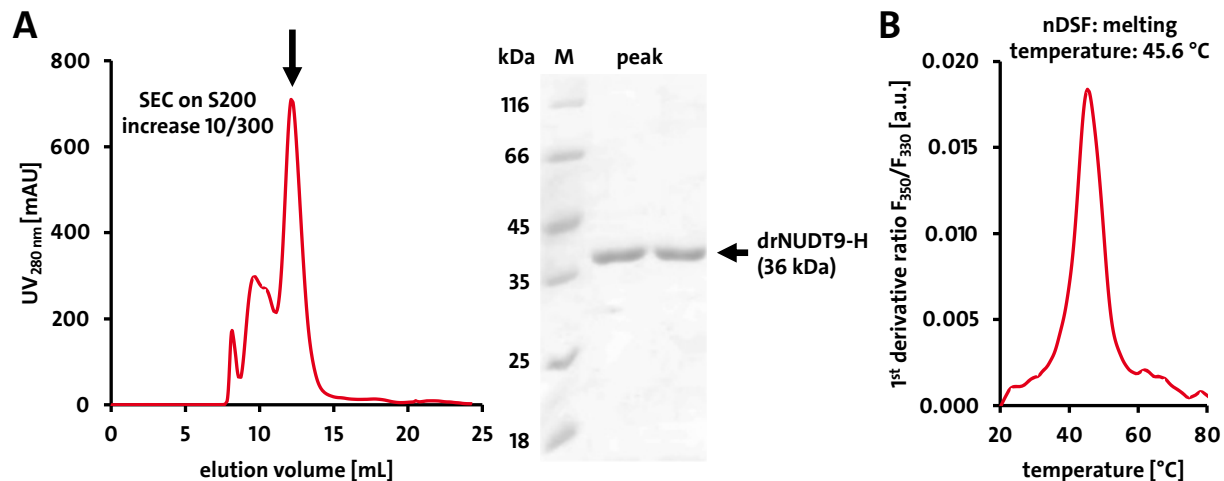


Figure 3.18: Purification and thermal stability of *drNUDT9-H*. (A) SEC profile of *drNUDT9-H* on an S200 increase 10/300 column with a peak at ~12.5 mL (indicated by arrow) that corresponds to a multimeric form of *drNUDT9-H* (~150 kDa according to the column manufacturer's manual). SDS-PAGE analysis (with Coomassie staining) of the indicated peak shows pure *drNUDT9-H* (36 kDa). M: marker. (B) nDSF melting analysis of 14 μ M *drNUDT9-H*. First derivative of fluorescence intensity ratio F₃₅₀/F₃₃₀ with maximum at 45.6°C (melting temperature).

The purified *dr*NUDT9-H protein was further characterized regarding ligand binding by nDSF titrations with ADPR / 2'-deoxy-ADPR and by ITC with ADPR (Figure 3.19). There was no evidence of the nucleotides binding to *dr*NUDT9-H, comparable to the data that was collected for isolated *hs*NUDT9-H (Gattkowski, unpublished).

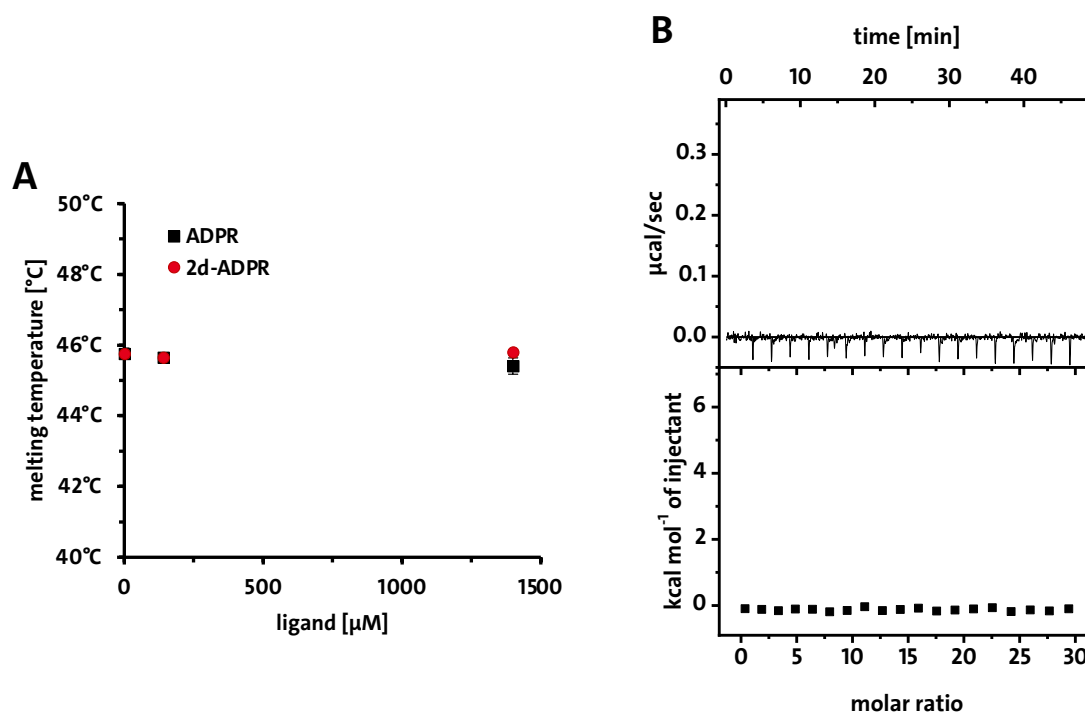


Figure 3.19: ADPR and 2'-deoxy-ADPR do not bind to isolated *dr*NUDT9-H. (A) No shift of melting temperatures (duplicates) of *dr*NUDT9-H upon addition of ADPR / 2'-deoxy-ADPR (2d-ADPR). (B) ITC measurement of *dr*NUDT9-H (10 μM) and ADPR (1500 μM) shows no binding.

While *hs*NUDT9-H in the context of the full-length channel in fact binds ADPR, the NUDT9-H domain of the invertebrate *nv*TRPM2 channel further exhibits catalytic function and cleaves ADPR to AMP and ribose 5-phosphate (Kühn et al., 2016). To assess whether *dr*NUDT9-H also possesses hydrolase activity, the protein was incubated with ADPR and 2'-deoxy-ADPR before subsequent HPLC analysis of the resulting nucleotide products (Figure 3.20). The experiment suggested no or very small catalytic activity due to unaltered nucleotide peak intensities after incubation with *dr*NUDT9-H. Although the AMP/2'-deoxy-AMP levels slightly increased, the changes were minor when compared to the active hydrolase NUDT9, which exhibits major changes after already six minutes (Gattkowski et al., 2021).

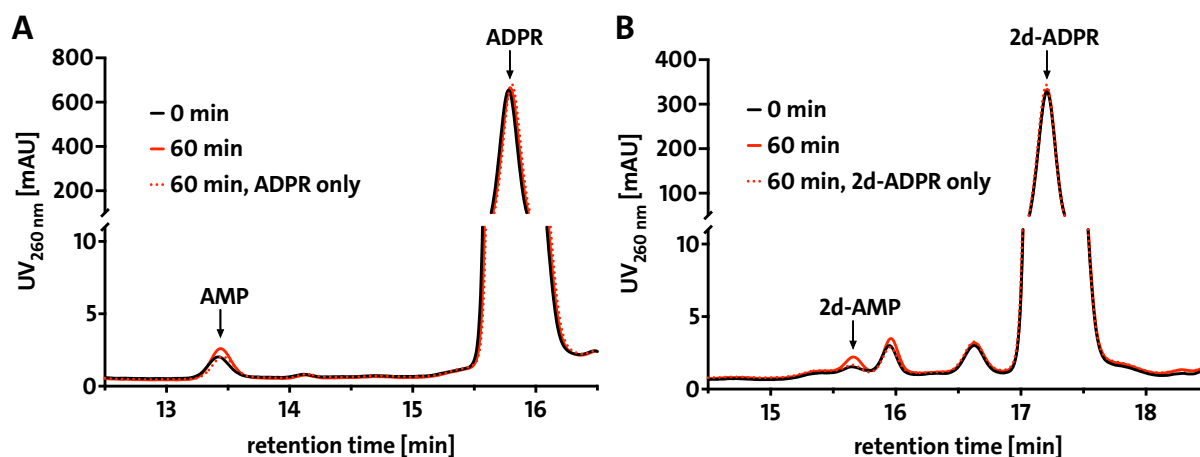


Figure 3.20: HPLC analysis of hydrolase assay with *dr*NUDT9-H. (A) HPLC profile after hydrolase assay of *dr*NUDT9-H and ADPR. AMP and ADPR peaks are shown at 0 min and 60 min incubation with *dr*NUDT9-H, ADPR only trace shows autocatalytic cleavage of ADPR after 60 min. (B) HPLC profile after hydrolase assay of *dr*NUDT9-H and 2'-deoxy-ADPR (2d-ADPR). 2'-deoxy-AMP (2d-AMP) and 2d-ADPR peaks are shown at 0 min and 60 min incubation with *dr*NUDT9-H, 2d-ADPR only trace shows autocatalytic cleavage of 2d-ADPR after 60 min.

Taken together, the isolated NUDT9-H domain of zebrafish TRPM2 does not seem to bind ADPR or 2'-deoxy-ADPR and exhibits no catalytic activity.

3.2 Discussion

The ion channel TRPM2, which is involved in various physiological processes such as the oxidative stress response and temperature sensing, is activated by the adenine nucleotide ADPR (Perraud et al., 2001). In this study, the two nucleotide-binding domains of TRPM2 (N-terminal MHR1/2 and C-terminal NUDT9-H) were expressed in soluble forms and biophysically characterized. The isolated human (Gattkowsky, unpublished) and zebrafish (this dissertation) NUDT9-H domains did not reveal interactions with ADPR. While the MHR1/2 domain of human TRPM2 (*hsMHR1/2*) did not express in *E. coli*, the zebrafish orthologue (*drMHR1/2*) was successfully purified and characterized.

3.2.1 2'-deoxy-ADPR is no superagonist of zebrafish TRPM2

Besides ADPR, the human TRPM2 channel (*hsTRPM2*) is also activated by the superagonist 2'-deoxy-ADPR, which induces significantly higher currents than ADPR (Fliegert et al., 2017b). The work of this dissertation revealed that not only ADPR, but also 2'-deoxy-ADPR binds to isolated *drMHR1/2*, emphasizing the role of the N-terminal domain as a conserved nucleotide binding site. Its importance was shown before for *hsTRPM2*, *drTRPM2* and *nvTRPM2* by structural (Huang et al., 2018, 2019) as well as by functional studies (Kühn et al., 2016, 2019a; Riekehr et al., 2022; Tóth et al., 2020).

Both agonists showed similar binding parameters regarding the interaction with *drMHR1/2* (Figure 3.2). While the experiments revealed for the first time that 2'-deoxy-ADPR binds to the N-terminal domain of TRPM2, they provide no explanation for a potential superagonistic effect of 2'-deoxy-ADPR on *drTRPM2*. These results are published (Sander et al., 2022a) and additional whole-cell patch clamp studies by co-author Jelena Pick revealed further information in context of full-length *drTRPM2*. In line with another study (Kühn et al., 2019a), the zebrafish orthologue exhibited much higher currents than *hsTRPM2* upon infusion of ADPR, leading to cell rupture. In order to decrease current amplitudes, extracellular Ca^{2+} was reduced. Under these measurable conditions ADPR and 2'-deoxy-ADPR did not induce significantly different maximum currents, indicating that while 2'-deoxy-ADPR is a superagonist of *hsTRPM2*, it does not have this effect on *drTRPM2* (Sander et al., 2022a).

This difference between *dr*TRPM2 and *hs*TRPM2 could be based on different binding affinities of *dr*MHR1/2 and *hs*MHR1/2 for ADPR and 2'-deoxy-ADPR. Besides the biophysical binding data of the isolated *dr*MHR1/2 domain obtained in this study, the respective experiments with isolated *hs*MHR1/2 would allow more insight. Unfortunately, despite 62% sequence identity and 74% sequence similarity to *dr*MHR1/2 (according to sequence alignment), the human domain could not be purified. However, based on cryo-EM structures of *dr*TRPM2 (Huang et al., 2018) and *hs*TRPM2 (Huang et al., 2019) in complex with ADPR, it does not seem likely that the binding pocket within MHR1/2 is responsible for the difference. In both orthologues, ADPR is bound in a horseshoe-like conformation, interacting with homologous residues that are structurally arranged to form a conserved binding site (Figure 3.21). The 2'-hydroxyl group, that is absent in 2'-deoxy-ADPR, is exposed to the solvent and shows no obvious interactions with *dr*MHR1/2 or *hs*MHR1/2 (Figure 3.21). This suggests that the 2'-hydroxyl group has no impact on ADPR binding to MHR1/2. Consequently, 2'-deoxy-ADPR presumably binds to the MHR1/2 domain of both orthologues in the same configuration as ADPR and the modified ligand induces the same conformational changes as ADPR.

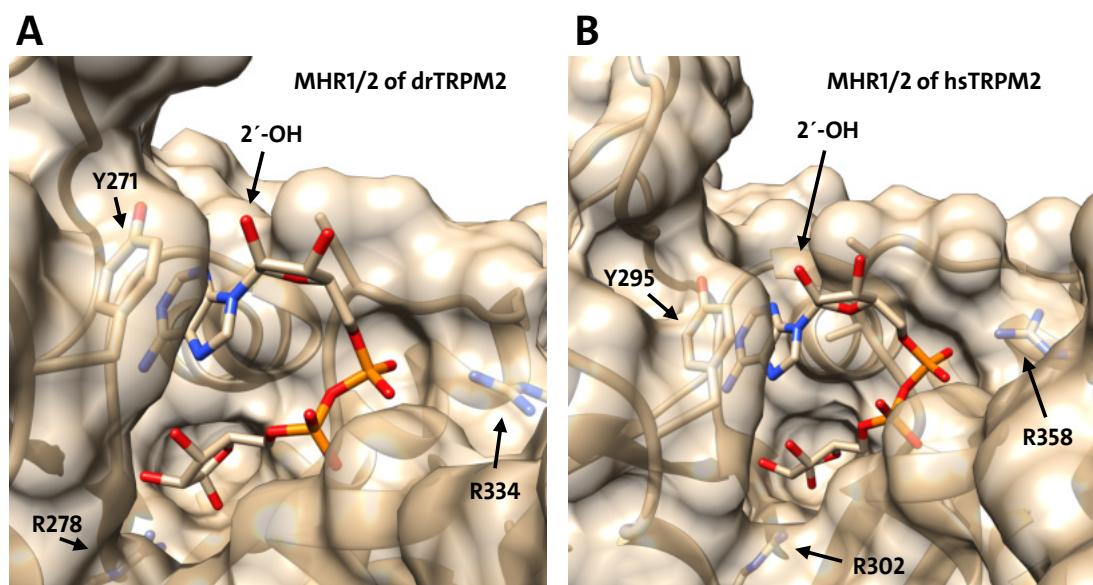


Figure 3.21: The 2'-hydroxyl group of ADPR is exposed in MHR1/2. ADPR bound to TRPM2 in MHR1/2 in the horseshoe-like conformation. The 2'-hydroxyl is marked (2'-OH) and is exposed to the solvent. Interacting residues are marked: Y271 (*dr*TRPM2) / Y295 (*hs*TRPM2) stacks with the adenine moiety, R278 (*dr*TRPM2) / R302 (*hs*TRPM2) interacts with the terminal ribose, R334 (*dr*TRPM2) / R358 (*hs*TRPM2) interacts with the α -phosphate. Cartoon depiction with transparent surface. **(A)** *dr*TRPM2 (PDB: 6DRJ (Huang et al., 2018)). **(B)** *hs*TRPM2 (PDB: 6PUS (Huang et al., 2019)).

In *hsNUDT9-H*, ADPR was structurally observed in a different molecular geometry (extended, Figure 3.22) compared to *hsMHR1/2* (horseshoe-like, cf. Figure 3.21). Thus, the two domains might contribute differently to channel activation (Huang et al., 2019). The 2'-hydroxyl group of ADPR bound to NUDT9-H of *hsTRPM2* points towards tyrosine 1485 (Figure 3.22). Although no direct interaction can be observed, it is feasible that this residue, which stacks with the adenine moiety of ADPR, is positioned closer to the ligand in case the 2'-hydroxyl group is missing since it would no longer be near the hydroxyl group of tyrosine. Thus, 2'-deoxy-ADPR binding to *hsNUDT9-H* could induce a conformational change that is different from the rigid-body rotation that is observed upon ADPR binding (Huang et al., 2019). This could further translate to a modified assisting function that NUDT9-H exerts during channel opening, possibly explaining the superagonistic effect of 2'-deoxy-ADPR on *hsTRPM2*.

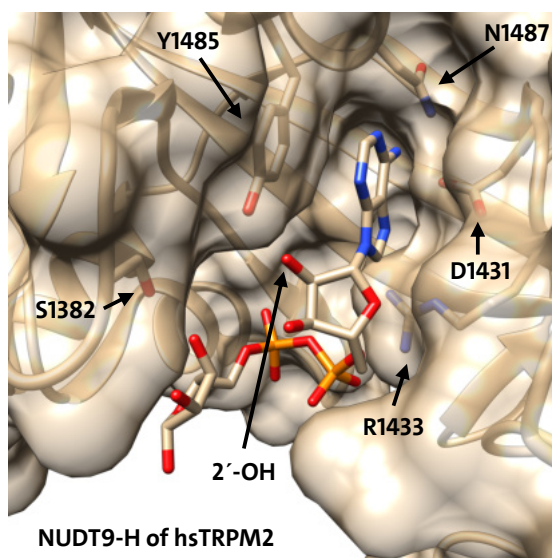


Figure 3.22: The 2'-hydroxyl group of ADPR is not exposed in *hsNUDT9-H*. ADPR bound to *hsTRPM2* in NUDT9-H in the extended conformation. The 2'-hydroxyl is marked (2'-OH) and points towards Y1485. All interacting residues are marked: S1382 interacts with the terminal ribose, Y1485 stacks with and N1487/D1431 interact with the adenine moiety, R1433 interacts with the adenine ribose. Cartoon depiction with transparent surface. PDB: 6PUS (Huang et al., 2019).

Unfortunately, no structural study so far could resolve an ADPR molecule within the NUDT9-H domain of *drTRPM2* due to its flexibility (Huang et al., 2018; Yin et al., 2019a). Nevertheless, it is possible that the NUDT9-H domain is responsible for the lack of the superagonistic effect of 2'-deoxy-ADPR on *drTRPM2* due to a different positioning of

both ligands in *dr*NUDT9-H compared to *hs*NUDT9-H. Additionally, this seems likely since NUDT9-H exhibits different functions in different TRPM2 orthologues: active enzyme in invertebrate TRPM2 (Kühn et al., 2016; Tóth et al., 2020) and channel-activating domain without enzymatic function in vertebrate TRPM2 (Iordanov et al., 2016, 2019; Kühn and Lückhoff, 2004). The lack of enzymatic function of *dr*NUDT9-H was also shown in this study (Figure 3.20). Although the NUDT9-H domains of *dr*TRPM2 and *hs*TRPM2 are both needed for channel activation, the two vertebrate channels differ in their response to some ADPR analogues that are assumed to bind to NUDT9-H: Two antagonists of *hs*TRPM2 with bulky, hydrophobic substitutions at the adenine C8 position (8-(3-acetyl-phenyl)-ADPR and 8-(thiophen-3-yl)-ADPR (Moreau et al., 2013)) act as agonists of *dr*TRPM2 (Kühn et al., 2019a). Moreover, inosine 5'-diphosphate ribose (IDPR), an ADPR analogue with a slightly modified adenine ring, is a partial agonist of *hs*TRPM2 (Kühn et al., 2019b) while it does not activate *dr*TRPM2 (Kühn et al., 2019a). Both examples imply a different role of NUDT9-H in the two orthologues.

In this work and previous studies by Ellen Gattkowsky, the isolated *hs*NUDT9-H and *dr*NUDT9-H domains did not seem to interact with ADPR or 2'-deoxy-ADPR. While the human domain purified as a monomer (Gattkowsky, unpublished), the zebrafish variant purified in a multimeric, probably tetrameric form (Figure 3.18) which could alter ligand binding properties. Since *hs*NUDT9-H is proven to bind ADPR (Huang et al., 2019), the domain presumably needs a larger context, for example the neighboring MHR1/2 domain, to interact with its ligand. One study showed weak binding of ADPR to isolated *dr*NUDT9-H by MST (Wang et al., 2018). However, due to the flexibility of the domain in the zebrafish orthologue, it is unknown whether *dr*NUDT9-H, which is crucial for channel activation (Huang et al., 2018), in fact binds ADPR and 2'-deoxy-ADPR in context of full-length *dr*TRPM2.

Taken together, the biophysical binding experiments with isolated *dr*MHR1/2 laid the foundation for the discovery that 2'-deoxy-ADPR does not have a superagonistic effect on *dr*TRPM2. The underlying mechanisms when compared to *hs*TRPM2 remain unknown, but it is likely that the NUDT9-H domain is crucial for the difference rather than the MHR1/2 domain.

3.2.2 cADPR and 8-Br-cADPR do not interact with TRPM2

Besides ADPR and 2'-deoxy-ADPR, the two cyclic ADPR derivatives cADPR and 8-Br-cADPR as well as the *hs*TRPM2 antagonist 8-Br-ADPR were analyzed regarding binding to isolated *dr*MHR1/2.

8-Br-ADPR inhibits the activation of *hs*TRPM2 by ADPR (Moreau et al., 2013; Partida-Sanchez et al., 2007; Riekehr et al., 2022). Nevertheless, in the absence of ADPR, it can also act as a low-affinity partial agonist of *nv*TRPM2 (Tóth et al., 2020) and slightly increases currents compared to buffer controls in whole-cell patch clamp experiments with *hs*TRPM2 (Riekehr et al., 2022). Although its effect on *dr*TRPM2 is not known, ITC experiments in this study revealed binding to the isolated *dr*MHR1/2 domain with parameters similar to ADPR and 2'-deoxy-ADPR (Figure 3.3). Thus, an antagonistic (for ADPR activation)/partial agonistic effect comparable to the one on *hs*TRPM2 and *nv*TRPM2 is conceivable. Since the MHR1/2 domain contains a conserved nucleotide binding site (Lü and Du, 2020), 8-Br-ADPR presumably binds there in all orthologues. In *nv*TRPM2, where channel gating is independent from the NUDT9-H domain, binding of 8-Br-ADPR to MHR1/2 in fact induces the partial agonistic effect. The ADPR derivative is further hydrolyzed by the catalytically active NUDT9-H in this species (Tóth et al., 2020). It remains elusive how 8-Br-ADPR mechanistically functions in *hs*TRPM2 and *dr*TRPM2, where channel gating is dependent on NUDT9-H. Besides binding to MHR1/2, it is possible that NUDT9-H is also involved in enabling the antagonistic effect.

It is controversially discussed if the cyclic nucleotide cADPR activates TRPM2. Especially the structural findings of 8-Br-cADPR and ADPR in a horseshoe-like conformation bound to the MHR1/2 domain of *hs*TRPM2 suggest a direct modulatory role of cADPR on TRPM2 (Huang et al., 2019). However, in this study, the physiological ADPR derivative did not bind to isolated *dr*MHR1/2 (Figure 3.3). These results are published and additional whole-cell patch clamp experiments by first author Winnie Riekehr showed that cADPR does not activate *hs*TRPM2 under various conditions, neither alone nor in synergy with subthreshold concentrations of ADPR (Riekehr et al., 2022). The observed activating effects in the literature (Kolisek et al., 2005; Togashi et al., 2006; Yu et al., 2019) are probably due to contamination of commercial cADPR preparations by up to 21% ADPR,

depending on the supplier (Riekehr et al., 2022). In line with the data obtained for this thesis, when the contaminating ADPR is enzymatically hydrolyzed before the substance is used for electrophysiology, the pure cADPR does not activate *hs*TRPM2 (Heiner et al., 2006; Tóth and Csanády, 2010).

Although the cADPR derivative 8-Br-cADPR was modeled into MHR1/2 in a cryo-EM structure of *hs*TRPM2 (PDB: 6PUU (Huang et al., 2019)) and was shown to act as a *hs*TRPM2 antagonist (Kolisek et al., 2005; Riekehr et al., 2022), it did not reveal binding to the isolated *dr*MHR1/2 domain (Figure 3.3). Similarly to cADPR, 8-Br-cADPR is prone to hydrolysis and commercial preparations contain up to 19% 8-Br-ADPR impurities, depending on the supplier (Riekehr et al., 2022). Thus, the chemical used for the above-mentioned cryo-EM study (Santa Cruz Biotechnology, 95% purity according to scbt.com) presumably contained significant amounts of 8-Br-ADPR. Since it was used at 25x excess compared to the protein (1 mM 8-Br-cADPR to 40 μ M *hs*TRPM2 (Huang et al., 2019)), it is possible that the density within MHR1/2 corresponds to 8-Br-ADPR in a horseshoe-like conformation rather than to 8-Br-cADPR. The local resolution (~ 4 Å (Huang et al., 2019)) does not allow the reliable identification of either nucleotide and 8-Br-ADPR also fits into the density of the corresponding cryo-EM map (EMDB: 20482, Figure 3.23).

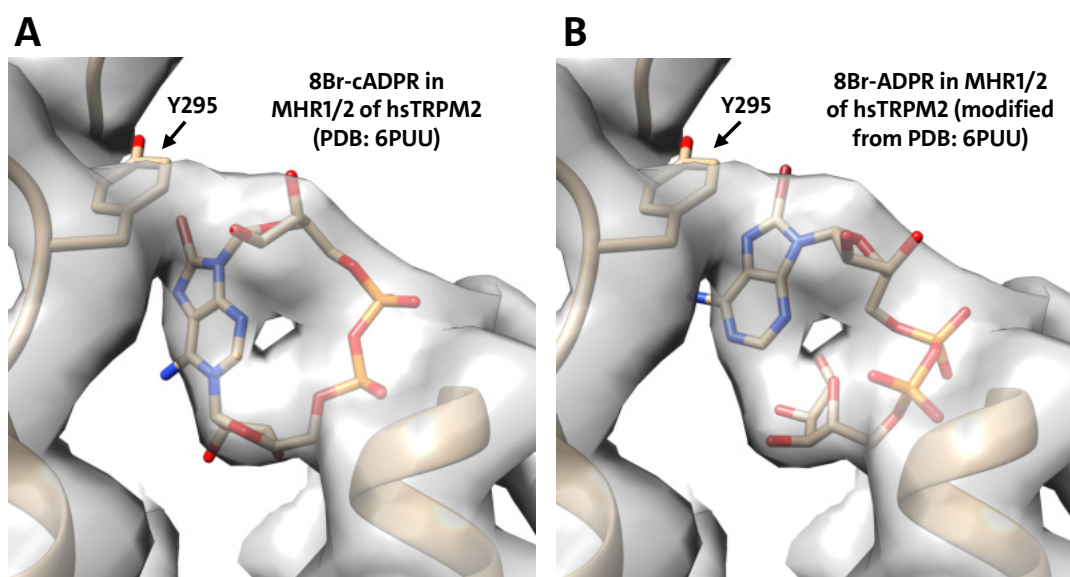


Figure 3.23: 8-Br-cADPR and 8-Br-ADPR both fit into the density of EMDB 20482. Cryo-EM map of nucleotide binding site in MHR1/2 is shown as grey transparent surface (local resolution: ~ 4 Å) with protein in cartoon representation and ligands as atom model. **(A)** Original model with 8-Br-cADPR (PDB: 6PUU (Huang et al., 2019)). **(B)** Modified model with 8-Br-ADPR which also fits into the density.

Consequently, 8-Br-cADPR might not bind to TRPM2. The observed antagonistic effects in electrophysiology could be explained by the rapid hydrolysis to 8-Br-ADPR in the patched cells (Riekehr et al., 2022). Taken together, while 8-Br-ADPR was confirmed to interact with TRPM2, the data suggests that both cyclic nucleotides (cADPR and 8-Br-cADPR) do not.

3.2.3 Conserved Zn²⁺-binding domain in MHR1/2

The isolated *dr*MHR1/2 domain was analyzed by X-ray crystallography and the resulting structure superimposed well with the MHR1/2 domain of apo-*dr*TRPM2 (PDB: 6DRK (Huang et al., 2018), cf. Figure 3.5). Co-crystallization and crystal soaking with ADPR/2'-deoxy-ADPR failed, probably due to the structural rearrangements that MHR1/2 undergoes upon ADPR binding: A closing movement of the bi-lobed structure of the MHR1/2 domain by 7-8° has been reported for both *dr*TRPM2 (Huang et al., 2018) and *hs*TRPM2 (Huang et al., 2019).

The structure of apo-*dr*MHR1/2 revealed a so far unrecognized domain responsible for the coordination of a Zn²⁺ ion (Figure 3.6). The residues involved in ion coordination are evolutionarily conserved between TRPM2 sequences from invertebrates to mammals (Figure 3.7), indicating physiological relevance of the motif which was not resolved in any previous *dr*TRPM2 structure (Huang et al., 2018; Yin et al., 2019a). Although the domain was modeled as a backbone trace in cryo-EM structures of *hs*TRPM2, the low local resolution of ~5-6 Å (compared to 2.0 Å of the crystal structure) presumably did not allow the identification of the Zn²⁺-coordinating site (Huang et al., 2019). Another structural study concerning *hs*TRPM2 not only modeled the backbone of the domain but also contained side chain information with a different fold compared to the *dr*MHR1/2 crystal structure (Wang et al., 2018). However, due to the local resolution of ~4-6 Å this information does not seem completely reliable, explaining why the Zn²⁺-binding site was not identified.

In this study, the structural and functional importance of the newly identified site for isolated *dr*MHR1/2 as well as for *hs*TRPM2 was assessed by mutations of the Zn²⁺-coordinating residues. Subsequent protein expression experiments as well as a cell

surface biotinylation assay showed that the motif seems to be crucial for correct protein folding and trafficking (Figure 3.8, Figure 3.9). In general, Zn^{2+} -binding domains are essential structural factors for many proteins (Kochańczyk et al., 2015). The novel domain in *drMHR1/2* is connected to the remaining MHR1/2 with a β -stem and both share a large connecting interface revealing substantial interactions (Figure 3.24, cyan/grey interface). Thus, the Zn^{2+} -binding domain presumably stabilizes the fold of the MHR1/2 domain which further influences TRPM2 stability.

Whole-cell patch clamp experiments with *hsTRPM2* Zn^{2+} -binding site variants showed that the site is additionally crucial for ADPR-activated channel function (Figure 3.10), suggesting that the intact Zn^{2+} -binding domain primes MHR1/2 for ADPR binding. It interacts with the loop 263-372 (287-297 in *hsTRPM2*) which contains the conserved tyrosine residue Y271 (Y295 in *hsTRPM2*). This residue stacks with the adenine base of ADPR and its derivatives upon binding to MHR1/2 (cf. Figure 3.21 (Huang et al., 2018, 2019)). Consequently, correct positioning of the loop possibly enables ligand binding to the domain and the subsequent closure of the bi-lobed shape that induces channel opening (Huang et al., 2018).

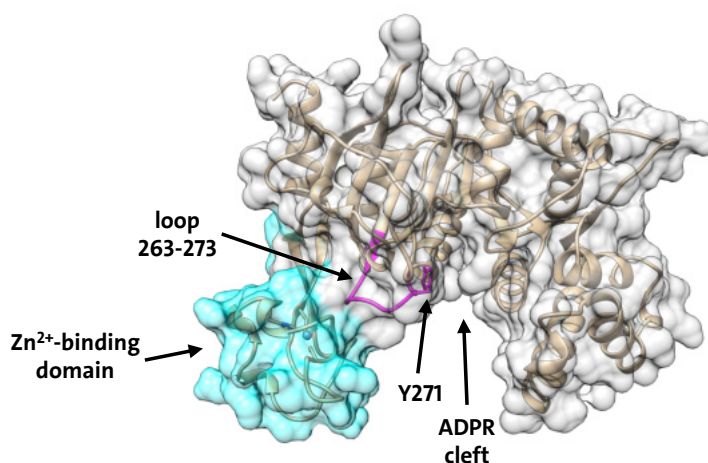


Figure 3.24: Importance of Zn^{2+} -binding site for MHR1/2 stability and ADPR binding. Zn^{2+} -binding domain (cyan surface) makes substantial interactions with the remaining part of the MHR1/2 domain (grey surface). The presence of the Zn^{2+} -binding domain in *drMHR1/2* leads to the correct positioning of loop 263-273 (magenta) containing the conserved tyrosine residue Y271 which stacks with the adenine moiety of ADPR once ADPR binds in its cleft (see PDB: 6DRJ). According to this model, the stabilization and loop positioning caused by the Zn^{2+} -domain primes the MHR1/2 domain for ligand binding.

Since the motif is not only conserved between TRPM2 orthologues but also within the TRPM family, the Zn²⁺-binding site probably exhibits its stabilizing function in the MHR1/2 domain of all TRPM members. Unfortunately, besides the two above-mentioned TRPM2 studies, no other available TRPM structure resolved the domain. The corresponding residues are missing in all available models, probably due to their exposed location on the outside of MHR1/2 (TRPM2 (Yin et al., 2019a; Zhang et al., 2018), TRPM4 (Autzen et al., 2018; Duan et al., 2018a; Guo et al., 2017; Winkler et al., 2017), TRPM7 (Duan et al., 2018b), TRPM8 (Diver et al., 2019; Yin et al., 2018, 2019b)). However, *AlphaFold2* predictions show that the Zn²⁺-coordinating side chains of all TRPM proteins (except TRPM5) cluster together closely (Jumper et al., 2021; Varadi et al., 2022). It remains elusive if the site also influences channel activity of other TRPM members similarly to its possible impact on ADPR positioning within MHR1/2 of TRPM2.

In addition to its structural function, Zn²⁺ coordination can also have catalytic or regulatory implications (Kochańczyk et al., 2015). Since free intracellular Zn²⁺ affects TRPM2 activity and the linked response to oxidative stress (Abuarab et al., 2017; Ye et al., 2014), the novel Zn²⁺-binding site in MHR1/2 could consequently play a role in cellular signaling pathways. However, this seems unlikely because a Zn²⁺-free variant of *drMHR1/2*, as mimicked with the Zn²⁺-binding site mutations, does not seem to be stable enough to enable flexible binding/unbinding processes.

Interestingly, the N-terminal region of human TRPC5 contains an intracellular Zn²⁺-binding site that also comprises one histidine and three cysteine residues and that is structurally similar to the novel site in TRPM channels (Wright et al., 2020). Functionally, it was shown that intracellular Zn²⁺ contributes to oxidative neuronal death through delayed Ca²⁺ influx via TRPC5 (Park et al., 2019). Whether the N-terminal Zn²⁺-binding site is the molecular reason for this observation is unknown. Its sequence is conserved between all TRPC members, but not related to the TRPM motif. It seems conceivable that the motifs in TRPC and TRPM channels share common functionalities.

Taken together, the crystal structure of *drMHR1/2* allowed the identification of a Zn²⁺-binding site that is conserved between TRPM2 members from various species and within the TRPM family. It is essential for structural integrity and channel activity of TRPM2.

3.2.4 TRPM2-CaM interaction

When activated by ADPR or ADPR derivatives, TRPM2 activity is regulated by binding of free Ca^{2+} to the transmembrane-cytosol interface and by CaM, a Ca^{2+} -sensing signaling protein (Csanády and Törőcsik, 2009; Starkus et al., 2007). Two CaM-binding motifs in *hsTRPM2* were shown to have functional roles in either channel activation (motif in MHR1/2 (Tong et al., 2006)) or temperature sensitivity (motif in NUDT9-H (Gatkowski et al., 2019)).

In this study, isolated *drMHR1/2* revealed binding to Ca^{2+} -CaM (Figure 3.11, Figure 3.12), confirming functionality of the IQ-like motif in the zebrafish orthologue. It remains unknown whether the interaction is Ca^{2+} dependent since all binding experiments were performed in presence of the cation. The motif is predominantly conserved between *hsTRPM2* (where it is Ca^{2+} dependent (Gatkowski, 2021)) and *drTRPM2*. Intramolecular changes of *drMHR1/2* upon CaM binding, as shown by SAXS (Figure 3.13), suggest that CaM also induces conformational changes when binding to the N-terminal domain in context of the full-length channel. Interestingly, as discussed in the dissertation of Ellen Gatkowski, the putative CaM-binding site corresponding to the IQ-like motif is not accessible in all published TRPM2 structures. CaM binding to the site would require substantial conformational rearrangements that are not structurally captured yet (Gatkowski, 2021).

CaM binding to the IQ-like motif in MHR1/2 influences channel gating by maintaining an open channel through a positive feedback mechanism (Tong et al., 2006). Nevertheless, as shown by MST experiments in this study, the *drMHR1/2*-CaM interaction is independent from ADPR or 2'-deoxy-ADPR binding to the isolated domain (Figure 3.11). Thus, the positive feedback mechanism and binding of ADPR and ADPR derivatives for initial channel activation seem to be independent from each other. Alternatively, their possible interplay could require a larger structural context with the neighboring NUDT9-H domain and the physiological tetrameric fold.

To gain more structural insight into CaM binding to full-length *hsTRPM2*, the purification of a complex for cryo-EM studies was attempted during the experimental work of this dissertation. While TRPM2 could be purified with proteolysis impurities that require

optimization of the purification, CaM did not bind to TRPM2 forming a stable complex (Figure 3.16). Since at least two binding sites exist in *hs*TRPM2 (Gatkowski et al., 2019; Tong et al., 2006), this indicates that the conditions were not ideal for complex formation and they also require optimization. While an existing complex structure of TRPV5 with CaM was created using a similar protocol that entails the addition of CaM at 2x excess before SEC (Dang et al., 2019), two other structural studies of TRP channel complexes with CaM were generated under constant presence of CaM in all purification buffers to saturate the samples (Singh et al., 2018; Vinayagam et al., 2020). It is possible that this method would also allow the successful purification of a TRPM2-CaM complex. The published complex structures of TRPC4, TRPV5 and TRPV6 show different binding modes: Up to four CaM molecules can bind to the rib helices of a TRPC4 tetramer, locking the channel in its closed state (Vinayagam et al., 2020). The TRPV5 channel exhibits a flexible stoichiometry (Dang et al., 2019) and TRPV6 can only bind one CaM molecule in its cytoplasmic cavity that induces the transition towards an inactivated state (Singh et al., 2018). All reported binding modes or even combinations of the different variants also seem conceivable for TRPM2.

Taken together, Ca²⁺-CaM binding to the IQ-like motif in the N-terminal MHR1/2 domain of TRPM2 was confirmed for the isolated zebrafish domain. The further elucidation of the structural and functional consequences of CaM binding to TRPM2 requires a TRPM2-CaM complex structure which could not be successfully generated in this study.

3.3 Perspective

The results of this dissertation shed light on many characteristics regarding the ligand-binding domains of TRPM2. However, some molecular mechanisms are still not fully understood and require further investigation.

While the isolated MHR1/2 domain of *dr*TRPM2 was thoroughly assessed, the purification of the human orthologue was not successful in *E. coli*. Expression in insect or mammalian cells might yield a functional and stable protein due to post-translational modifications that are not generated in bacteria. Biophysical characterization of isolated *hs*MHR1/2 would be expedient in order to understand the superagonistic effect of 2'-deoxy-ADPR on *hs*TRPM2, especially in comparison to *dr*TRPM2 (Sander et al., 2022a) and also *nv*TRPM2 (Tóth et al., 2020), where the ligand seems to lack this effect. Since the underlying molecular mechanism probably rather involves the NUDT9-H domain than the MHR1/2 domain, structural analysis of ADPR and 2'-deoxy-ADPR binding to the C-terminal domain is necessary. This problem needs to be addressed in context of the full-length protein because neither ADPR nor 2'-deoxy-ADPR showed binding to isolated *hs*NUDT9-H and *dr*NUDT9-H. Particularly, it needs to be elucidated if ADPR in fact binds to NUDT9-H of *dr*TRPM2 and if this potential process exhibits a different binding mode compared to the human orthologue. 2'-deoxy-ADPR is not resolved in any TRPM2 structure and its distinct effects on MHR1/2 and NUDT9-H are not fully understood. Ligand-bound structures would help understanding its role towards TRPM2 activation in all orthologues.

Another ADPR derivative with an unclear function is 8-Br-cADPR. While the endogenous adenine nucleotide cADPR does not bind to TRPM2, the 'cADPR antagonist' 8-Br-cADPR was modeled into a *hs*TRPM2 structure in an apo-like state (Huang et al., 2019). However, due to possible impurities, it appears possible that the density of the ligand does not correspond to 8-Br-cADPR but to 8-Br-ADPR. A re-assessed structure of *hs*TRPM2 in complex with pure 8-Br-cADPR would clarify if the cyclic nucleotide binds to the channel. Furthermore, a structure disclosing the detailed binding mode of 8-Br-ADPR would be advantageous in order to fully understand its antagonistic function on ADPR-induced TRPM2 activation.

The novel Zn²⁺-binding site in the MHR1/2 domain of TRPM channels was shown to be important for structural integrity and function of TRPM2. It is conserved within the TRPM family, but whether it has a similar impact on other TRPM channels needs to be confirmed experimentally. While it seems likely that it plays a structural role, the functional implications on channel gating could be different due to the different ligands and transported ions in different TRPM members. An example of a similar site in TRPC5 suggests a universal role of a Zn²⁺-binding domain in all TRP channels which also needs experimental confirmation, for example by further structural work on TRP channels other than TRPM and TRPC. In general, besides the structural role and its functional implications, Zn²⁺ can act as a second messenger indicating that the novel site could be involved in cellular signaling pathways. A central point in the elucidation of this possibility is the question if the Zn²⁺ ion can be dislodged without disrupting overall protein integrity. Initial trials with isolated *dr*MHR1/2 involving EDTA to remove the bound ion were unsuccessful, indicating very tight binding. This needs to be further addressed for full-length TRPM2 and for TRPM as well as for TRP channels in general. Finally, while this study provided some new insight into the TRPM2-CaM interaction, a complex structure is crucial in order to understand the regulatory role of CaM binding towards TRPM2 activity. Besides the optimization of the purification process before the analysis by cryo-EM, it could be possible to chemically cross-link modified CaM with TRPM2 in case the complex is not stable. Furthermore, time-resolved cryo-EM studies could help deciphering the complex formation process.

4 P2X7

This chapter is about the C-terminal ballast domain of P2X7. During the experimental work of this study, it was structurally and functionally characterized by various biophysical methods, especially regarding binding parameters towards calmodulin and GDP. The results are prepared for publication (Sander et al., 2022b) and were obtained by the author of this thesis, unless stated otherwise.

4.1 Results

4.1.1 P2X7 ballast domain (P2X7BD) contains two CaM-binding regions

Calmodulin (CaM) was shown to interact with rat P2X7 and a 1-5-16 CaM-binding motif (I541, L545, W556) was identified within the C-terminal ballast domain (P2X7BD) of the protein (Roger et al., 2008). Since it remains unknown whether CaM also influences human and mouse P2X7, a peptide-based isothermal titration calorimetry (ITC) approach was performed to identify the exact binding sites in all orthologues. Besides the known motif, one other sequence within the P2X7BD (1-14 motif, W575, Y588) was identified as a putative CaM-binding region due to the appropriate spacing of bulky, hydrophobic anchor residues (Tidow and Nissen, 2013). Corresponding peptides from human, mouse and rat were synthesized with overhangs on both ends to increase solubility. However, three of the peptides were insoluble. The remaining peptides (Figure 4.1 A, color-coded) were analyzed regarding their binding parameters towards CaM by ITC. All measurements were performed in the presence of Ca^{2+} because the analyzed CaM-binding motifs suggest that only the activated Ca^{2+} -CaM (with four bound Ca^{2+} ions) is recognized. The ITC experiments were executed by Isabel Müller (LMU Munich). All three peptides investigated (both motifs from mouse and one from human) revealed exothermic binding to Ca^{2+} -CaM in the low micromolar range (Figure 4.1 B-D), which suggests that not only rat P2X7 but also mouse and human P2X7 bind Ca^{2+} -CaM through motifs in the C-terminus.

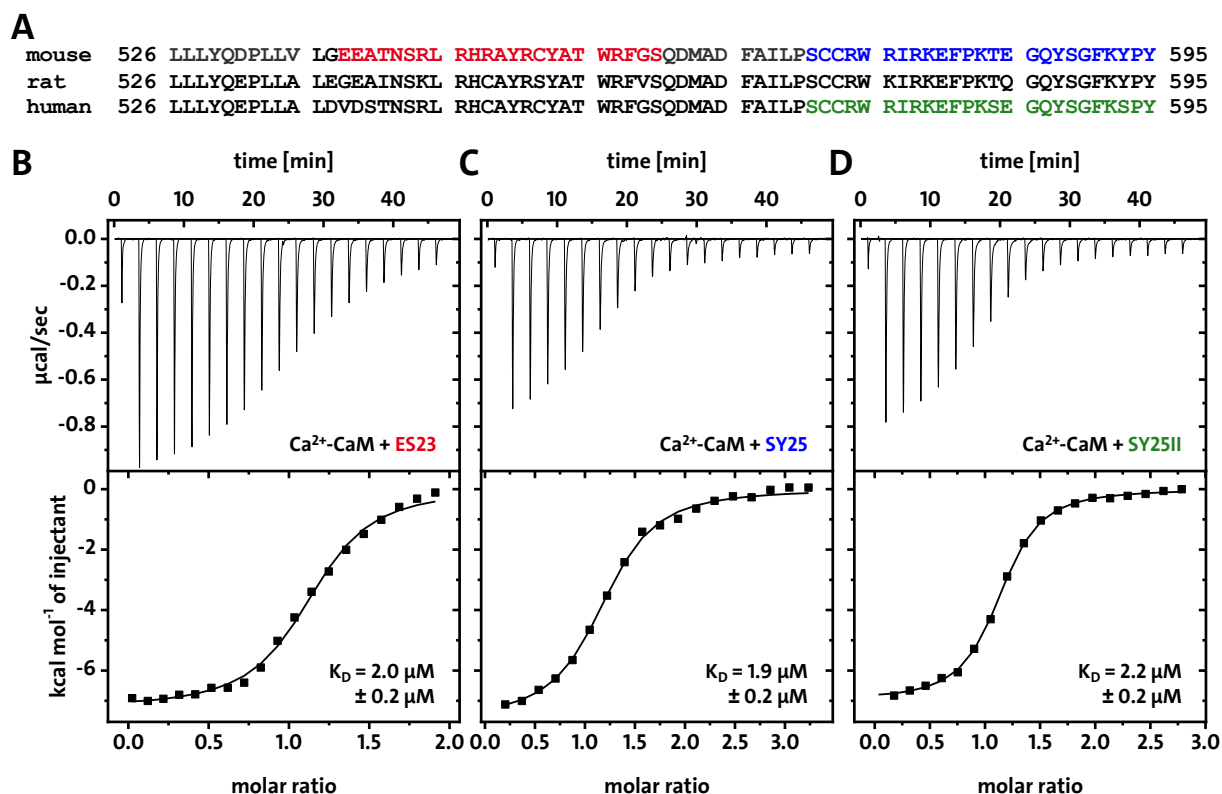


Figure 4.1: CaM-binding regions within the P2X7 ballast domain. (A) Partial sequence alignment of the P2X7 ballast domain from mouse, rat and human (residues 526-595). The soluble peptides used for ITC are colored and named by first and last amino acid alongside the length. **(B)-(D)** ITC measurements of Ca^{2+} -CaM (20 μM) and peptides (500 μM , color-codes refer to colored sequences in (A)) reveal exothermic binding in the low micromolar range. Same y-scales in all ITC panels.

4.1.2 Expression and purification of human P2X7 ballast domain (P2X7BD)

In order to assess the impact of the identified CaM-binding motifs in the protein context of the cytoplasmic part of P2X7, the entire C-terminus of human P2X7 including the cytoplasmic cap domain as well as the ballast domain (residues 355-595) was recombinantly expressed in different *E. coli* strains. Unfortunately, this construct did not seem to result in the production of a stable protein. During the purification by immobilized metal affinity chromatography (IMAC), only a faint band corresponding to the correct protein was observed (Figure 4.2 A). However, a prominent band of lower molecular weight could represent a proteolysis product of the target protein: the isolated P2X7 ballast domain (P2X7BD) without the cap-domain. To test if this domain alone could be purified, its sequence was cloned into an expression vector (pET-mCherry) and expression was carried out in Rosetta 2 *E. coli* cells. The subsequent purification by

two-step IMAC (classical as well as reverse after TEV cleavage of His₆-mCherry tag) and SEC resulted in a monodisperse, pure sample (Figure 4.2 B). The SEC elution volume indicated a trimeric form of *hsP2X7BD* (for simplicity subsequently termed: P2X7BD)

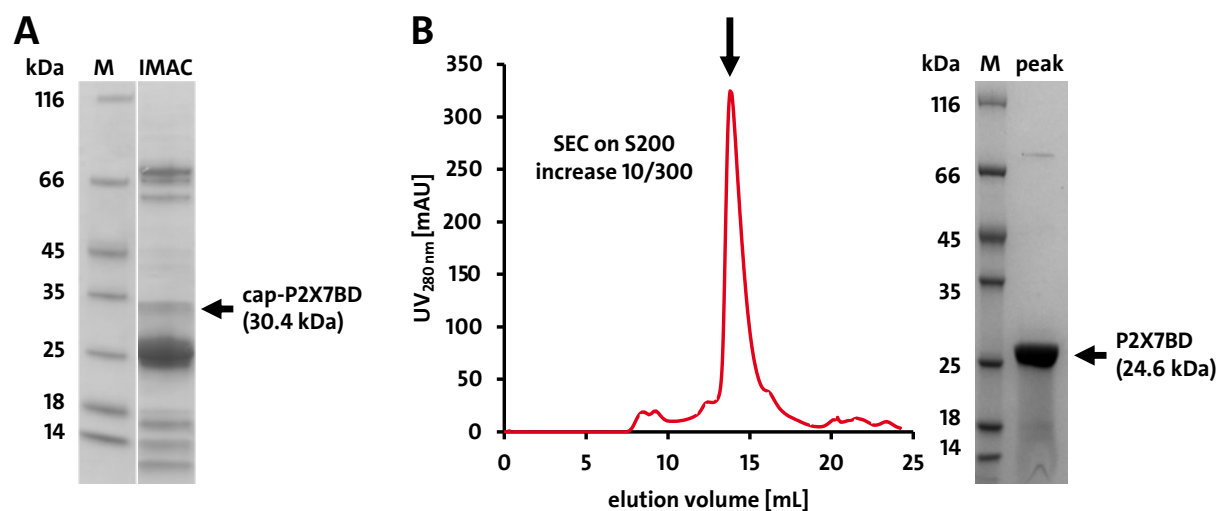


Figure 4.2: Expression and purification of human P2X7BD. (A) IMAC purification of cap-P2X7BD (30.4 kDa, residues 355-595 of *hsP2X7*) reveals only a faint band of the correct size. The main band probably corresponds to a proteolysis product: P2X7BD (24.6 kDa). SDS-PAGE analysis (4-20%), Coomassie-stained. M: marker. (B) SEC profile of P2X7BD (residues 395-595 of *hsP2X7*) on an S200 increase 10/300 column with a peak at ~14 mL (indicated by arrow) that corresponds to a trimeric form of P2X7BD (~74 kDa). SDS-PAGE analysis (4-20%, Coomassie-stained) of the indicated peak shows pure P2X7BD (24.6 kDa). M: marker.

4.1.3 Ca²⁺-CaM and GDP have opposite effects on the stability of P2X7BD

The stability of the isolated P2X7BD was analyzed by nDSF based on the intrinsic tryptophan fluorescence of the sample. The analysis revealed a single transition with an apparent melting temperature of 43.3°C, showing that the protein is stable in its trimeric form (Figure 4.3 A, red). Since the guanosine nucleotide GDP was identified within the ballast domain of a rat P2X7 structure (McCarthy et al., 2019), the effect of GDP on the isolated human P2X7BD was analyzed. The addition of GDP revealed a strong stabilizing effect due to an increase in melting temperature, indicating that GDP also binds in the ballast domain of human P2X7 (Figure 4.3 A, blue).

To confirm the P2X7BD-CaM interaction that was suggested by the above-mentioned ITC studies with peptides, the nDSF experiments were also performed in the presence of Ca²⁺-CaM. Since CaM does not contain any tryptophan or tyrosine residues, the nDSF

signal exclusively originated from P2X7BD. When Ca^{2+} -CaM was added to P2X7BD, a major drop in apparent melting temperature was observed, suggesting that Ca^{2+} -CaM destabilizes P2X7BD (Figure 4.3 A, green). The scattering data of the nDSF experiments, which reflects on the aggregation status of the samples, showed that P2X7BD in the apo form as well as in complex with GDP starts to aggregate once the protein unfolds due to temperature (Figure 4.3 B, red and blue). Surprisingly, Ca^{2+} -CaM seems to prevent P2X7BD from aggregating altogether (Figure 4.3 B, green).

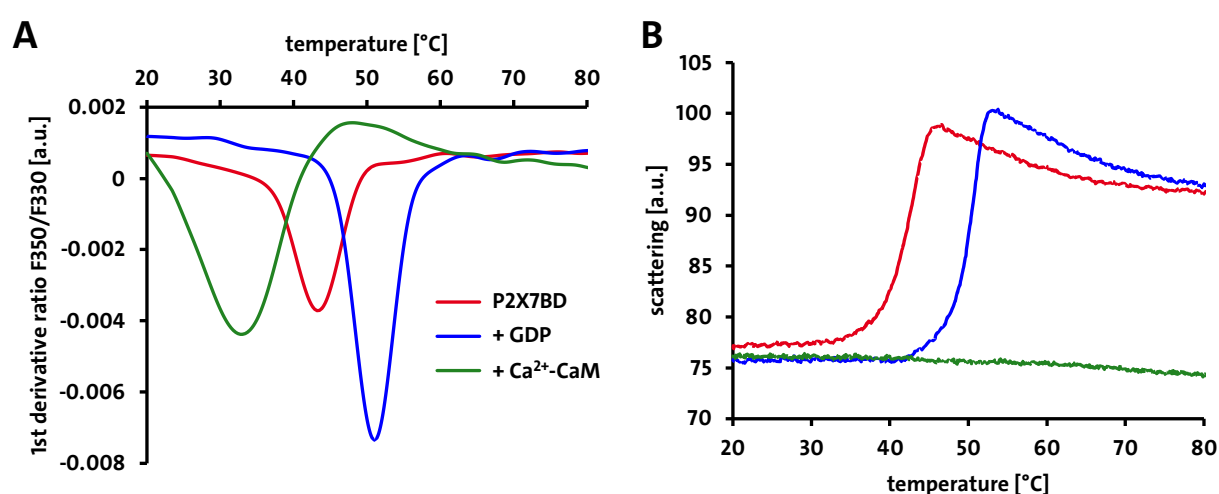


Figure 4.3: P2X7BD is stabilized by GDP and destabilized by Ca^{2+} -CaM. nDSF melting analysis of 20 μM P2X7BD with 500 μM GDP or 35 μM Ca^{2+} -CaM. **(A)** First derivative of fluorescence intensity ratio F_{350}/F_{330} with minimum at 43.3°C (melting temperature). Melting temperature increases upon addition of GDP (to 51.0°C) and decreases upon addition of Ca^{2+} -CaM (to 32.9°C). **(B)** Scattering data (visualizing aggregation status) shows that addition of GDP delays thermal aggregation, addition of Ca^{2+} prevents P2X7BD from aggregating. Same color code as in (A).

A simultaneous nDSF analysis of GDP and Ca^{2+} -CaM binding to P2X7BD revealed that the observed effects of stabilization and destabilization are concentration-dependent with similar (de)stabilization curves (Figure 4.4). Isothermal analysis with *FoldAffinity*, a software designed to deduce binding affinities from nDSF data (spc.embl-hamburg.de/app/FoldAffinity (Niebling et al., 2021)), yielded K_D values in the low micromolar range for GDP binding that seem independent from the Ca^{2+} -CaM concentration, despite large confidence intervals (Table 4.1).

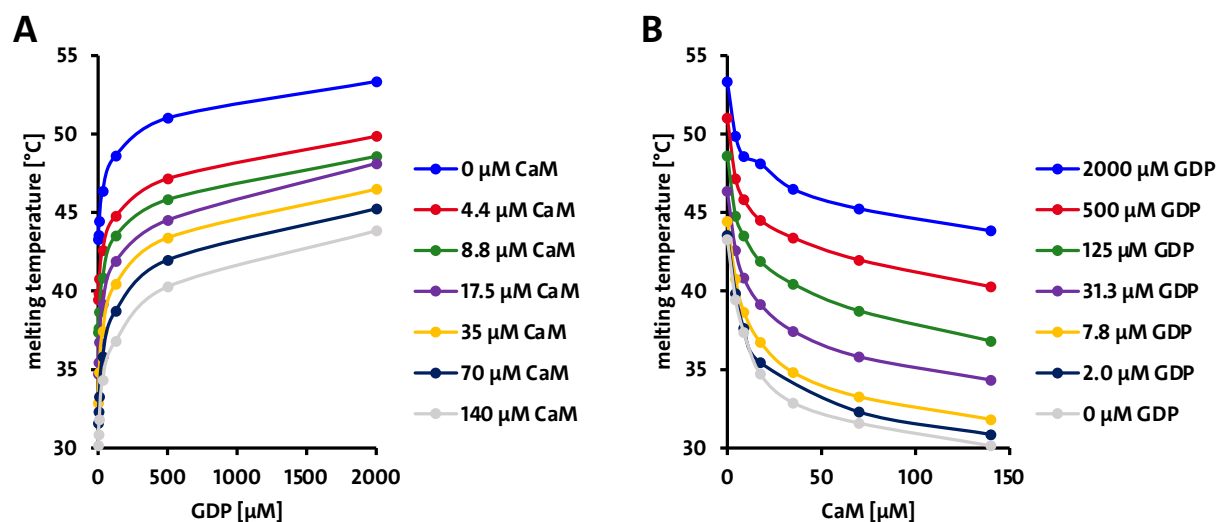


Figure 4.4: The opposite effects of GDP and Ca²⁺-CaM are concentration dependent. (A) nDSF melting analysis of 20 μM P2X7BD with varying GDP concentrations. (B) nDSF melting analysis of 20 μM P2X7BD with varying Ca²⁺-CaM (termed CaM for simplicity) concentrations.

Table 4.1: P2X7BD-GDP binding affinities at different Ca²⁺-CaM concentrations. *FoldAffinity* (spc.embl-hamburg.de/app/FoldAffinity (Niebling et al., 2021)) was used to estimate isothermal parameters (stated as confidence interval CI95%) of GDP binding to P2X7BD at different Ca²⁺-CaM concentrations. Fluorescence melting curves were fitted with the ‘local’ option and $C_p = 0$. K_D estimation ($T_{\text{isothermal}}$) was performed at 3°C above the melting temperature of P2X7BD without GDP.

Ca ²⁺ -CaM concentration	K_D CI95% [μM]	T_m without GDP	$T_{\text{isothermal}}$
0.0 μM	0.078 - 4.8	44°C	47°C
4.4 μM	0.002 - 4.7	41°C	44°C
8.8 μM	0.06 - 5.1	39°C	42°C
17.5 μM	5.0 - 7.7	36°C	39°C
70.0 μM	7.5 - 12.0	32°C	35°C
140.0 μM	5.4 - 10.0	30°C	33°C

Interestingly, the destabilizing effect on P2X7BD was only observed with Ca²⁺-CaM, not with apo-CaM (in buffer containing 10 mM EDTA). The latter showed no impact on the melting temperature of P2X7BD (Figure 4.5 A). The interaction of P2X7BD and GDP was further analyzed by ITC, confirming exothermic binding in the low micromolar range (2.6 μM ± 0.4 μM, Figure 4.5 B).

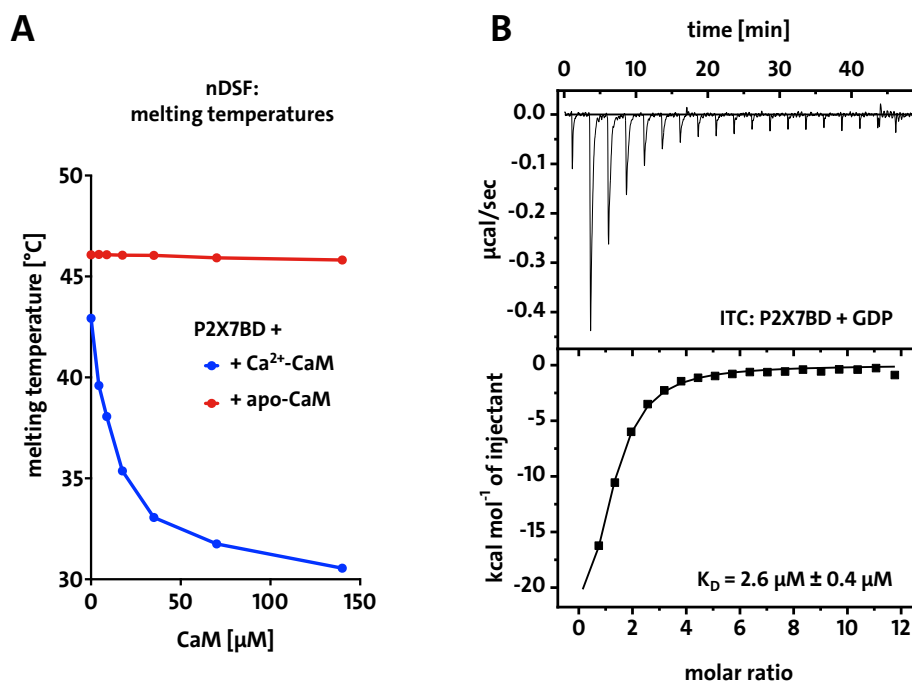


Figure 4.5: GDP and Ca²⁺-CaM interact with P2X7BD, apo-CaM does not. (A) nDSF melting temperature analysis of 20 μM P2X7BD and varying concentrations of CaM shows interaction with Ca²⁺-CaM and no interaction with apo-CaM. (B) ITC shows exothermic binding in the low micromolar range for P2X7BD (5 μM) and GDP (300 μM).

Taken together, GDP and Ca²⁺-CaM both interact with P2X7BD. GDP plays a stabilizing role while Ca²⁺-CaM destabilizes the isolated domain.

4.1.4 Ca²⁺-CaM binding disrupts the trimeric state of P2X7BD

To decipher the underlying mechanisms for the destabilizing effect, the interaction between P2X7BD and Ca²⁺-CaM was further analyzed. Chemical cross-linking of P2X7BD with disuccinimidyl suberate (DSS) and subsequent SDS-PAGE analysis revealed three bands (approx. 25 kDa, 50 kDa, 75 kDa) representing the monomeric, dimeric and trimeric domain (Figure 4.6). Addition of Ca²⁺-CaM (17 kDa) altered this pattern: Instead of the multimeric states of P2X7BD, two other bands were detected and assigned to P2X7BD-CaM complexes of the ratios 1:1 (42 kDa) and 1:2 (59 kDa, Figure 4.6). Mass spectrometric analysis of the corresponding gel bands after tryptic digest (performed at UKE core facility mass spectrometric proteomics) confirmed the presence of P2X7BD as well as of CaM (Table 4.2).

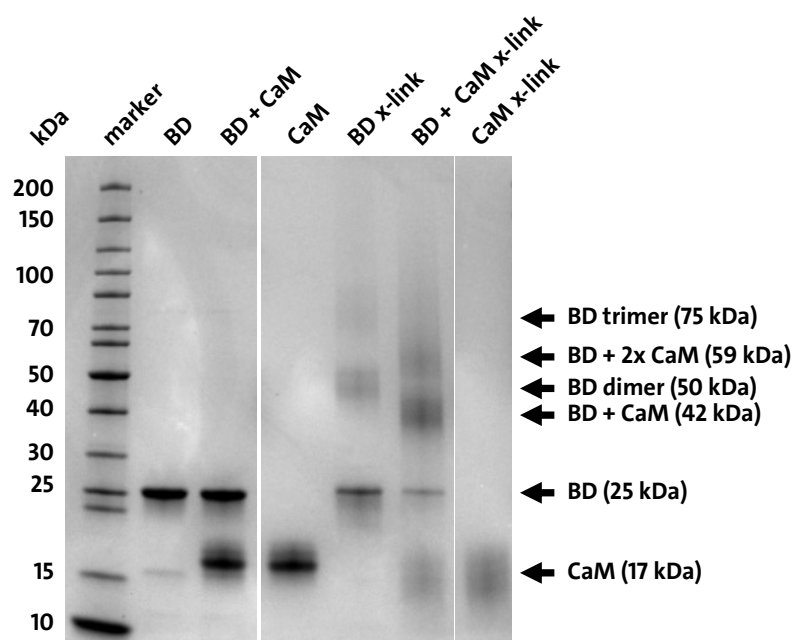


Figure 4.6: Ca²⁺-CaM cross-linking to P2X7BD. Equal amounts of P2X7BD (in figure: BD) and Ca²⁺-CaM (in figure: CaM) were mixed (50 μ M each) before chemical cross-linking (x-link) by disuccinimidyl suberate (DSS). Analysis by SDS-PAGE, Coomassie-stained. The resulting complex bands are labelled.

Table 4.2: Mass spectrometric analysis of tryptic digest of bands after cross-linking. SDS-PAGE gel bands were cut out and subjected to tryptic digest. Resulting peptides were subsequently analyzed by mass spectrometry and mapped to the sequences of the P2X7 ballast domain (P2X7BD) and calmodulin (CaM).

Band from crosslink	P2X7BD		CaM	
	# Unique peptides	Detected peptide coverage	# Unique peptides	Detected peptide coverage
42 kDa	17	74%	12	66%
59 kDa	16	74%	10	65%

As the cross-linking data suggests that binding of Ca²⁺-CaM to P2X7BD disrupts the oligomeric state of the domain, complex formation was analyzed by analytical SEC experiments. P2X7BD was mixed with excess Ca²⁺-CaM before injection onto an S200 increase column. GDP was also added in order to investigate the impact of nucleotide binding on the P2X7BD-CaM interaction. The chromatogram revealed that the P2X7BD-CaM complex exhibits a slightly reduced size compared to the domain alone because the peak shifted to a larger elution volume (Figure 4.7). Since complex formation typically results in the addition of molecular weights and subsequent increase in size, these

experiments confirmed that CaM binding to P2X7BD alters the oligomeric state of the domain. GDP did not influence the interaction.

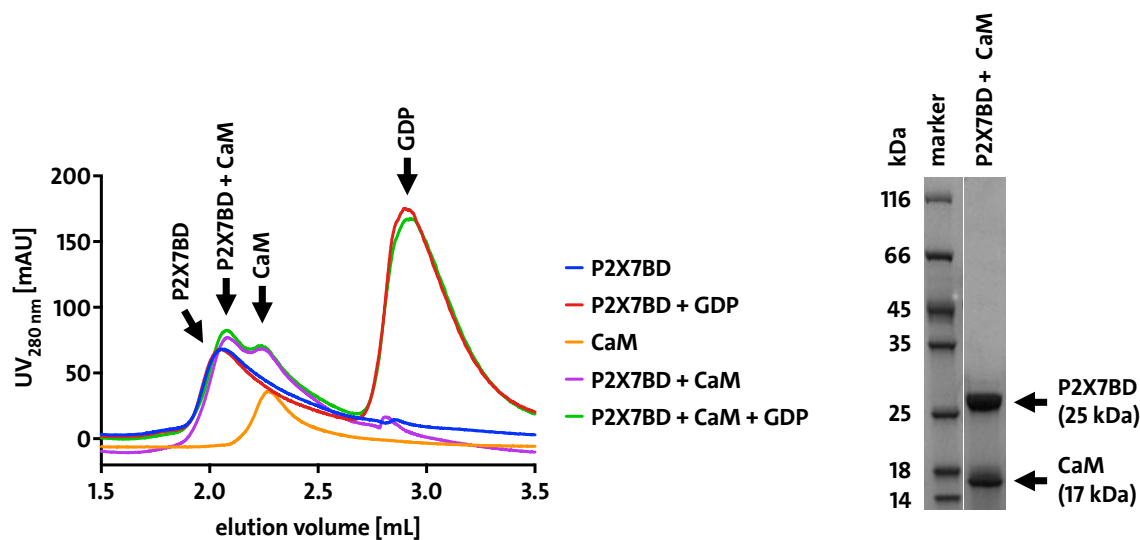


Figure 4.7: CaM binds to P2X7BD which leads to a decrease in size. Binding of CaM to P2X7BD as shown by SEC on an S200 increase 5/150 column by peak shift (P2X7BD: 2.06 mL, P2X7BD + CaM: 2.08 mL), P2X7BD (250 μ M), CaM (1250 μ M) and GDP (1250 μ M) were run in the presence of 5 mM Ca^{2+} either individually or pre-incubated together before injection. SDS-PAGE (4-20%) inset shows the peak fraction of the complex (indicated by “P2X7BD + CaM” in chromatogram) with bands for P2X7BD and CaM (Coomassie-stained).

Small-angle X-ray scattering was coupled to SEC (SEC-SAXS) to further analyze the slight change in elution volume observed in the SEC experiments. The SAXS raw data and distance distribution function curves of the P2X7BD-CaM complex show different shapes compared to P2X7BD alone (Figure 4.8). Especially, the distance distribution function reveals that the complex is more compact than the domain, however with a larger maximal protein dimension (D_{max}).

Quantitative analysis of the SAXS data showed that on the one hand, besides the D_{max} also the radius of gyration (R_g) slightly increased upon addition of Ca^{2+} -CaM. On the other hand, the Porod volume (V_{Porod}) as well as the molecular weight of the complex are reduced compared to the isolated domain. The molecular weight estimates are in agreement with a trimeric P2X7BD (theoretical: 75 kDa, SAXS: 72.4 kDa) that is disrupted upon Ca^{2+} -CaM binding and results in a complex containing one or two Ca^{2+} -CaM molecules bound to a monomeric ballast domain (theoretical: 42/59 kDa, SAXS: 50.8 kDa).

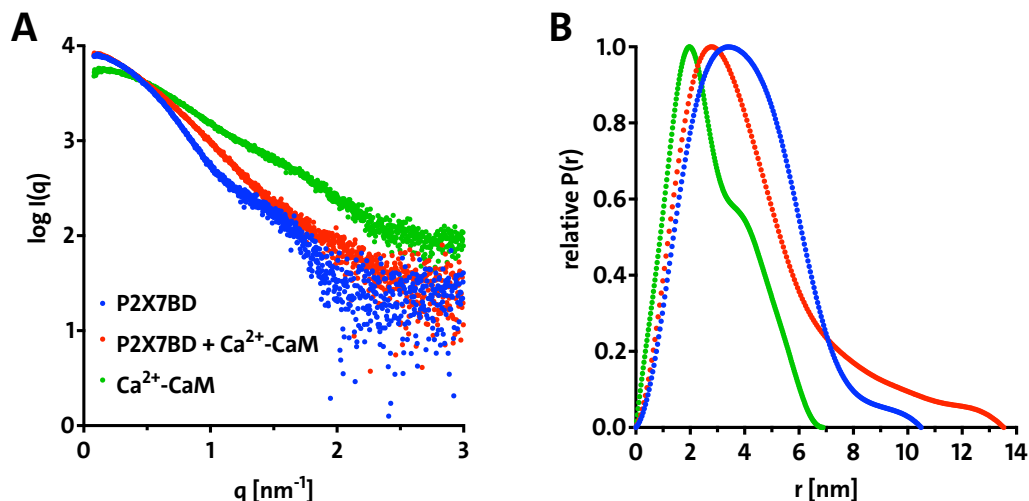


Figure 4.8: SEC-SAXS analysis of the P2X7BD-CaM interaction. (A) Size exclusion chromatography small-angle X-ray scattering (SEC-SAXS) raw data of buffer-subtracted samples. (B) Distance distribution plot as calculated from the raw data by the program GNOM. Same color code as in (A).

Table 4.3: SEC-SAXS analysis of the P2X7BD-CaM interaction. Radii of gyration (R_g), Porod volumes (V_{Porod}) and molecular weight estimates (MW) were calculated from buffer-subtracted scattering curves via the Guinier approximation. The distance distribution function ($P(r)$) which yielded the maximal protein dimension (D_{max}) was obtained from the entire scattering curve using the program GNOM.

Sample	R_g [nm]	D_{max} [nm]	V_{Porod} [Å ³]	MW [kDa]
Ca ²⁺ -CaM	2.1	6.9	22,713	15.5
P2X7BD	3.1	10.5	94,246	72.4
P2X7BD-CaM complex	3.2	13.5	72,532	50.8

Ab initio shape reconstructions based on the SAXS data using the DAMMIF software supported the previous results since the trimeric P2X7BD is converted to a more elongated form once Ca²⁺-CaM is bound (Figure 4.9).

In order to structurally confirm the findings established by SAXS, crystallization trials with the P2X7BD-CaM complex were performed by a high-throughput screening of crystallization conditions. Unfortunately, no crystal growth could be achieved in any condition. Taken together, Ca²⁺-CaM binds to the soluble P2X7 ballast domain and disrupts its trimeric state.

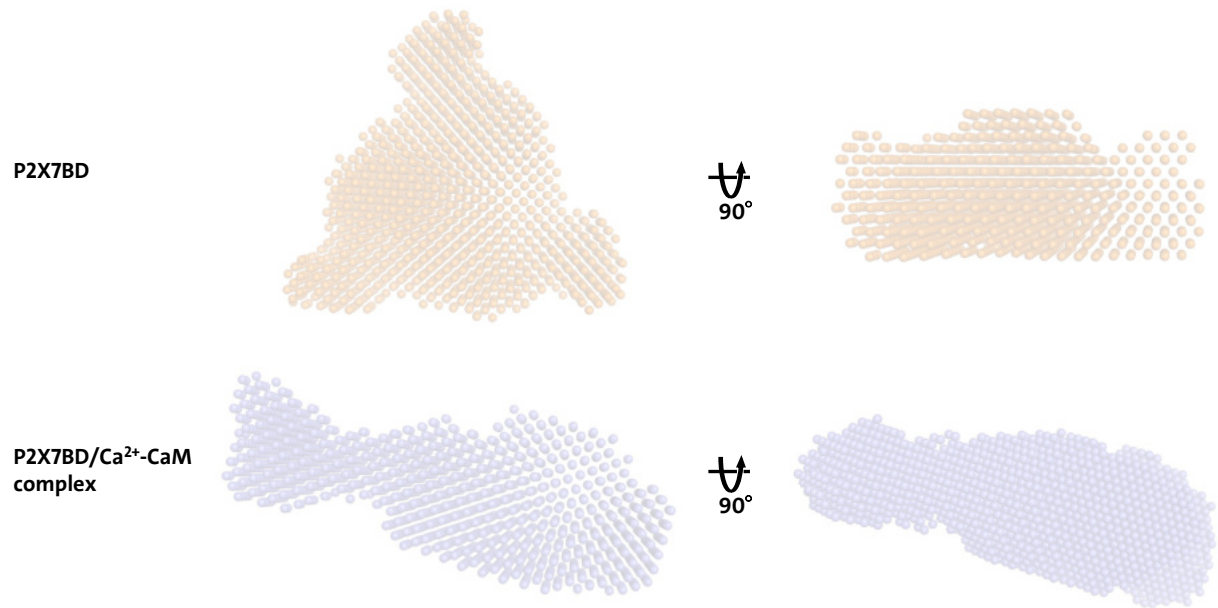


Figure 4.9: SAXS *ab initio* reconstructions of P2X7BD and P2X7BD-CaM complex. Shape reconstructions were generated using the DAMMIF software and are depicted as solid sphere dummy beads. The shape changes to a more elongated form once Ca²⁺-CaM is bound to P2X7BD.

4.2 Discussion

The P2X7 receptor, an ion channel activated by extracellular ATP, is involved in many physiological processes linked to immunity and inflammation (Adinolfi et al., 2018). It contains a unique C-terminal ballast domain (P2X7BD) that is crucial for the cytotoxic action of the receptor (Surprenant et al., 1996).

4.2.1 CaM-binding regions in the C-terminus of P2X7

Ca²⁺-CaM binding to a 1-5-16 motif within the C-terminal ballast domain of rat P2X7 (I541, L545, W556) was shown to enhance and prolong Ca²⁺ entry through the ion channel (Roger et al., 2008). Peptide-based binding experiments in this dissertation confirmed the importance of two regions for CaM binding. While the first one (named ES23, cf. Figure 4.1) comprises the known anchor residues, the other one (named SY25, cf. Figure 4.1) revealed a new putative 1-14 motif (W575, Y588). Both regions are located within the C-terminal ballast domain (Figure 4.10 A).

Interestingly, although one of the anchor residues of the published motif is not present in human and mouse P2X7 (I541 of rat P2X7 compared to T541 in human and mouse P2X7), the corresponding peptide of the mouse orthologue showed binding to Ca²⁺-CaM. In contrast to a study that could not identify any CaM-dependent processes connected to human P2X7 (Roger et al., 2010), this indicates that human as well as mouse P2X7 receptors probably interact with the Ca²⁺-sensing signaling protein. The two remaining residues of the published motif are either sufficient to bind CaM or other bulky, hydrophobic residues of the area (e.g. Y550, Y553, F558) are responsible. As shown by structural comparisons of various CaM-binding proteins, the spacing of anchor residues responsible for the interaction can vary significantly, resulting in several different CaM binding modes (Tidow and Nissen, 2013).

Both identified CaM-binding regions, including all putative anchor residues, correspond to two helical stretches within P2X7BD that are in close structural vicinity to a GDP molecule (Figure 4.10 B). This nucleotide is coordinated within a high-affinity binding site and was identified in a structural study of rat P2X7 (McCarthy et al., 2019). Its function in context of the full-length P2X7 receptor is unknown.

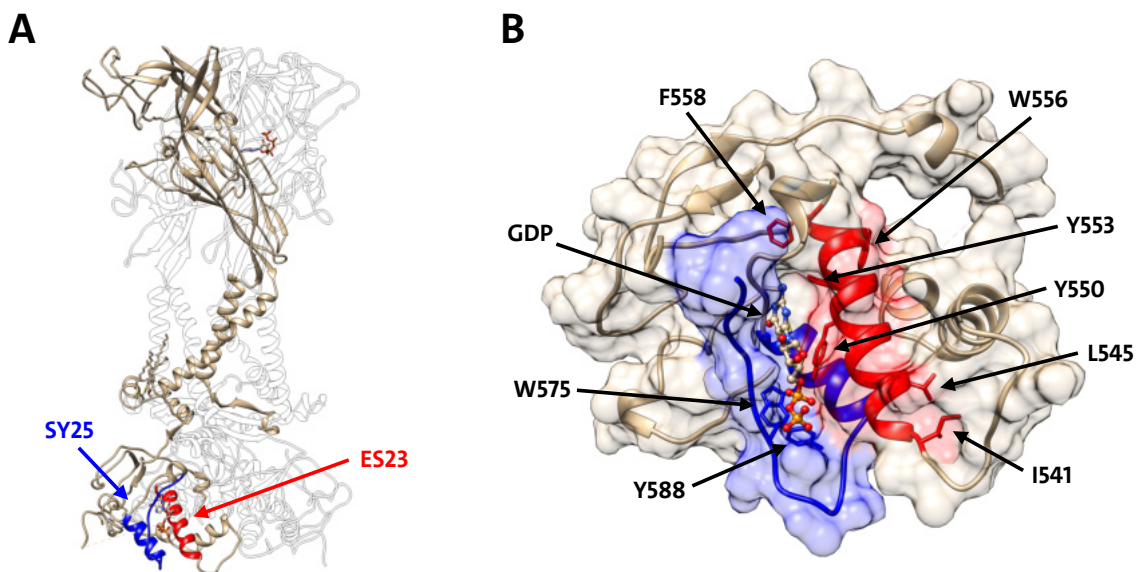


Figure 4.10: Putative CaM-binding regions of P2X7BD. Regions corresponding to published 1-5-16 motif (ES23, red) and novel motif (SY25, blue) are color coded. **(A)** Both regions are located within the C-terminal ballast domain of trimeric rat P2X7 (PDB: 6U9W (McCarthy et al., 2019)). One monomer is shown in color. **(B)** Close-up view of a P2X7BD monomer (extracted from same PDB as (A)). Both putative CaM-binding regions are in close vicinity to the bound GDP molecule (shown as ball and stick representation). Putative anchor residues responsible for CaM binding are marked. Cartoon representation with transparent surface.

Although only two of the putative anchor residues (Y550, Y588) are directly involved in nucleotide coordination, it seems likely that already slight structural rearrangements in the CaM-binding regions strongly influence GDP binding. Consequently, the P2X7BD-CaM interaction probably impairs GDP coordination, suggesting that simultaneous binding is not possible.

4.2.2 Interaction of P2X7BD with Ca^{2+} -CaM and GDP

In order to analyze the potential competition between CaM and GDP regarding P2X7BD binding, the isolated domain from human P2X7 was expressed in a soluble form. According to *AlphaFold2* models (Jumper et al., 2021; Varadi et al., 2022) of rat, mouse, and human P2X7BD, the structures of the orthologues superimpose well (Figure 4.11 A), suggesting that structural and functional results from isolated human P2X7BD can be transferred to the other orthologues as well. The loop 443-469, which is missing in the PDB structure of rat P2X7 (McCarthy et al., 2019), exhibits low confidence scores in *AlphaFold2* and is consequently probably unfolded or flexible.

The purification of human P2X7BD (in the following P2X7BD for simplicity) revealed a trimeric state (Figure 4.2), which is in good agreement with the trimeric structure of full-length rat P2X7 (McCarthy et al., 2019). Melting analysis of the protein showed only one transition, indicating that the trimer is stable and does not disassemble before the protein denatures. Large molecular interfaces between the subunits (Figure 4.11 B) could be the reason for this phenomenon and can further explain why no monomeric species was observed during the SEC purification (cf. Figure 4.2).

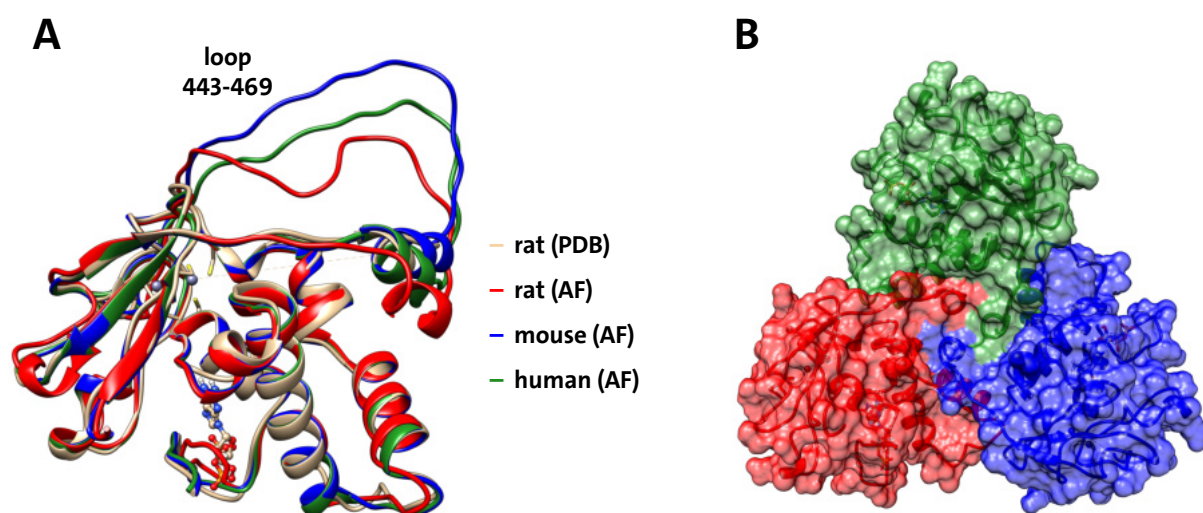


Figure 4.11: Molecular models of P2X7BD. (A) Overlay of cryo-EM structure of rat P2X7BD (wheat, extracted from PDB: 6U9W (McCarthy et al., 2019)) with *AlphaFold2* (AF) models of rat (red), mouse (blue), and human (green) P2X7BD (Jumper et al., 2021; Varadi et al., 2022). (B) Trimeric P2X7BD (extracted from same PDB as (A)) reveals large interfaces between subunits of the trimer. Monomers are differently colored. Cartoon representation with transparent surface.

In this study, GDP binding to isolated P2X7BD was confirmed by ITC and thermal stabilization. Furthermore, Ca^{2+} -CaM destabilized the domain (Figure 4.4, Figure 4.5). While stabilizing effects of ligands are common, as for example shown by ADPR binding to *drMHR1/2* (cf. Figure 3.2), destabilizing effects can be explained by ligand binding to an unfolded or intermediate state (Cimpmperman et al., 2008; Kabir et al., 2016). In the case of P2X7BD, partial unfolding could imply the partition of the purified trimer and subsequent Ca^{2+} -CaM binding to the monomeric form. SAXS (Figure 4.8) as well as cross-linking analyses (Figure 4.6) confirmed that Ca^{2+} -CaM disrupts the trimeric state of P2X7BD and that one or two Ca^{2+} -CaM molecules are bound to an individual ballast

domain. The resulting complex, which unfortunately did not crystallize, showed no aggregation upon thermal unfolding like apo-P2X7BD, indicating that Ca^{2+} -CaM binding prevents P2X7BD from aggregating. Apo-CaM did not cause thermal destabilization of P2X7BD. Thus, it presumably does not bind to the target, which is consistent with the traits of many other CaM-regulated proteins (Tidow and Nissen, 2013).

Simultaneous analysis of GDP and Ca^{2+} -CaM binding to P2X7BD showed concentration-dependent stabilization and destabilization, respectively, which appears to be independent from one another as indicated by *FoldAffinity* and SEC analysis. Reversible binding events could explain these results: Depending on relative concentrations and dissociation constants, GDP and Ca^{2+} -CaM bind to P2X7BD. While the interaction with GDP presumably does not influence the multimeric state of the domain because it revealed a stabilizing effect, Ca^{2+} -CaM binding disrupts the trimer (Figure 4.12). Although no direct experimental proof could be provided, it further seems likely that both ligands cannot bind to P2X7BD simultaneously, especially due to the structural vicinity of the two putative CaM-binding regions to the GDP binding site (cf. Figure 4.10). It remains unknown whether one of the helical structures is preferred or if both regions are in fact responsible for Ca^{2+} -CaM binding.

Taken together, isolated P2X7BD interacts reversibly with GDP and with Ca^{2+} -CaM. The latter disrupts the trimeric state of the domain. Nevertheless, functional implications for signaling and receptor gating in context of full-length P2X7 are not known.

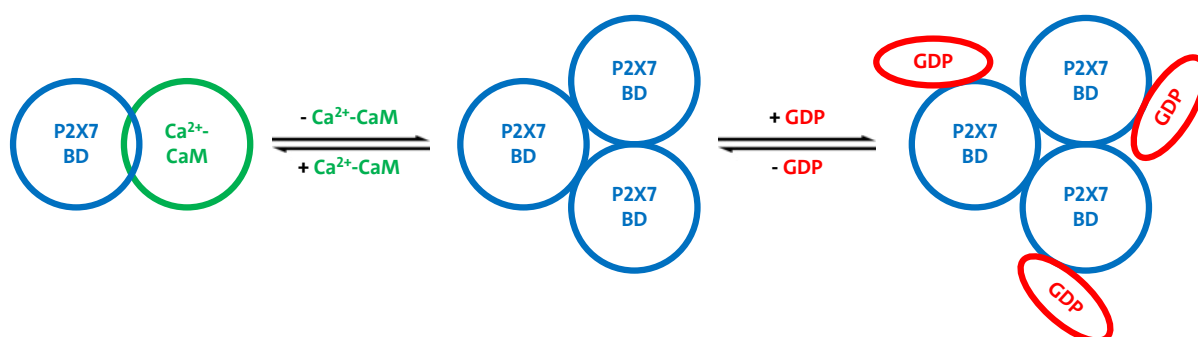


Figure 4.12: Model for ligand binding to P2X7BD. Schematic representation of GDP and Ca^{2+} -CaM binding to P2X7BD in an equilibrium dependent on relative concentrations and dissociation constants. Ca^{2+} -CaM binding to P2X7BD disrupts the trimeric form of P2X7BD.

4.3 Perspective

The results of this dissertation shed light on many characteristics regarding the C-terminal ballast domain of P2X7. However, some molecular mechanisms as well as the functional implications for signaling and receptor gating are still not fully understood and require further investigation.

While this study revealed that the P2X7BD trimer is disrupted upon binding of Ca^{2+} -CaM, the exact nature of this interaction is not known. More insight into the regulatory function of the Ca^{2+} -sensing signaling protein could be achieved by means of a structure of the P2X7BD-CaM complex. This work would presumably indicate which CaM-binding region is responsible for the interaction and if CaM and GDP can bind to P2X7BD simultaneously or if the binding events are mutually exclusive.

Structural experiments with full-length P2X7 and Ca^{2+} -CaM could further answer the question if CaM binding also influences the intact receptor. Based on this dissertation, it seems likely that trimer disruption of the ballast domain induces movements of the cytoplasmic cap region that lead to conformational changes which alter functional properties of full-length P2X7.

Although the ballast domain is not directly involved in channel gating, it is important for some functional properties of P2X7 such as membrane permeabilization and the cytotoxic effect (Adinolfi et al., 2010; Cheewatrakoolpong et al., 2005; Surprenant et al., 1996; Wilson et al., 2002). Therefore, the C-terminal domain probably links channel function with intracellular signaling cascades. Further functional studies are needed to understand this connection and the roles of the interaction partners Ca^{2+} -CaM, GDP, and also of the Zn^{2+} -binding site, that was identified within the ballast domain (McCarthy et al., 2019).

5 MATERIAL AND METHODS

5.1 Material

5.1.1 Chemicals

Unless otherwise stated, all reagents and chemicals were purchased from Sarstedt, Carl Roth, Sigma-Aldrich, Thermo Fisher Scientific. ADPR analogues were purchased from Biolog Life Science Institute. Hazardous and toxic chemicals were handled and disposed according to the safety instructions (see: 7 Safety and disposal) and are listed in Table 7.1.

5.1.2 Bacteria and cell lines

All bacterial strains as well as insect and mammalian cell lines used for cloning or the expression of recombinant protein sequences in this thesis are shown in Table 5.1 alongside their origins and culture media. Detailed compositions of culture media are listed in Table 5.2.

Table 5.1: Expression systems used in this study.

Cells	Origin	Culture Medium
B834 (DE3)	<i>E. coli</i>	M9 minimal medium
BL21 Gold (DE3)	<i>E. coli</i>	LB-Lennox or TB
BL21 Gold pLysS (DE3)	<i>E. coli</i>	TB
C43 (DE3)	<i>E. coli</i>	TB
DH10Bac TM	<i>E. coli</i>	LB-Lennox
Rosetta 2 (DE3)	<i>E. coli</i>	TB
Rosetta-gami (DE3)	<i>E. coli</i>	TB
XL1-Blue	<i>E. coli</i>	LB-Lennox
Sf9 insect cells	<i>Spodoptera frugiperda</i>	Insect-XPRESS
HEK293 wt	<i>Homo sapiens</i> , kidney	DMEM
HEK293S GnTI- adherent	<i>Homo sapiens</i> , kidney	DMEM/F-12
HEK293S GnTI- in suspension	<i>Homo sapiens</i> , kidney	FreeStyle TM 293

5.1.3 Solutions and culture media

All solutions and cell culture media that were utilized during the study are shown in Table 5.2 alongside their composition. They were prepared with de-ionized water. The pH values were measured and adjusted using a peqMeter 1.14 (PEQLAB).

Table 5.2: Composition of solutions and culture media.

Description	Composition
DMEM (Dulbecco's Modified Eagle's Medium) medium	ready-to-use (Thermo Fisher 10566016), add 10% (v/v) FBS (Sigma), add 100 U/mL Penicillin (Gibco), add 100 µg/mL Streptomycin (Gibco)
DMEM/F-12 (Dulbecco's Modified Eagle's Medium/Nutrient Mixture F-12) medium	ready-to-use (Thermo Fisher 11320033), add 10% (v/v) FBS (Sigma), add 100 U/mL Penicillin (Gibco), add 100 µg/mL Streptomycin (Gibco)
FreeStyle™ 293 expression medium	ready-to-use (Thermo Fisher 12338018), add 1% (v/v) FBS (Sigma)
Insect-XPRESS medium	ready-to-use (Biozym 881172)
M9 minimal medium	6 g/L Na ₂ HPO ₄ , 4 g/L KH ₂ PO ₄ · 3 H ₂ O, 0.5 g/L NaCl, 0.5 g/L NH ₄ Cl, 0.25 g/L MgSO ₄ · 7 H ₂ O, 44.1 mg/L CaCl ₂ · 2 H ₂ O, 0.4% (w/v) Glucose, 5 mg/L EDTA pH 7.5, 0.833 mg/L FeCl ₃ , 0.084 mg/L ZnCl ₂ , 0.013 mg/L CuCl ₂ · 2 H ₂ O, 0.060 mg/L CoCl ₂ · 6 H ₂ O, 0.010 mg/L H ₃ BO ₃ , 0.240 mg/L CuSO ₄ · 1 H ₂ O, 0.300 mg/L MnCl ₂ · 4 H ₂ O, 0.027 mg/L ZnSO ₄ · 1 H ₂ O, 0.5 mg/L riboflavin, 0.5 mg/L niacinamide, 0.5 mg/L pyridoxine monohydrate, 0.5 mg/L thiamine, 24 mg/L of all amino acids except methionine
LB (Lysogeny Broth) Lennox medium	20 g/L LB-Lennox medium (Roth X964.4), add 15 g/L Agar-Agar for LB-Agar plates

Description	Composition
Patch clamp extracellular solution 1x	140 mM NMDG, 5 mM KCl, 3.3 mM MgCl ₂ , 1 mM CaCl ₂ , 5 mM D-Glucose, 10 mM HEPES, adjust to pH 7.4 with HCl
Patch clamp intracellular solution 2x	120 mM KCl, 8 mM NaCl, 1 mM MgCl ₂ , 10 mM HEPES, 10 mM EGTA, 5.6 mM CaCl ₂ , adjust to pH 7.2 with KOH
PBS (Phosphate-buffered saline)	ready-to-use (Thermo Fisher 14190144)
SDS sample buffer 1x	1% (w/v) SDS, 8% (v/v) Glycerol, 50 mM Tris pH 7, 1% (v/v) 2-Mercaptoethanol, 0.01% (w/v) Bromophenol blue
SDS-PAGE running buffer 1x	25 mM Tris base (3 g/L), 192 mM Glycine (14.4 g/L), 0.1% (w/v) SDS
TAE buffer 1x	40 mM Tris base, 20 mM Acetic acid (1.21 mL/L), 1 mM EDTA pH 8
TB (Terrific Broth) medium	47.6 g/L Terrific Broth modified (Roth HP61.1), 4 mL/L Glycerol
TBST buffer 1x	50 mM Tris base (6 g/L), 138 mM NaCl (8 g/L), 2.7 mM KCl (0.2 g/L), adjust to pH 8.0 with HCl, add 0.05% (v/v) Tween-20
Western blot transfer buffer 1x	25 mM Tris base (3 g/L), 192 mM Glycine (14.4 g/L), 0.025% (w/v) SDS, 20% (v/v) Methanol

5.1.4 Plasmid vectors

Table 5.3 shows all plasmid vectors that were used in this study with their composition. All vector backbones originated from the Tidow lab except pIRES2-EGFP which was supplied by the Fliegert lab (UKE, Hamburg), pEG BacMam which was supplied by Eric

Gouaux (Vollum Institute, Oregon, USA), and pGEX6P1-GFP-nanobody which was supplied by Kazuhisa Nakayama (Kyoto University, Japan) through Addgene (#61838). TRPM2 sequences originated either from the Fliegert lab (*hsTRPM2*) or GenScript (*drTRPM2*, #ODa47363D). P2X7 sequences were supplied by Annette Nicke (LMU Munich). The inserts were added to the backbones and mutated during this work.

Table 5.3: Plasmid vectors used in this study.

Insert	Tags	Backbone
<i>drMHR1/2</i> (1-419 of <i>drTRPM2</i>)	TEV-cleavable N-terminal His ₆	pnEK-vH
<i>drMHR1/2</i> C65A	TEV-cl. N-term. His ₆	pnEK-vH
<i>drMHR1/2</i> C67A	TEV-cl. N-term. His ₆	pnEK-vH
<i>drMHR1/2</i> C65A C67A	TEV-cl. N-term. His ₆	pnEK-vH
<i>hsMHR1/2</i> (1-443 of <i>hsTRPM2</i>)	TEV-cl. N-term. His ₆	pnEK-vH
<i>hsMHR1/2</i> (1-443 of <i>hsTRPM2</i>)	TEV-cl. N-term. Lipo-His ₆	pRSET
<i>hsMHR1/2</i> (1-443 of <i>hsTRPM2</i>)	TEV-cl. N-term. GST-His ₆	pET42a(+)
<i>drNUDT9-H</i> (1188-1474 of <i>drTRPM2</i>)	TEV-cl. N-term. His ₆	pnEK-vH
<i>drTRPM2</i>	-	pIRES2-EGFP
<i>hsTRPM2</i>	-	pIRES2-EGFP
<i>hsTRPM2</i> C89A	-	pIRES2-EGFP
<i>hsTRPM2</i> C91A	-	pIRES2-EGFP
<i>hsTRPM2</i> C89A C91A	-	pIRES2-EGFP
<i>hsTRPM2</i>	C-term. His ₆ -EGFP	pEG BacMam
<i>hsTRPM2</i>	C-term. His ₆ -MBP	pEG BacMam
<i>hsP2X7BD</i> (395-595 of <i>hsP2X7</i>)	TEV-cl. C-term. mCherry-His ₆	pET mCherry
cap- <i>hsP2X7BD</i> (355-595 of <i>hsP2X7</i>)	TEV-cl. N-term. His ₆	pnEK-vH
Calmodulin	-	pET15b
anti-GFP nanobody	GST	pGEX6P1

5.2 Methods

5.2.1 Microbiology

5.2.1.1 Preparation and transformation of electrocompetent *E. coli* cells

To prepare electrocompetent *E. coli* cells a single-clone culture (1 L) was grown with the appropriate antibiotics at 37°C while shaking until a cell density (OD₆₀₀) between 0.4 and 0.6 was reached. Cells were cooled on ice for 60 min before four centrifugation (4,000×g for 15 min) and resuspension steps with decreasing resuspension volumes (800 mL H₂O, 500 mL H₂O, 20 mL 10% (v/v) glycerol, 3 mL 10% (v/v) glycerol). After the last resuspension step the cells were divided into 50 µL aliquots, flash frozen in liquid nitrogen and stored at -80°C.

Cells were thawed and transformation of plasmid DNA (50-100 ng per cell aliquot) was performed with an electroporation device (MicroPulser, BioRad). After the electroshock 300 µL of LB medium were added to the transformed cells and they were grown for 60 min at 37°C while shaking. 50-200 µL were plated on LB-agar plates containing the appropriate antibiotics.

5.2.1.2 Preparation and transformation of chemically competent *E. coli* cells

To prepare chemically competent DH10Bac™ *E. coli* cells a single-clone culture (400 mL) was grown with the appropriate antibiotics at 37°C while shaking until a cell density (OD₆₀₀) between 0.4 and 0.6 was reached. Cells were cooled on ice for 60 min before two centrifugation (2,500×g for 10 min) and resuspension steps with decreasing resuspension volumes (40 mL 0.1 M CaCl₂, 8 mL 0.1 M CaCl₂/10% (v/v) glycerol). After the second resuspension step the cells were divided into 100 µL aliquots, flash frozen in liquid nitrogen and stored at -80°C.

The cells were thawed on ice for transformation. Plasmid DNA (0.1-1.0 µg per cell aliquot) was added to the cells and they were incubated on ice for 30 min before subjected to a heat shock (42°C for 45 s). After incubation on ice for 2 min 900 µL LB medium were added to the transformed cells and they were grown for 4 h at 37°C while shaking. 100-300 µL were plated on LB-agar plates containing the appropriate antibiotics.

5.2.2 Molecular biology

5.2.2.1 Polymerase chain reaction (PCR)

DNA sequences of interest were amplified by PCR before being inserted into expression vectors. The general PCR reaction set-up is shown in Table 5.4. The primers for the PCR reaction (Sigma) were designed with 16-22 nucleotides matching to the template sequence and overhangs corresponding to the desired restriction enzyme sequences.

Table 5.4: General PCR reaction set-up.

Compound	Amount	Concentration
Template DNA	0.1-1.0 ng	4-40 pg/ μ L
5x Phusion buffer HF or GC	5.0 μ L	1x
dNTPs (10 mM each stock)	0.5 μ L	200 μ M each
Forward primer (10 μ M stock)	0.5 μ L	0.2 μ M
Reverse primer (10 μ M stock)	0.5 μ L	0.2 μ M
Phusion polymerase (2 U/ μ L, Thermo Fisher F530)	0.25 μ L	0.02 U/ μ L
H ₂ O	to 25 μ L	

PCR reactions were performed with a peqSTAR 2X thermal cycler (peqlab). The general PCR program is shown in Table 5.5.

Table 5.5: General PCR program.

Step	Temperature	Time	Cycles
Initial denaturation	98°C	3 min	
Denaturation	98°C	30 s	30x
Annealing	56°C	30 s	
Extension	72°C	30 s / kb	
Final Extension	72°C	5 min	
Store	6°C	Hold	

PCR products were purified with the GeneJET gel extraction kit (Thermo Fisher K0691). The binding buffer of the kit (75 μL) was directly added to the PCR reaction. After loading to the spin column and washing according to the manufacturer's protocol the purified PCR product was eluted with 25 μL H_2O .

5.2.2.2 Cloning with restriction enzymes

DNA sequences of interest (as purified PCR products (see 5.2.2.1) or within plasmid vectors) were cloned into the desired expression vectors with two appropriate FastDigest restriction enzymes (Thermo Fisher). Initially, the sequences were digested for one hour at 37°C as shown in Table 5.6. In the same step, the target vector was dephosphorylated (FastAP® Alkaline Phosphatase, Thermo Fisher).

Table 5.6: General DNA digest reaction.

Compound	Vector	Insert
DNA	5 μg plasmid DNA	20.5 μL purified PCR product or 5 μg plasmid DNA
10x FastDigest buffer green	2.5 μL	2.5 μL
FastDigest restriction enzyme #1	1.0 μL	1.0 μL
FastDigest restriction enzyme #2	1.0 μL	1.0 μL
FastAP® Alkaline Phosphatase	1.0 μL	-
H_2O	to 25 μL	to 25 μL

The digested DNA fragments were visualized by agarose gel electrophoresis (1% agarose in TAE buffer, stained with ROTI®GelStain Red, Roth) and subsequently purified from the gel with the GeneJET gel extraction kit (Thermo Fisher K0691) according to the manufacturer's protocol. Elution was performed with 25 μL H_2O .

The digested and purified DNA fragments were ligated with T4 Ligase (Thermo Fisher EL0011) for one hour at room temperature. The ligation reaction set-up is shown in Table 5.7.

Table 5.7: General ligation reaction set-up.

Compound	Amount
Vector	100 ng
Insert	3:1 (insert : vector) molar ratio
10x T4 Ligase buffer	2.0 μ L
T4 Ligase	0.5 μ L
H ₂ O	to 20 μ L

The ligated DNA construct (5 μ L) was transformed into electrocompetent XL1-Blue *E. coli* bacteria (see 5.2.1.1). After shaking for one hour at 37°C to produce antibiotic resistance proteins the bacteria were plated out on LB-agar plates containing the appropriate antibiotics. The plates were incubated at 37°C over night. Colonies were picked into 4 mL LB medium the next day and grown shaking at 37°C over night.

Plasmid DNA was purified from the cultures using the GeneJET Plasmid Miniprep Kit (Thermo Fisher K0502) according to the manufacturer's protocol. Elution was performed with 40 μ L H₂O. The desired sequences were verified via Sanger sequencing (sent to Eurofins Genomics) with the appropriate sequencing primers.

5.2.2.3 Site-directed mutagenesis

Site-directed mutagenesis was performed to introduce mutations into DNA sequences. For small mutations primers (Sigma) were designed with the Takara Bio primer design online tool (www.takarabio.com/learning-centers/cloning/primer-design-and-other-tools). For large insertions or deletions phosphorylated, non-overlapping primers (Sigma) with 24-30 matching nucleotides were designed. Mutagenesis PCR was performed with PlatinumTM SuperFi II DNA Polymerase (Thermo Fisher 12368010) according to the manufacturer's protocol. The general mutagenesis PCR reaction set-up is shown in Table 5.8.

Table 5.8: General mutagenesis PCR reaction set-up.

Compound	Amount	Concentration
Template DNA	0.1-1.0 ng	2-20 pg/ μ L
2x Superfi II PCR Master Mix	25 μ L	1x
Forward primer (10 μ M stock)	2.5 μ L	0.5 μ M
Reverse primer (10 μ M stock)	2.5 μ L	0.5 μ M
H ₂ O	to 50 μ L	

PCR reactions were performed with a peqSTAR 2X thermal cycler (peqlab). The general mutagenesis PCR program is shown in Table 5.9.

Table 5.9: General mutagenesis PCR program.

Step	Temperature	Time	Cycles
Initial denaturation	98°C	30 s	
Denaturation	98°C	10 s	30x
Annealing	60°C	10 s	
Extension	72°C	30 s / kb	
Final Extension	72°C	5 min	
Store	6°C	Hold	

FastDigest DpnI (2 μ L, Thermo Fisher FD1704) was added directly to the reaction to digest the non-mutated template DNA (1 h at 37°C). Afterwards, the PCR product was purified with the GeneJET gel extraction kit (Thermo Fisher K0691). The binding buffer of the kit (150 μ L) was directly added to the DpnI-digested PCR reaction. After loading to the spin column and washing according to the manufacturer's protocol the purified PCR product was eluted with 25 μ L H₂O.

Only for large insertions or deletions an additional ligation reaction (set-up: Table 5.10) was performed for one hour at room temperature.

Table 5.10: General mutagenesis ligation reaction set-up.

Compound	Amount
Purified mutagenesis PCR product	25 μ L
10x T4 Ligase buffer	5 μ L
T4 Ligase	1 μ L
H ₂ O	to 50 μ L

Subsequently, 5 μ L of the purified PCR product (for small mutations) or of the ligation reaction (for large insertions or deletions) were transformed as mentioned above (see 5.2.2.2). The analysis including mini prep and sequence verification via Sanger sequencing was performed accordingly.

5.2.3 Protein expression and purification

5.2.3.1 Zebrafish MHR1/2 domain (*drMHR1/2*) of TRPM2

The expression and purification of *drMHR1/2* of TRPM2 is published (Sander et al., 2022a) and was conceptualized as well as performed by the author of this thesis. The sequence coding for the *drMHR1/2* domain (residues 1-419 of *drTRPM2*) was cloned (see 5.2.2.1 and 5.2.2.2) into a pNEK-vH vector bearing a TEV-cleavable N-terminal His₆-tag. For wild type protein, the plasmid was transformed into *E. coli* BL21 Gold (DE3) cells (see 5.2.1.1) protein production was carried out in TB media supplemented with 25 μ g/mL kanamycin. Cells were grown at 37°C until a cell density (OD₆₀₀) of 1 was reached. After induction with 0.1 mM isopropyl β -D-1-thiogalactopyranoside (IPTG), the cells were grown for further 16 hours at 20°C. The production of selenomethionine-labelled protein was carried out in the methionine auxotroph *E. coli* strain B834 (Wood, 1966) in M9 minimal medium supplemented with 70 mg/L L-selenomethionine (Serva 77765) and 25 μ g/mL kanamycin. Cells were grown at 37°C to an OD₆₀₀ of 0.6 and after induction with 0.1 mM IPTG, the target protein was expressed for further 16 hours at 20 °C.

The cells were harvested by centrifugation (5,000 \times g for 25 min) and lysed in 25 mM Tris pH 7.5, 300 mM NaCl, 5% (v/v) glycerol, 5 mM 2-mercaptoethanol (100 mL buffer per liter of growth culture) using a high-pressure homogenizer (EmulsiFlex-C3, Avestin). 2 μ g/mL

DNase I with 2 mM MgCl₂ and 0.2 mg/mL lysozyme were added to facilitate lysis. 0.5 mM phenylmethylsulfonyl fluoride (PMSF) was added to inhibit protease activity. Cell debris was removed by centrifugation (39,000×g for 45 min) and the His₆-tagged protein was purified from the supernatant using immobilized metal affinity chromatography (IMAC) with Ni-NTA resin (Roth) in a gravity flow column. 2 mL bead volume was used for the lysate of 1 L growth culture. Loading to the beads was performed in presence of 5 mM imidazole, 30 mM imidazole was used for washing and 400 mM imidazole was used for the elution of the target protein. After His-tag removal by TEV protease (1/10 w/w, self-made in the Tidow lab) over night and reverse Ni-NTA purification, the target protein was further purified by gel filtration on a Superdex S200 increase 10/300 column (Cytiva) using buffer M (for wild type protein, 25 mM HEPES pH 7.5, 150 mM NaCl, 5 mM CaCl₂, 5 mM MgCl₂) or buffer MS (for Se-Met-labelled protein, 25 mM HEPES pH 7.5, 150 mM NaCl, 5 mM CaCl₂, 5 mM MgCl₂, 5 mM 2-mercaptoethanol). Peak fractions were pooled and protein identity confirmed by SDS-PAGE and mass spectrometry (see 5.2.4.1 and 5.2.4.1).

5.2.3.2 Human MHR1/2 domain (*hsMHR1/2*) of TRPM2

The sequence coding for the *hsMHR1/2* domain (residues 1-443 of *hsTRPM2*) was cloned (see 5.2.2.1 and 5.2.2.2) into three different expression vectors: a pNEK-vH vector bearing a TEV-cleavable N-terminal His₆-tag, a pRSET vector bearing a TEV-cleavable N-terminal Lipo-His₆-tag and a pET42a vector bearing a TEV-cleavable N-terminal GST-His₆-tag. Expression tests were performed with the following *E. coli* strains: BL21 Gold (DE3), BL21 Gold pLysS (DE3), C43 (DE3), Rosetta 2 (DE3), Rosetta-gami (DE3). Appropriate antibiotics were used depending on the strain. Cultures were grown until a density of 0.6 (measured at 600 nm) was reached, induced with 0.1 mM IPTG and further grown at 20°C for 16 hours.

Cells were harvested by centrifugation (5,000×g for 15 min) and lysed in 25 mM Tris pH 8, 500 mM NaCl, 10% (v/v) glycerol, 5 mM 2-mercaptoethanol (10 mL buffer per 100 mL of growth culture) using pulsed sonication for 3x 3 min (30% power, Bandelin Sonopuls GM2070). 2 µg/mL DNase I with 2 mM MgCl₂ and 0.2 mg/mL lysozyme were added to

facilitate lysis alongside 0.5 mM PMSF to inhibit protease activity. Cell debris was removed by centrifugation (21,000×g for 60 min) and the supernatant was subjected to IMAC with Ni-NTA resin (Roth) in a gravity flow column. 0.3 mL bead volume was used for the lysate of 100 mL growth culture. Loading to the beads was performed in presence of 5 mM imidazole, 30 mM imidazole was used for washing and 500 mM imidazole was used for the elution.

5.2.3.3 Calmodulin (CaM)

The expression and purification of CaM is prepared for publication (Sander et al., 2022b), was conceptualized by Katharina Veith and performed by the author of this thesis. The sequence coding for human CaM was cloned into a pET15b vector (see 5.2.2.1 and 5.2.2.2) without additional tags. Protein expression was carried out in BL21 Gold (DE3) *E. coli* (see 5.2.1.1) in LB medium supplemented with 100 µg/mL ampicillin. Cells were induced (0.1 mM IPTG) at a density of 0.6 (measured at 600 nm) and further grown at 20°C for 16 hours.

Cells were harvested by centrifugation (5,000×g for 25 min) and resuspended in 50 mM Tris pH 7.5, 2 mM CaCl₂ (30 mL buffer per liter of growth culture). 2 µg/mL DNase I with 2 mM MgCl₂ and 0.2 mg/mL lysozyme were added to facilitate lysis which was achieved by pulsed sonication for 3x 3 min (30% power, Bandelin Sonopuls GM2070). Cell debris was removed by centrifugation (39,000×g for 45 min) and the cleared lysate was subjected to hydrophobic interactionTM chromatography (HIC) on a HiTrapTM Phenyl FF (LS) column (5 mL bead volume, Cytiva) connected to an ÄKTA start (Cytiva). The following buffers were used: lysis and loading: 50 mM Tris pH 7.5, 2 mM CaCl₂; elution: 50 mM Tris pH 7.5, 10 mM EDTA. Loading and elution processes were repeated until the eluted protein concentration decreased. The eluted fractions were pooled and gel filtrated on a Superdex S75 10/300 column (Cytiva) in 20 mM HEPES pH 7.5, 150 mM NaCl, 5 mM CaCl₂ to obtain the active Ca²⁺-CaM or in 20 mM HEPES pH 7.5, 150 mM NaCl, 10 mM EDTA to obtain apo-CaM. Peak fractions were pooled and protein identity was confirmed by SDS-PAGE and mass spectrometry (see 5.2.4.1 and 5.2.4.1).

5.2.3.4 Anti-GFP nanobody

The sequence coding for a GST-tagged anti-GFP nanobody was cloned into a pGEX6P1 plasmid (see 5.2.2.2). Protein expression was carried out in electrocompetent BL21 Gold *E. coli* (see 5.2.1.1) in LB medium supplemented with 100 µg/mL ampicillin. Cells were grown until a density of 0.5 (measured at 600 nm) was reached, induced with 0.1 mM IPTG and further grown at 30°C for 4 hours.

The cells were harvested by centrifugation (5,000×g for 25 min) and resuspended in 25 mM Tris pH 7.5, 150 mM NaCl, 5 mM DTT, 1 mM PMSF (10 mL buffer per 250 mL of growth culture). Lysis was achieved by pulsed sonication for 3x 1 min (30% power, Bandelin Sonopuls GM2070) and the addition of Triton X-100 (final 1% v/v). Cell debris was removed by centrifugation (21,000×g for 30 min) and the cleared lysate was added to glutathione-sepharose 4B beads (Macherey-Nagel 745500, 2 mL lysate per mL bead volume) before incubation at 4°C for 18 h. The beads were washed with 40 column volumes of 25 mM Tris pH 7.5, 150 mM NaCl, 5 mM DTT, 0.1% Triton X-100 and subsequently used for purification of GFP-tagged *hsTRPM2* (see 5.2.3.5).

5.2.3.5 Full-length human TRPM2 (*hsTRPM2*)

The sequence coding for *hsTRPM2* was cloned (see 5.2.2.1 and 5.2.2.2) into the pEG BacMam vector (supplied by Eric Gouaux, Vollum Institute, Oregon, USA) with a C-terminal His₆-EGFP or His₆-MBP tag. The pEG BacMam vector allows for expression in mammalian cells due to a CMV promoter in front of the gene of interest. Since the vector also contains an EGFP sequence behind an insect P10 promoter and baculovirus traits it can be further used to produce BacMam virus in insect cells.

Test expressions: Test expressions were performed in adherent HEK293S GnTI- cells grown in DMEM/F-12 medium at 37°C and 5% CO₂. After transient transfection with Lipofectamine LTX according to the manufacturer's protocol (1.5 µg DNA, 4.5 µL Lipofectamine LTX in one well of a 6 well plate), the cells were grown for 18 hours before the medium was changed and 10 mM sodium butyrate was added to boost protein expression. The cells were grown for further 24 hours at 30°C before being harvested by centrifugation (1,500×g for 5 min) and subsequently washed with PBS. After whole-cell

solubilization with 20 mM Tris pH 8, 150 mM NaCl, 40 mM (2%) Dodecyl- β -D-maltopyranoside (DDM, Glycon Biochemicals, Luckenwalde, Germany) for one hour, insoluble material was separated by centrifugation (70,000 \times g for 40 min). The lysates were analyzed by SDS-PAGE (see 5.2.4.1) and subsequent western blot (see 5.2.4.2) to visualize TRPM2 expression.

BacMam expression: For large-scale BacMam expression a BacMam plasmid was transformed into chemically competent DH10BacTM *E. coli* (see 5.2.1.2) and plated on LB-agar plates containing 50 μ g/mL kanamycin, 7 μ g/mL gentamicin, 10 μ g/mL tetracycline, 100 μ g/mL X-gal, 40 μ g/mL IPTG. After 48 h at 37°C, a white colony was picked, cultured and subjected to bacmid isolation with the GeneJET Plasmid Miniprep Kit (Thermo Fisher K0502) according to the manufacturer's protocol. Bacmid DNA was eluted with 50 μ L ddH₂O and subsequently used for transfection of adherent Sf9 insect cells using Cellfectin II reagent (Thermo Fisher 10362-100) according to the manufacturer's instructions (1 μ g bacmid DNA, 8 μ L Cellfectin II reagent per well of a six-well plate with 9×10^5 cells). Adherent Sf9 cells were grown in Insect-XPRESS medium (Biozym 881172) at 27°C. The culture medium containing BacMam P1 virus was collected and filtered (45 μ m) after four days and used to infect suspension cultures of Sf9 cells (1:500 v/v at a cell density of 1×10^6 cells/mL) to generate BacMam P2 virus. Sf9 suspension cultures were grown at 27°C and 130 rpm. The culture medium containing P2 virus was collected (5,000 \times g for 60 min at 4°C) and filtered (45 μ m) before being used to infect HEK293S GnTI- cells in suspension for protein expression. Suspension HEK293S GnTI- cells were cultured in FreeStyleTM 293 expression medium (Thermo Fisher 12338018) with 1% (v/v) FBS (Sigma) at 37°C, 135 rpm and 8% CO₂. At a cell density of $2-3 \times 10^6$ cells/mL, BacMam P2 virus was added (1:10 v/v). After 18 hours, 10 mM sodium butyrate was added to boost protein expression and the temperature was reduced to 30°C for further 48 hours before harvesting by centrifugation (5,000 \times g for 20 min).

Purification: The cells were lysed with the hypotonic buffer (50 mL buffer per liter of growth culture) 10 mM Tris pH 8 with 1x protease inhibitors (cOmpleteTM, Roche) for 1 h before diluted in TBS buffer (20 mM Tris pH 8, 150 mM NaCl). Cell debris was removed by centrifugation (3,000 \times g for 30 min) before membrane preparation by

ultracentrifugation (186,000×g for 70 min). The membranes were resuspended in TBS buffer supplemented with 5% glycerol, 2 mM 2-mercaptoethanol, 1x protease inhibitors and subsequently solubilized by 1% glyco-diosgenin (GDN) for 1 h. Insoluble material was removed by ultracentrifugation (186,000×g for 40 min) before the supernatant was added to beads containing anti-GFP nanobody (see 5.2.3.4). The beads were washed with TBS buffer supplemented with 2 mM 2-mercaptoethanol, 0.03% GDN before elution with 10 mM glutathione (in wash buffer). Ca²⁺-CaM (see 5.2.3.3) was added at 10x molar excess before the complex was further purified by SEC on an Superose 6 increase 10/300 column (Cytiva) in TBS supplemented with 2 mM 2-mercaptoethanol, 0.02% GDN, 5 mM CaCl₂. Peak fractions were analyzed by SDS-PAGE and concentrated (Amicon centrifugal filter, 100 kDa cut-off, Sigma Aldrich).

5.2.3.6 Zebrafish NUDT9-H domain (*drNUDT9-H*) of TRPM2

The sequence coding for the *drNUDT9-H* domain (residues 1188-1474 of *drTRPM2*) was cloned (see 5.2.2.1 and 5.2.2.2) into a pNEK-vH vector bearing a TEV-cleavable N-terminal His₆-tag. Protein production was carried out in BL21 Gold pLysS (DE3) *E. coli* (see 5.2.1.1) in TB medium supplemented with 25 µg/mL kanamycin and 34 µg/mL chloramphenicol. The cells were grown at 37°C until a density of 1 (measured at 600 nm) was reached, induced with 0.1 mM IPTG and further grown at 20°C for 16 hours.

Cells were harvested by centrifugation (5,000×g for 25 min) and resuspended in 25 mM Tris pH 7.5, 250 mM NaCl, 10% glycerol (v/v) (30 mL buffer per liter of growth culture). 2 µg/mL DNase I with 2 mM MgCl₂ and 0.2 mg/mL lysozyme were added to facilitate lysis which was achieved by high-pressure homogenization (EmulsiFlex-C3, Avestin). Cell debris was removed by centrifugation (39,000×g for 45 min) and the supernatant was subjected to IMAC with Ni-NTA resin (Roth) in a gravity flow column. 2 mL bead volume was used for the lysate of 1 L growth culture. Loading was performed in presence of 5 mM imidazole, 30 mM imidazole was used for washing, and 500 mM imidazole was used for the elution of the His-tagged target protein. The protein was further purified by gel filtration on a Superdex S200 increase 10/300 column (Cytiva) in 25 mM HEPES pH 7.5,

200 mM NaCl. Peak fractions were pooled and protein identity confirmed by SDS-PAGE and mass spectrometry (see 5.2.4.1 and 5.2.4.1).

5.2.3.7 Human P2X7 ballast domain (*hsP2X7BD*)

The expression and purification of *hsP2X7BD* is prepared for publication (Sander et al., 2022b) and was conceptualized as well as performed by the author of this thesis. A pET28a vector was used to express the cytoplasmic ballast domain (P2X7BD, residues 395-595 of *hsP2X7*; cap-P2X7BD, residues 355-395 of *hsP2X7*) of the human P2X7 protein with a TEV-cleavable C-terminal mCherry-His₆-tag. Molecular cloning was performed by Isabell Müller (LMU Munich). Protein expression was carried out in Rosetta 2 (DE3) *E. coli* (see 5.2.1.1) in TB medium supplemented with 25 µg/mL kanamycin and 34 µg/mL chloramphenicol. Cells were induced (0.1 mM IPTG) at a density of 0.6 (measured at 600 nm) and further grown at 20°C for 16 hours.

Cells were harvested by centrifugation (5,000×g for 25 min) and lysed in 25 mM Tris pH 7.5, 300 mM NaCl, 5% (v/v) glycerol, 5 mM 2-mercaptoethanol (100 mL buffer per liter of growth culture) using a high-pressure homogenizer (EmulsiFlex-C3, Avestin). 2 µg/mL DNase I with 2 mM MgCl₂ and 0.2 mg/mL lysozyme were added to facilitate lysis. 0.5 mM phenylmethylsulfonyl fluoride (PMSF) was added to inhibit protease activity. After lysis the lysate was cleared by centrifugation (39,000×g for 45 min) and subsequently subjected to immobilized metal affinity chromatography (IMAC) with Ni-NTA resin (Roth) in a gravity flow column to purify the His₆-tagged fusion protein. 2 mL bead volume was used for the lysate of 1 L growth culture. Loading to the beads was performed in presence of 5 mM imidazole, 30 mM imidazole was used for washing and 400 mM imidazole was used for the elution of the target protein. Further purification was achieved by the removal of the mCherry-His₆ tag by TEV protease (1/10 w/w, self-made in the Tidow lab) over night, subsequent reverse Ni-NTA chromatography and gel filtration on a Superdex S200 increase 10/300 column (Cytiva) in 20 mM HEPES pH 7.5, 150 mM NaCl, 5 mM CaCl₂. Peak fractions of trimeric P2X7BD were pooled and protein identity was confirmed by SDS-PAGE and mass spectrometry (see 5.2.4.1 and 5.2.4.1).

5.2.4 Protein characterization

5.2.4.1 SDS-PAGE

Pure protein samples or protein lysates were separated by sodium dodecyl sulfate-polyacrylamide gel electrophoresis (SDS-PAGE) to assess molecular weight as well as purity. The samples were quantified via absorption at 280 nm (Nanodrop 2000, Thermo Fisher) or Bradford assay (Sigma B6916 according to the manufacturer's protocol) and subsequently mixed with SDS sample buffer. Boiling (5 min at 95°C) was performed before electrophoresis, unless the sample contained detergent. Whole-cell lysates as well as samples from the cell surface biotinylation assay were heated for 5 min at 75°C. After loading (pure proteins: 4 µg, lysates: 50 µg, cell surface biotinylation assay: 12 µg) to a polyacrylamide gel (BioRad Mini-PROTEAN® TGX™ Precast Gel 4-20%) proteins were separated at 200 V for 45 min. Protein standards were used to estimate molecular masses (PageRuler™ Unstained or PageRuler™ Prestained, Thermo Fisher 26614 or 26616). Gels were either stained by Coomassie staining (Quick Coomassie Stain, Biotrend NB-45-00078) according to the manufacturer's instructions or proteins were visualized by western blot (see 5.2.4.2).

5.2.4.2 Western blot

Western blot analysis was performed to detect specific proteins within a protein mixture (e.g. whole-cell lysate). The proteins on an SDS-PAGE gel (see 5.2.4.1) were transferred to a PVDF membrane (Merck Millipore) at 400 mA for 90 min (wet blot in western blot transfer buffer). The membrane was washed with TBST buffer before blocking (5% milk in TBST) for one hour and being cut at 140 kDa to simultaneously detect TRPM2 (171 kDa) and the reference Na⁺/K⁺-ATPase (100 kDa). The membrane parts were probed for 18 h with anti-*hs*TRPM2 antibody from rabbit (Novus #nb500-241 at 1:50,000 dilution in 2.5% milk in TBST) and anti-Na⁺/K⁺-ATPase antibody from rabbit (Cell Signaling #3010 at 1:1,000 dilution in 2.5% BSA in TBST), respectively. After washing with TBST both primary antibodies were detected with an HRP-conjugated anti-rabbit secondary antibody (Dianova #111-035-045 at 1:10,000 dilution) for 1 h. Chemiluminescent detection was

performed using the SuperSignal West Pico substrate (Thermo Fisher) on a Vilber Fusion FX system.

5.2.4.3 Mass spectrometry (MS)

Mass spectrometric (MS) analysis was performed to confirm identity of purified protein samples. After chromatographic separation by SDS-PAGE and Coomassie staining (see 5.2.4.1) specific protein bands were cut out. The bands were sent to the core facility “Mass Spectrometric Proteomics” at the UKE Hamburg where a tryptic digest followed by LC-MS/MS was performed to identify peptides corresponding to the target proteins confirming their presence in the original samples.

5.2.4.4 Analytical size-exclusion chromatography (SEC)

Purified proteins (*drMHR1/2*, 120 μM or *hsP2X7BD*, 250 μM) were mixed with 5x excess of purified Ca^{2+} -calmodulin (600 μM or 1250 μM) and 5x excess of GDP (1250 μM). The mixture was incubated on ice for 30 minutes and subsequently loaded onto size-exclusion chromatography to chromatographically separate the samples according to their native mass. A Superdex S200 increase 10/300 (24 mL bed volume, 500 μL loading volume) or 5/150 (3 mL bed volume, 100 μL loading volume) column (Cytiva) was used in 20 mM HEPES pH 7.5, 150 mM NaCl, 5 mM CaCl_2 . Fractions of the peaks were analyzed by SDS-PAGE (see 5.2.4.1) and MS (see 5.2.4.3).

5.2.4.5 Nano differential scanning fluorimetry (nDSF)

Protein stability was measured by nDSF using a differential scanning fluorimeter (Prometheus, NanoTemper Technologies, Munich). This technique measures the intrinsic tryptophan fluorescence of a protein as a function of temperature and thus reports on protein unfolding and conformational changes as consequences of a change in the tryptophan environment (Alexander et al., 2014; Gao et al., 2020). Further, the aggregation status of the sample is measured by the light intensity loss due to scattering.

Proteins or protein/ligand complexes were subjected to nDSF measurements in capillaries at a concentration of 10-20 μM . A thermal gradient (20°C-95°C, heating rate: 1°C/min) was applied while fluorescence intensities at 330 nm and 350 nm (F_{330} and F_{350}) as well as scattering intensities were measured. The ratio F_{350}/F_{330} as well as the first derivative of this ratio was calculated to determine the melting temperatures of the samples. Scattering data was used to assess the aggregation status of the analyzed proteins.

5.2.4.6 Isothermal titration calorimetry (ITC)

ITC is a technique to directly characterize the thermodynamics of a protein-protein or protein-ligand interaction. One compound (in the ITC syringe) is titrated to the other compound (in the ITC cell) while the temperature is kept constant. Almost any binding event is accompanied by a change in enthalpy or temperature which can be quantified by the calorimeter and thus leads to direct measurements of binding parameters, e.g. dissociation constant (K_D) and enthalpy (Freyer and Lewis, 2008).

Before ITC measurements the buffers of ligands and purified proteins were matched, meaning that ligands were dissolved or diluted in the buffer used for size-exclusion chromatography of the protein to avoid a buffer mismatch which results in high ITC background signals. The concentration of ligands (amongst others: peptides from GL Biochem, Shanghai, China) was adjusted to 300 μM -1500 μM and they were placed in the ITC syringe. Proteins were diluted to 5 μM -20 μM and loaded to the ITC cell. Measurements were carried out at 25°C on a MicroCal ITC-200 calorimeter (Malvern Panalytical) and thermodynamic parameters were analyzed with the MicroCal™ software. After an initial injection (0.5 μL) 18 regular injections (2 μL each) were added from the syringe to the cell. Stirring speed was set to 750 rpm and individual injections were interspaced by 150 seconds. All measurements were performed as triplicates and ligands were titrated into buffer to allow for baseline subtraction due to heat of dilution. Errors are reported as standard deviations of the mean K_D value.

5.2.4.7 Microscale thermophoresis (MST)

The directed movement of particles in a temperature gradient (thermophoresis) can be used to analyze protein-ligand interactions. The thermophoresis of a protein alone is typically significantly different compared to a protein-ligand complex because ligand binding causes changes in size, charge and solvation energy. MST devices quantify these changes by measuring the fluorescence distribution within capillaries upon heating of defined areas with a laser (Jerabek-Willemsen et al., 2014). The machine that was used in this study (Monolith NT.LabelFree, NanoTemper Technologies, Munich) measures the change of the intrinsic tryptophan fluorescence of the analyzed proteins.

Proteins were diluted to 500 nM in MST buffer including 0.1% Pluronic (NanoTemper Technologies, Munich) and mixed with different amounts of ligands which were also diluted in the same buffer. Measurements were performed according to the MO.Control software (NanoTemper Technologies, Munich) and binding parameters were calculated with the MO.Affinity Analysis software (NanoTemper Technologies, Munich).

5.2.4.8 Protein cross-linking

Purified P2X7BD and Ca²⁺-CaM were used for cross-linking experiments to visualize the protein-protein complexes that the two interaction partners form. Both proteins (50 µM each in 25 µL total volume) were mixed in 20 mM HEPES pH 7.5, 150 mM NaCl, 2 mM CaCl₂. The chemical cross-linking reagent disuccinimidyl suberate (DSS, Thermo Fisher 21655) was added at 50x excess (2.5 mM final concentration, from a fresh 50 mM stock in DMSO) before incubation for 30 minutes at room temperature. DSS is non-cleavable, reacts with two primary amines (e.g. in lysine residues or the N-terminus of a protein) at pH 7-9 and forms a stable amide bond. The reaction was quenched by the addition of 50 mM Tris pH 7.5 which contains a primary amine group. After 15 minutes of incubation at room temperature SDS sample buffer was added and the samples were boiled at 95°C for five minutes before analysis by SDS-PAGE (see 5.2.4.1).

5.2.5 Protein crystallization and structure determination

Protein crystallography is a powerful method to obtain three-dimensional structure information on a molecular level. In general, the atoms within a protein crystal cause a beam of X-rays to diffract into many distinct directions making it possible to calculate exact atom positions of the original protein molecule (Chayen and Saridakis, 2008). However, it is impossible to experimentally measure the phases of the incident X-rays, which are necessary for structure determination. One method to determine the phases is selenium single-wavelength anomalous dispersion (Se-SAD). The use of selenomethionine instead of the natural sulfur-methionine gives rise to measurable intensity changes due to the heavy atoms that can be used to deduce their positions. Protein crystallization and structure determination of *drMHR1/2* is published (Sander et al., 2022a) and was conceptualized as well as performed by the author of this thesis.

Crystals of selenomethionine-labelled *drMHR1/2* protein were grown by sitting drop vapour diffusion technique. 1 μL of purified protein at 4 mg/mL was mixed with 1 μL of the precipitant mix (Tris, BICINE, diethylene glycol, triethylene glycol, tetraethylene glycol, pentaethylene glycol, glycerol, PEG4000, Jeffamine[®] M-600). Crystals of triangular shape appeared after one to three days, reaching sizes of approximately 50-120 μm .

X-ray diffraction data were collected at 100 K at the PETRA III/EMBL P14 beamline (Hamburg). All datasets were processed with XDS (Kabsch, 2010) and merged with AIMLESS (Evans and Murshudov, 2013). Heavy atom site identification and phasing was performed with SHELXCD (Sheldrick, 2008). A combination of ARP/wARP (Langer et al., 2008) and COOT (Emsley et al., 2010) was used for automatic and manual model building, respectively. Metal ion analysis and confirmation of Zn^{2+} ion in the structure was performed with the *CheckMyMetal* server (Zheng et al., 2017). Refinement was carried out in PHENIX (Liebschner et al., 2019). The final model corresponds to residues 38-423 and has been deposited in the RCSB Protein Data Bank under accession number 7AOV. All data collection and refinement statistics are summarized in Table 5.11.

Table 5.11: Crystallographic data collection and refinement statistics of *drMHR1/2*. Data from the last resolution shell are in parentheses.

Data collection	
Beamline	PETRA III, P13
Wavelength (Å)	0.98
Resolution (Å)	46.6 - 2.0 (2.07 - 2.00)
Space group	P 1 2 ₁ 1
Cell dimensions	
a, b, c (Å)	47.8, 188.1, 47.8
α , β , γ (°)	90.0, 102.7, 90.0
Completeness (%)	97.2 (96.9)
Mean I/ σ (I)	10.3 (1.5)
R _{meas}	0.288 (1.88)
R _{pim}	0.077 (0.51)
CC _{1/2}	0.996 (0.552)
Multiplicity	13.9 (13.6)
Refinement	
Reflections used in refinement	53670 (5367)
R _{work} / R _{free}	0.19 / 0.23
Number of non-hydrogen atoms	6373
macromolecules	5956
ligands/ions	2
Average B-factor (Å ²)	45.7
macromolecules (Å ²)	45.5
ligands/ions (Å ²)	30.5
RMS _{bonds} (Å)	0.008
RMS _{angles} (°)	0.97
Ramachandran	
Favored regions (%)	95.8
Allowed regions (%)	3.8
Outliers (%)	0.4
Rotamer outliers (%)	0.0

5.2.6 Hydrolase assay by high performance liquid chromatography (HPLC)

To assess the enzymatic activity of *drNUDT9-H*, the nucleotides ADPR and 2'-deoxy-ADPR were incubated with the protein. The resulting products (AMP/2'-deoxy-AMP and ribose 5-phosphate) were subjected to HPLC analysis.

Protein (30 μ M *drNUDT9-H*) and nucleotides (100 μ M) were mixed in a total volume of 150 μ L (buffer: 50 mM KH_2PO_4 pH 7.2, 2 mM MgCl_2) and incubated for an hour at 28°C. The reaction was stopped by the addition of 1 mM KF. Reaction products were separated from the protein with a Vivaspin 500 concentrator (10 kDa cut-off, Sigma Aldrich) at 10,000 \times g for 10 min. Methanol (10% v/v) was added to the flow-through before analysis by HPLC. The nucleotides were separated on a Multohyp BDS C18 column (particle size: 5 μ m, 250 \times 4.6 mm, Chromatographie Service, Langerwehe, Germany) connected to an Agilent 1260 infinity module (Agilent Technologies) while a gradient with increasing methanol concentrations was applied: 0 min (15%), 3.5 min (15%), 11 min (31.25%), 15 min (31.25%), 25 min (50%), 27 min (50%), 29 min (15%), 38 min (15%). ChemStation software (Agilent Technologies) was used for acquisition and data analysis. A diode-array detector (Agilent Technologies) was used to detect the nucleotides at 260 nm. Pure ADPR/2'-deoxy-ADPR and AMP/2'-deoxy-AMP were used as external standards to identify retention times.

5.2.7 Size-exclusion chromatography small-angle X-ray scattering (SEC-SAXS)

SAXS is a method that provides low-resolution structural information of biological macromolecules in solution. It is becoming a standard tool for protein characterization especially because large conformational changes can be visualized by SAXS (Svergun et al., 2013). Coupled to a size-exclusion chromatography system (SEC-SAXS) even protein complexes or mixtures can be analyzed due to the separation of the individual components resulting in individual SAXS patterns (Panjkovich and Svergun, 2018). The SEC-SAXS method for P2X7BD with Ca^{2+} -CaM is prepared for publication (Sander et al., 2022b), was also used for *drMHR1/2* with Ca^{2+} -CaM and was conceptualized as well as performed by the author of this thesis.

All SEC-SAXS measurements were executed on the Bio-SAXS beamline P12 on the storage ring PETRA III (DESY, Hamburg, Germany). Samples were chromatographically separated using an S200 increase 5/150 column in 20 mM HEPES pH 7.5, 150 mM NaCl, 5 mM CaCl₂ before the measurement. SEC-SAXS data analysis was performed with CHROMIXS (Panjkovich and Svergun, 2018) as part of the ATSAS 3.0 package (Manalastas-Cantos et al., 2021). Peaks were assigned based on the SEC information from the purification process. Radii of gyration (R_g), Porod volumes and MW estimates were obtained from buffer subtracted scattering curves using the Guinier approximation (Manalastas-Cantos et al., 2021). The distance distribution function ($P(r)$) and the maximal protein dimension (D_{max}) were calculated from the entire scattering curve using the program GNOM (Svergun, 1992). Furthermore, *ab initio* models were generated using DAMMIF (Franke and Svergun, 2009).

5.2.8 Electron microscopy

Negative-stain electron microscopy was used for the visualization of *hsTRPM2* particles. Continuous carbon-coated 300 mesh grids (Plano GmbH S160-3) were glow-discharged for 30 s to render them hydrophilic (GlowQube, Quorum Technologies) before adding 2 μ L of sample (1 mg/mL) to the carbon-coated side. After 30 s adsorption time, excess sample was blotted off with filter paper before the grid was washed twice with water. Uranyl formate (0.75% in water) stain was applied twice for 30 s and excess stain was removed by blotting with a filter paper. The dried grids were analyzed by electron microscopy. A TALOS L120C transmission electron microscope (Thermo Fisher) was used to screen grids and also for image acquisition at 57,000x and 92,000x magnification.

5.2.9 Cell surface biotinylation assay

The cell surface biotinylation assay analyzing *hsTRPM2* variants is published (Sander et al., 2022a), was conceptualized by Jelena Pick/Ralf Fliegert and performed by the author of this thesis. The assay visualizes if TRPM2 protein mutants are correctly synthesized within the cell and subsequently transported to the plasma membrane.

HEK293 wild type cells (cultivated in DMEM at 37°C and 5% CO₂) were transfected with pIRES2-EGFP vectors containing *hsTRPM2* variants (wild type, C89A, C91A, C89A C91A double mutant) or empty vector using lipofectamine LTX (Thermo Fisher) according to the manufacturer's instructions. Transfection was verified by fluorescence microscopy. Cells were grown for 48 hours after transfection, washed with PBS and incubated with 1 mg/mL EZ-Link Sulfo-NHS-LC-Biotin in PBS (Thermo Fisher) in order to biotinylate cell surface proteins. After detachment with 2 mM EDTA in PBS, the cells were collected, centrifuged (500 g for 5 min) and washed with PBS. Cell lysis and membrane protein extraction was performed using the ProteoExtract Native Membrane kit (Sigma 444810) according to the manufacturer's protocol. Solubilized membrane protein samples were quantified by Bradford assay.

NeutraVidin Agarose beads (70 µL, Thermo Fisher) were used to isolate the biotinylated cell surface proteins. The beads were incubated with total membrane protein samples (600 µg) for 18 h while rotating at 4°C. After washing with extraction buffer II from the kit mentioned above, the beads as well as the total membrane protein samples were mixed with SDS sample buffer and heated to 75°C for 5 min. The samples were analyzed by SDS-PAGE (see 5.2.4.1) and western blot (see 5.2.4.2).

5.2.10 Electrophysiology (patch clamp)

The patch clamp technique is a versatile tool to investigate ion channel behavior. In this study, the so-called whole-cell mode was performed: This mode involves a glass micropipette that is sealed to the cell membrane of a single cell to be analyzed. Subsequent rupture of the membrane patch below the pipette tip gives a microelectrode inside the pipette electrical access to the cytosol. A voltage clamp is applied using a second electrode in the extracellular solution. The measured membrane currents contain information about the characteristics of the ion channels within the membrane of the analyzed cell (Molleman, 2002).

Patch clamp measurements with *hsTRPM2* variants are published (Sander et al., 2022a), were conceptualized by Ralf Fliegert and performed by the author of this thesis. HEK293 cells were transfected 24 hours prior to experiments using jetPEI reagent (Polyplus

transfection). The transfection complex (5 μg DNA and 10 μL jetPEI reagent in 150 mM NaCl solution at a total volume of 250 μL) was incubated for 30 minutes before 2.5×10^5 cells were added. The cell suspension was subsequently seeded to 35 mm dishes at low density. Patch clamp experiments were performed at room temperature. Before the start of the experiments the medium was replaced by patch clamp extracellular solution. Patch pipettes were pulled from 1.05 x 1.50 x 80 mm glass capillaries and filled with patch clamp intracellular solution (200 nM intracellular Ca^{2+} , as calculated with Maxchelator: <https://somapp.ucdmc.ucdavis.edu/pharmacology/bers/maxchelator>). After pipette resistances were determined (1.5 - 2.9 M Ω) currents were compensated for fast and slow capacity transients and recorded in whole-cell configuration. The series resistance compensation was set to 70%. Using voltage clamp, repetitive voltage ramps of 140 ms spanning the range from -85 mV to +20 mV were applied from a holding potential of -50 mV every 5 s over a measuring period of 450 s. For data analysis, the maximum outward current at +15 mV of each measuring period was extracted from all experiments. Cells with a series resistance >10 M Ω during the experiment were excluded from data analysis.

Statistical analysis was performed with GraphPad Prism (v9, GraphPad Software). After normal distribution was confirmed by Kolmogorov-Smirnov test, one-way ANOVA test was applied followed by Dunnett test for multiple comparisons.

5.2.11 Multiple sequence alignment

Multiple sequence alignment of TRPM2 and homologues was performed using the Clustal Omega server (Madeira et al., 2019). Results were visualized with Jalview (<https://www.jalview.org/>).

5.2.12 Molecular graphics

Molecular graphics and analyses were performed with PyMol (Version 2.1, Schrödinger, LLC) and UCSF Chimera (Pettersen et al., 2004). UCSF Chimera was developed by the Resource for Biocomputing, Visualization, and Informatics at the University of California, San Francisco, with support from NIH P41-GM103311.

6 REFERENCES

- Abriel, H., Syam, N., Sottas, V., Amarouch, M.Y., and Rougier, J.-S. (2012). TRPM4 channels in the cardiovascular system: Physiology, pathophysiology, and pharmacology. *Biochem. Pharmacol.* *84*, 873–881.
- Abuarab, N., Munsey, T.S., Jiang, L.H., Li, J., and Sivaprasadarao, A. (2017). High glucose-induced ROS activates TRPM2 to trigger lysosomal membrane permeabilization and Zn²⁺-mediated mitochondrial fission. *Sci. Signal.* *10*, 1–12.
- Adinolfi, E., Cirillo, M., Woltersdorf, R., Falzoni, S., Chiozzi, P., Pellegatti, P., Callegari, M.G., Sandonà, D., Markwardt, F., Schmalzing, G., et al. (2010). Trophic activity of a naturally occurring truncated isoform of the P2X7 receptor. *FASEB J.* *24*, 3393–3404.
- Adinolfi, E., Giuliani, A.L., De Marchi, E., Pegoraro, A., Orioli, E., and Di Virgilio, F. (2018). The P2X7 receptor: A main player in inflammation. *Biochem. Pharmacol.* *151*, 234–244.
- Alexander, C.G., Wanner, R., Johnson, C.M., Breitsprecher, D., Winter, G., Duhr, S., Baaske, P., and Ferguson, N. (2014). Novel microscale approaches for easy, rapid determination of protein stability in academic and commercial settings. *Biochim. Biophys. Acta - Proteins Proteomics* *1844*, 2241–2250.
- Almasi, S., Kennedy, B.E., El-Aghil, M., Sterea, A.M., Gujar, S., Partida-Sánchez, S., and El Hiani, Y. (2018). TRPM2 channel-mediated regulation of autophagy maintains mitochondrial function and promotes gastric cancer cell survival via the JNK-signaling pathway. *J. Biol. Chem.* *293*, 3637–3650.
- Amoroso, F., Capece, M., Rotondo, A., Cangelosi, D., Ferracin, M., Franceschini, A., Raffaghello, L., Pistoia, V., Varesio, L., and Adinolfi, E. (2015). The P2X7 receptor is a key modulator of the PI3K/GSK3 β /VEGF signaling network: evidence in experimental neuroblastoma. *Oncogene* *34*, 5240–5251.
- Autzen, H.E., Myasnikov, A.G., Campbell, M.G., Asarnow, D., Julius, D., and Cheng, Y. (2018). Structure of the human TRPM4 ion channel in a lipid nanodisc. *Science (80-.)*. *359*, 228–232.
- Bagur, R., and Hajnóczky, G. (2017). Intracellular Ca²⁺ Sensing: Its Role in Calcium Homeostasis and Signaling. *Mol. Cell* *66*, 780–788.
- Bao, L., Chen, S., Conrad, K., Keefer, K., Abraham, T., Lee, J.P., Wang, J., Zhang, X.-Q., Hirschler-Laszkiwicz, I., Wang, H.-G., et al. (2016). Depletion of the Human Ion Channel TRPM2 in Neuroblastoma Demonstrates Its Key Role in Cell Survival through Modulation of Mitochondrial Reactive Oxygen Species and Bioenergetics. *J. Biol. Chem.* *291*, 24449–24464.
- Bartlett, R., Stokes, L., and Sluyter, R. (2014). The P2X7 Receptor Channel: Recent Developments and the Use of P2X7 Antagonists in Models of Disease. *Pharmacol. Rev.* *66*, 638–675.
- Baszczyński, O., Watt, J.M., Rozewitz, M.D., Guse, A.H., Fliegert, R., and Potter, B.V.L. (2019). Synthesis of Terminal Ribose Analogues of Adenosine 5'-Diphosphate Ribose as Probes for the Transient Receptor Potential Cation Channel TRPM2. *J. Org. Chem.* *84*,

6143–6157.

Baszczyński, O., Watt, J.M., Rozewitz, M.D., Fliegert, R., Guse, A.H., and Potter, B.V.L. (2020). Synthesis of phosphonoacetate analogues of the second messenger adenosine 5'-diphosphate ribose (ADPR). *RSC Adv.* *10*, 1776–1785.

Bhattacharya, A., and Biber, K. (2016). The microglial ATP-gated ion channel P2X7 as a CNS drug target. *Glia* *64*, 1772–1787.

Blenn, C., Wyrsh, P., Bader, J., Bollhalder, M., and Althaus, F.R. (2011). Poly(ADP-ribose)glycohydrolase is an upstream regulator of Ca²⁺ fluxes in oxidative cell death. *Cell. Mol. Life Sci.* *68*, 1455–1466.

Brake, A.J., Wagenbach, M.J., and Julius, D. (1994). New structural motif for ligand-gated ion channels defined by an ionotropic ATP receptor. *Nature* *371*, 519–523.

Buelow, B., Song, Y., and Scharenberg, A.M. (2008). The Poly(ADP-ribose) Polymerase PARP-1s Required for Oxidative Stress-induced TRPM2 Activation in Lymphocytes. *J. Biol. Chem.* *283*, 24571–24583.

Burnstock, G. (1972). Purinergic nerves. *Pharmacol. Rev.* *24*, 509–581.

Burnstock, G. (1976). Do some nerve cells release more than one transmitter? *Neuroscience* *1*, 239–248.

Burnstock, G. (1978). A basis for distinguishing two types of purinergic receptor. In *Cell Membrane Receptors for Drugs and Hormones: A Multidisciplinary Approach*, R.W. Straub, and L. Bolis, eds. pp. 107–118.

Burnstock, G., and Kennedy, C. (1985). Is there a basis for distinguishing two types of P₂-purinoceptor? *Gen. Pharmacol. Vasc. Syst.* *16*, 433–440.

Burnstock, G., and Knight, G.E. (2004). Cellular Distribution and Functions of P₂ Receptor Subtypes in Different Systems. In *International Review of Cytology*, pp. 31–304.

Burnstock, G., and Knight, G.E. (2018). The potential of P₂X₇ receptors as a therapeutic target, including inflammation and tumour progression. *Purinergic Signal.* *14*, 1–18.

Burnstock, G., Holman, M.E., and Kuriyama, H. (1964). Facilitation of transmission from autonomic nerve to smooth muscle of guinea-pig vas deferens. *J. Physiol.* *172*, 31–49.

Burnstock, G., Campbell, G., Satchell, D., and Smythe, A. (1970). Evidence that adenosine triphosphate or a related nucleotide is the transmitter substance released by non-adrenergic inhibitory nerves in the gut. *Br. J. Pharmacol.* *40*, 668–688.

Calik, I., Calik, M., Turken, G., and Ozercan, I.H. (2020). A promising independent prognostic biomarker in colorectal cancer: P₂X₇ receptor. *Int. J. Clin. Exp. Pathol.* *13*, 107–121.

Caterina, M.J., Schumacher, M.A., Tominaga, M., Rosen, T.A., Levine, J.D., and Julius, D. (1997). The capsaicin receptor: a heat-activated ion channel in the pain pathway. *Nature* *389*, 816–824.

Chayen, N.E., and Saridakis, E. (2008). Protein crystallization: from purified protein to diffraction-quality crystal. *Nat. Methods* *5*, 147–153.

- Cheewatrakoolpong, B., Gilchrest, H., Anthes, J.C., and Greenfeder, S. (2005). Identification and characterization of splice variants of the human P2X7 ATP channel. *Biochem. Biophys. Res. Commun.* *332*, 17–27.
- Cimpmperman, P., Baranauskienė, L., Jachimovičiūtė, S., Jachno, J., Torresan, J., Michailovienė, V., Matulienė, J., Sereikaitė, J., Bumelis, V., and Matulis, D. (2008). A Quantitative Model of Thermal Stabilization and Destabilization of Proteins by Ligands. *Biophys. J.* *95*, 3222–3231.
- Cohen, M.S., and Chang, P. (2018). Insights into the biogenesis, function, and regulation of ADP-ribosylation. *Nat. Chem. Biol.* *14*, 236–243.
- Crivici, A., and Ikura, M. (1995). Molecular and structural basis of target recognition by calmodulin. *Annu. Rev. Biophys. Biomol. Struct.* *24*, 85–116.
- Csanády, L., and Töröcsik, B. (2009). Four Ca²⁺ Ions Activate TRPM2 Channels by Binding in Deep Crevices near the Pore but Intracellularly of the Gate. *J. Gen. Physiol.* *133*, 189–203.
- Dang, S., van Goor, M.K., Asarnow, D., Wang, Y., Julius, D., Cheng, Y., and van der Wijk, J. (2019). Structural insight into TRPV5 channel function and modulation. *Proc. Natl. Acad. Sci.* *116*, 8869–8878.
- DeLeo, J.A. (2006). Basic science of pain. *J. Bone Joint Surg. Am.* *88 Suppl 2*, 58–62.
- Diver, M.M., Cheng, Y., and Julius, D. (2019). Structural insights into TRPM8 inhibition and desensitization. *Science (80-.)*. *365*, 1434–1440.
- Duan, J., Li, Z., Li, J., Santa-Cruz, A., Sanchez-Martinez, S., Zhang, J., and Clapham, D.E. (2018a). Structure of full-length human TRPM4. *Proc. Natl. Acad. Sci.* *115*, 2377–2382.
- Duan, J., Li, Z., Li, J., Hulse, R.E., Santa-Cruz, A., Valinsky, W.C., Abiria, S.A., Krapivinsky, G., Zhang, J., and Clapham, D.E. (2018b). Structure of the mammalian TRPM7, a magnesium channel required during embryonic development. *Proc. Natl. Acad. Sci.* *115*, E8201–E8210.
- Emsley, P., Lohkamp, B., Scott, W.G., and Cowtan, K. (2010). Features and development of Coot. *Acta Crystallogr. Sect. D Biol. Crystallogr.* *66*, 486–501.
- Ernfors, P., Manira, A. El, and Svenningsson, P. (2021). Discoveries of receptors for temperature and touch. *Noble Assem. Karolinska Institutet* 2–5.
- Evans, P.R., and Murshudov, G.N. (2013). How good are my data and what is the resolution? *Acta Crystallogr. Sect. D Biol. Crystallogr.* *69*, 1204–1214.
- Faouzi, M., and Penner, R. (2014). Mammalian transient receptor potential (TRP) cation channels.
- Ferrari, D., Pizzirani, C., Adinolfi, E., Lemoli, R.M., Curti, A., Idzko, M., Panther, E., and Di Virgilio, F. (2006). The P2X 7 Receptor: A Key Player in IL-1 Processing and Release. *J. Immunol.* *176*, 3877–3883.
- Fliegert, R., Watt, J.M., Schöbel, A., Rozewitz, M.D., Moreau, C., Kirchberger, T., Thomas, M.P., Sick, W., Araujo, A.C., Harneit, A., et al. (2017a). Ligand-induced activation of human TRPM2 requires the terminal ribose of ADPR and involves Arg1433 and Tyr1349. *Biochem. J.* *474*, 2159–2175.

- Fliegert, R., Bauche, A., Wolf Pérez, A.-M., Watt, J.M., Rozewitz, M.D., Winzer, R., Janus, M., Gu, F., Rosche, A., Harneit, A., et al. (2017b). 2'-Deoxyadenosine 5'-diphosphoribose is an endogenous TRPM2 superagonist. *Nat. Chem. Biol.* *13*, 1036–1044.
- Fonfria, E., Murdock, P.R., Cusdin, F.S., Benham, C.D., Kelsell, R.E., and McNulty, S. (2006). Tissue Distribution Profiles of the Human TRPM Cation Channel Family. *J. Recept. Signal Transduct.* *26*, 159–178.
- Franke, D., and Svergun, D. (2009). DAMMIF , a program for rapid ab-initio shape determination in small-angle scattering. *J. Appl. Crystallogr.* *42*, 342–346.
- Freyer, M.W., and Lewis, E.A. (2008). Isothermal Titration Calorimetry: Experimental Design, Data Analysis, and Probing Macromolecule/Ligand Binding and Kinetic Interactions. In *Methods in Cell Biology*, pp. 79–113.
- Galione, A., Lee, H.C., and Busa, W.B. (1991). Ca²⁺-Induced Ca²⁺ Release in Sea Urchin Egg Homogenates: Modulation by Cyclic ADP-Ribose. *Science (80-.)*. *253*, 1143–1146.
- Gao, K., Oerlemans, R., and Groves, M.R. (2020). Theory and applications of differential scanning fluorimetry in early-stage drug discovery. *Biophys. Rev.* *12*, 85–104.
- Gattkowsky, E. (2021). Biophysical characterization of the pyrophosphatase NUDT9 and the NUDT9- homologous domain of the TRPM2 channel. University of Hamburg.
- Gattkowsky, E., Johnsen, A., Bauche, A., Möckl, F., Kulow, F., Garcia Alai, M., Rutherford, T.J., Fliegert, R., and Tidow, H. (2019). Novel CaM-binding motif in its NudT9H domain contributes to temperature sensitivity of TRPM2. *Biochim. Biophys. Acta - Mol. Cell Res.* *1866*, 1162–1170.
- Gattkowsky, E., Rutherford, T.J., Möckl, F., Bauche, A., Sander, S., Fliegert, R., and Tidow, H. (2021). Analysis of ligand binding and resulting conformational changes in pyrophosphatase NUDT9. *FEBS J.* *288*, 6769–6782.
- Gifford, J.L., Walsh, M.P., and Vogel, H.J. (2007). Structures and metal-ion-binding properties of the Ca²⁺-binding helix–loop–helix EF-hand motifs. *Biochem. J.* *405*, 199–221.
- Gomez-Villafuertes, R., and Adinolfi, E. (2020). Editorial: Emerging Mechanisms in Purinergic Signaling: From Cell Biology to Therapeutic Perspectives. *Front. Pharmacol.* *11*, 10–11.
- Gonnord, P., Delarasse, C., Auger, R., Benihoud, K., Prigent, M., Cuif, M.H., Lamaze, C., and Kanellopoulos, J.M. (2009). Palmitoylation of the P2X7 receptor, an ATP-gated channel, controls its expression and association with lipid rafts. *FASEB J.* *23*, 795–805.
- Granzotto, A., Canzoniero, L.M.T., and Sensi, S.L. (2020). A Neurotoxic Ménage-à-trois: Glutamate, Calcium, and Zinc in the Excitotoxic Cascade. *Front. Mol. Neurosci.* *13*, 1–13.
- Guo, J., She, J., Zeng, W., Chen, Q., Bai, X., and Jiang, Y. (2017). Structures of the calcium-activated, non-selective cation channel TRPM4. *Nature* *552*, 205–209.
- Halliwel, B. (2006). Oxidative stress and neurodegeneration: Where are we now? *J. Neurochem.* *97*, 1634–1658.
- Hara, Y., Wakamori, M., Ishii, M., Maeno, E., Nishida, M., Yoshida, T., Yamada, H., Shimizu,

- S., Mori, E., Kudoh, J., et al. (2002). LTRPC2 Ca²⁺-Permeable Channel Activated by Changes in Redox Status Confers Susceptibility to Cell Death. *Mol. Cell* 9, 163–173.
- Harteneck, C., Plant, T.D., and Schultz, G. (2000). From worm to man: three subfamilies of TRP channels. *Trends Neurosci.* 23, 159–166.
- Hecquet, C.M., Zhang, M., Mittal, M., Vogel, S.M., Di, A., Gao, X., Bonini, M.G., and Malik, A.B. (2014). Cooperative interaction of trp melastatin channel transient receptor potential (TRPM2) with its splice variant TRPM2 short variant is essential for Endothelial cell Apoptosis. *Circ. Res.* 114, 469–479.
- Heiner, I., Eisfeld, J., Warnstedt, M., Radukina, N., Jüngling, E., and Lückhoff, A. (2006). Endogenous ADP-ribose enables calcium-regulated cation currents through TRPM2 channels in neutrophil granulocytes. *Biochem. J.* 398, 225–232.
- Howard, M., Grimaldi, J., Bazan, J., Lund, F., Santos-Argumedo, L., Parkhouse, R., Walseth, T., and Lee, H. (1993). Formation and hydrolysis of cyclic ADP-ribose catalyzed by lymphocyte antigen CD38. *Science* (80-). 262, 1056–1059.
- Huang, Y., Winkler, P.A., Sun, W., Lü, W., and Du, J. (2018). Architecture of the TRPM2 channel and its activation mechanism by ADP-ribose and calcium. *Nature* 562, 145–149.
- Huang, Y., Roth, B., Lü, W., and Du, J. (2019). Ligand recognition and gating mechanism through three ligand-binding sites of human TRPM2 channel. *Elife* 8, 1–18.
- Huang, Y., Fliegert, R., Guse, A.H., Lü, W., and Du, J. (2020). A structural overview of the ion channels of the TRPM family. *Cell Calcium* 85, 102111.
- Iordanov, I., Mihályi, C., Tóth, B., and Csanády, L. (2016). The proposed channel-enzyme transient receptor potential melastatin 2 does not possess ADP ribose hydrolase activity. *Elife* 5, 1–20.
- Iordanov, I., Tóth, B., Szollosi, A., and Csanády, L. (2019). Enzyme activity and selectivity filter stability of ancient TRPM2 channels were simultaneously lost in early vertebrates. *Elife* 8, 1–23.
- Jarvis, M.F., and Khakh, B.S. (2009). ATP-gated P2X cation-channels. *Neuropharmacology* 56, 208–215.
- Jerabek-Willemsen, M., André, T., Wanner, R., Roth, H.M., Duhr, S., Baaske, P., and Breitsprecher, D. (2014). MicroScale Thermophoresis: Interaction analysis and beyond. *J. Mol. Struct.* 1077, 101–113.
- Jumper, J., Evans, R., Pritzel, A., Green, T., Figurnov, M., Ronneberger, O., Tunyasuvunakool, K., Bates, R., Žídek, A., Potapenko, A., et al. (2021). Highly accurate protein structure prediction with AlphaFold. *Nature* 596, 583–589.
- Kabir, A., Honda, R.P., Kamatari, Y.O., Endo, S., Fukuoka, M., and Kuwata, K. (2016). Effects of ligand binding on the stability of aldo-keto reductases: Implications for stabilizer or destabilizer chaperones. *Protein Sci.* 25, 2132–2141.
- Kabsch, W. (2010). Xds. *Acta Crystallogr. D. Biol. Crystallogr.* 66, 125–132.
- Kambe, T., Tsuji, T., Hashimoto, A., and Isumura, N. (2015). The physiological, biochemical, and molecular roles of zinc transporters in zinc homeostasis and

metabolism. *Physiol. Rev.* 95, 749–784.

Karasawa, A., and Kawate, T. (2016). Structural basis for subtype-specific inhibition of the P2X7 receptor. *Elife* 5, 1–17.

Karasawa, A., Michalski, K., Mikhelzon, P., and Kawate, T. (2017). The P2X7 receptor forms a dye-permeable pore independent of its intracellular domain but dependent on membrane lipid composition. *Elife* 6, 1–22.

Kasuya, G., Yamaura, T., Ma, X.-B., Nakamura, R., Takemoto, M., Nagumo, H., Tanaka, E., Dohmae, N., Nakane, T., Yu, Y., et al. (2017). Structural insights into the competitive inhibition of the ATP-gated P2X receptor channel. *Nat. Commun.* 8, 876.

Kawate, T., Michel, J.C., Birdsong, W.T., and Gouaux, E. (2009). Crystal structure of the ATP-gated P2X4 ion channel in the closed state. *Nature* 460, 592–598.

Klumpp, D., Misovic, M., Sztejn, K., Shumilina, E., Rudner, J., and Huber, S.M. (2016). Targeting TRPM2 channels impairs radiation-induced cell cycle arrest and fosters cell death of T cell leukemia cells in a Bcl-2-dependent manner. *Oxid. Med. Cell. Longev.* 2016, 1–14.

Knowles, H., Heizer, J.W., Li, Y., Chapman, K., Ogden, C.A., Andreasen, K., Shapland, E., Kucera, G., Mogan, J., Humann, J., et al. (2011). Transient Receptor Potential Melastatin 2 (TRPM2) ion channel is required for innate immunity against *Listeria monocytogenes*. *Proc. Natl. Acad. Sci.* 108, 11578–11583.

Koch-Nolte, F., Reche, P., Haag, F., and Bazan, F. (2001). ADP-ribosyltransferases: plastic tools for inactivating protein and small molecular weight targets. *J. Biotechnol.* 92, 81–87.

Kochańczyk, T., Drozd, A., and Krężel, A. (2015). Relationship between the architecture of zinc coordination and zinc binding affinity in proteins – insights into zinc regulation. *Metallomics* 7, 244–257.

Koivisto, A.-P., Belvisi, M.G., Gaudet, R., and Szallasi, A. (2022). Advances in TRP channel drug discovery: from target validation to clinical studies. *Nat. Rev. Drug Discov.* 21, 41–59.

Kolisek, M., Beck, A., Fleig, A., and Penner, R. (2005). Cyclic ADP-Ribose and Hydrogen Peroxide Synergize with ADP-Ribose in the Activation of TRPM2 Channels. *Mol. Cell* 18, 61–69.

Kopp, R., Krautloher, A., Ramírez-Fernández, A., and Nicke, A. (2019). P2X7 Interactions and Signaling – Making Head or Tail of It. *Front. Mol. Neurosci.* 12, 1–25.

Koshimizu, T., Koshimizu, M., and Stojilkovic, S.S. (1999). Contributions of the C-terminal Domain to the Control of P2X Receptor Desensitization. *J. Biol. Chem.* 274, 37651–37657.

Kuhlbrandt, W. (2014). The Resolution Revolution. *Science* (80-.). 343, 1443–1444.

Kühn, F.J.P., and Lückhoff, A. (2004). Sites of the NUDT9-H domain critical for ADP-ribose activation of the cation channel TRPM2. *J. Biol. Chem.* 279, 46431–46437.

Kühn, F.J.P., Heiner, I., and Lückhoff, A. (2005). TRPM2: a calcium influx pathway regulated by oxidative stress and the novel second messenger ADP-ribose. *Pflügers Arch. - Eur. J. Physiol.* 451, 212–219.

- Kühn, F.J.P., Kühn, C., Winking, M., Hoffmann, D.C., and Lückhoff, A. (2016). ADP-Ribose Activates the TRPM2 Channel from the Sea Anemone *Nematostella vectensis* Independently of the NUDT9H Domain. *PLoS One* *11*, e0158060.
- Kühn, F.J.P., Ehrlich, W., Barth, D., Kühn, C., and Lückhoff, A. (2019a). Functional importance of NUDT9H domain and N-terminal ADPR-binding pocket in two species variants of vertebrate TRPM2 channels. *Sci. Rep.* *9*, 19224.
- Kühn, F.J.P., Watt, J.M., Potter, B.V.L., and Lückhoff, A. (2019b). Different substrate specificities of the two ADPR binding sites in TRPM2 channels of *Nematostella vectensis* and the role of IDPR. *Sci. Rep.* *9*, 4985.
- Lange, I., Yamamoto, S., Partida-Sanchez, S., Mori, Y., Fleig, A., and Penner, R. (2009). TRPM2 Functions as a Lysosomal Ca²⁺-Release Channel in β Cells. *Sci. Signal.* *2*, 3174–3185.
- Langer, G., Cohen, S.X., Lamzin, V.S., and Perrakis, A. (2008). Automated macromolecular model building for X-ray crystallography using ARP/wARP version 7. *Nat. Protoc.* *3*, 1171–1179.
- Liebschner, D., Afonine, P. V., Baker, M.L., Bunkoczi, G., Chen, V.B., Croll, T.I., Hintze, B., Hung, L.W., Jain, S., McCoy, A.J., et al. (2019). Macromolecular structure determination using X-rays, neutrons and electrons: Recent developments in Phenix. *Acta Crystallogr. Sect. D Struct. Biol.* *75*, 861–877.
- Linden, J., Koch-Nolte, F., and Dahl, G. (2019). Purine Release, Metabolism, and Signaling in the Inflammatory Response. *Annu. Rev. Immunol.* *37*, 325–347.
- Lü, W., and Du, J. (2020). The N-terminal domain in TRPM2 channel is a conserved nucleotide binding site. *J. Gen. Physiol.* *152*, 2–5.
- Luo, Y., Yu, X., Ma, C., Luo, J., and Yang, W. (2018). Identification of a Novel EF-Loop in the N-terminus of TRPM2 Channel Involved in Calcium Sensitivity. *Front. Pharmacol.* *9*, 1–15.
- Madeira, F., Park, Y.M., Lee, J., Buso, N., Gur, T., Madhusoodanan, N., Basutkar, P., Tivey, A.R.N., Potter, S.C., Finn, R.D., et al. (2019). The EMBL-EBI search and sequence analysis tools APIs in 2019. *Nucleic Acids Res.* *47*, W636–W641.
- Manalastas-Cantos, K., Konarev, P. V., Hajizadeh, N.R., Kikhney, A.G., Petoukhov, M. V., Molodenskiy, D.S., Panjkovich, A., Mertens, H.D.T., Gruzinov, A., Borges, C., et al. (2021). ATSAS 3.0: expanded functionality and new tools for small-angle scattering data analysis. *J. Appl. Crystallogr.* *54*, 343–355.
- Mansoor, S.E., Lü, W., Oosterheert, W., Shekhar, M., Tajkhorshid, E., and Gouaux, E. (2016). X-ray structures define human P2X3 receptor gating cycle and antagonist action. *Nature* *538*, 66–71.
- Martinon, F., Burns, K., and Tschopp, J. (2002). The Inflammasome. *Mol. Cell* *10*, 417–426.
- McCarthy, A.E., Yoshioka, C., and Mansoor, S.E. (2019). Full-Length P2X7 Structures Reveal How Palmitoylation Prevents Channel Desensitization. *Cell* *179*, 659–670.e13.
- McHugh, D., Flemming, R., Xu, S.-Z., Perraud, A.-L., and Beech, D.J. (2003). Critical Intracellular Ca²⁺ Dependence of Transient Receptor Potential Melastatin 2 (TRPM2)

- Cation Channel Activation. *J. Biol. Chem.* 278, 11002–11006.
- McKemy, D.D., Neuhauser, W.M., and Julius, D. (2002). Identification of a cold receptor reveals a general role for TRP channels in thermosensation. *Nature* 416, 52–58.
- McNulty, S., and Fonfria, E. (2005). The role of TRPM channels in cell death. *Pflugers Arch. Eur. J. Physiol.* 451, 235–242.
- Molleman, A. (2002). *Patch Clamping* (Wiley).
- Montell, C. (2003). Mg²⁺ Homeostasis: The Mg²⁺-sensitive TRPM Channels. *Curr. Biol.* 13, 799–801.
- Moreau, C., Kirchberger, T., Swarbrick, J.M., Bartlett, S.J., Fliegert, R., Yorgan, T., Bauche, A., Harneit, A., Guse, A.H., and Potter, B.V.L. (2013). Structure–Activity Relationship of Adenosine 5'-diphosphoribose at the Transient Receptor Potential Melastatin 2 (TRPM2) Channel: Rational Design of Antagonists. *J. Med. Chem.* 56, 10079–10102.
- Mortadza, S.S., Sim, J.A., Stacey, M., and Jiang, L.H. (2017). Signalling mechanisms mediating Zn²⁺-induced TRPM2 channel activation and cell death in microglial cells. *Sci. Rep.* 7, 1–15.
- Mruk, K., Farley, B.M., Ritacco, A.W., and Kobertz, W.R. (2014). Calmodulation meta-analysis: predicting calmodulin binding via canonical motif clustering. *J. Gen. Physiol.* 144, 105–114.
- Nagamine, K., Kudoh, J., Minoshima, S., Kawasaki, K., Asakawa, S., Ito, F., and Shimizu, N. (1998). Molecular Cloning of a Novel Putative Ca²⁺ Channel Protein (TRPC7) Highly Expressed in Brain. *Genomics* 54, 124–131.
- Niebling, S., Burastero, O., Bürgi, J., Günther, C., Defelipe, L.A., Sander, S., Gattkowsky, E., Anjanappa, R., Wilmanns, M., Springer, S., et al. (2021). FoldAffinity: binding affinities from nDSF experiments. *Sci. Rep.* 11, 9572.
- Nikiforov, A., Kulikova, V., and Ziegler, M. (2015). The human NAD metabolome: Functions, metabolism and compartmentalization. *Crit. Rev. Biochem. Mol. Biol.* 50, 284–297.
- North, R.A. (2002). Molecular Physiology of P2X Receptors. *Physiol. Rev.* 82, 1013–1067.
- Ogunbayo, O.A., Zhu, Y., Rossi, D., Sorrentino, V., Ma, J., Zhu, M.X., and Evans, A.M. (2011). Cyclic adenosine diphosphate ribose activates ryanodine receptors, whereas NAADP activates two-pore domain channels. *J. Biol. Chem.* 286, 9136–9140.
- Panjikovich, A., and Svergun, D. (2018). CHROMIXS: automatic and interactive analysis of chromatography-coupled small-angle X-ray scattering data. *Bioinformatics* 34, 1944–1946.
- Park, S.E., Song, J.H., Hong, C., Kim, D.E., Sul, J.-W., Kim, T.-Y., Seo, B.-R., So, I., Kim, S.-Y., Bae, D.-J., et al. (2019). Contribution of Zinc-Dependent Delayed Calcium Influx via TRPC5 in Oxidative Neuronal Death and its Prevention by Novel TRPC Antagonist. *Mol. Neurobiol.* 56, 2836–2837.
- Park, Y.R., Chun, J.N., So, I., Kim, H.J., Baek, S., Jeon, J.-H., and Shin, S.-Y. (2016). Data-driven Analysis of TRP Channels in Cancer: Linking Variation in Gene Expression to Clinical

- Significance. *Cancer Genomics Proteomics* 13, 83–90.
- Partida-Sanchez, S., Gasser, A., Fliegert, R., Siebrands, C.C., Dammermann, W., Shi, G., Mousseau, B.J., Sumoza-Toledo, A., Bhagat, H., Walseth, T.F., et al. (2007). Chemotaxis of Mouse Bone Marrow Neutrophils and Dendritic Cells Is Controlled by ADP-Ribose, the Major Product Generated by the CD38 Enzyme Reaction. *J. Immunol.* 179, 7827–7839.
- Pedersen, S.F., Owsianik, G., and Nilius, B. (2005). TRP channels: An overview. *Cell Calcium* 38, 233–252.
- Pelegrin, P. (2021). P2X7 receptor and the NLRP3 inflammasome: Partners in crime. *Biochem. Pharmacol.* 187, 114385.
- Pelegrin, P., and Surprenant, A. (2006). Pannexin-1 mediates large pore formation and interleukin-1 β release by the ATP-gated P2X7 receptor. *EMBO J.* 25, 5071–5082.
- Pérez, C.A., Huang, L., Rong, M., Kozak, J.A., Preuss, A.K., Zhang, H., Max, M., and Margolskee, R.F. (2002). A transient receptor potential channel expressed in taste receptor cells. *Nat. Neurosci.* 5, 1169–1176.
- Perraud, A.-L., Fleig, A., Dunn, C.A., Bagley, L.A., Launay, P., Schmitz, C., Stokes, A.J., Zhu, Q., Bessman, M.J., Penner, R., et al. (2001). ADP-ribose gating of the calcium-permeable LTRPC2 channel revealed by Nudix motif homology. *Nature* 411, 595–599.
- Pettersen, E.F., Goddard, T.D., Huang, C.C., Couch, G.S., Greenblatt, D.M., Meng, E.C., and Ferrin, T.E. (2004). UCSF Chimera - A visualization system for exploratory research and analysis. *J. Comput. Chem.* 25, 1605–1612.
- Ramsey, I.S., Delling, M., and Clapham, D.E. (2006). An introduction to TRP channels. *Annu. Rev. Physiol.* 68, 619–647.
- Rassendren, F., Buell, G.N., Virginio, C., Collo, G., North, R.A., and Surprenant, A. (1997). The Permeabilizing ATP Receptor, P2X7. *J. Biol. Chem.* 272, 5482–5486.
- Riekehr, W.M., Sander, S., Pick, J., Tidow, H., Bauche, A., Guse, A.H., and Fliegert, R. (2022). cADPR Does Not Activate TRPM2. *Int. J. Mol. Sci.* 23, 3163.
- Roger, S., Pelegrin, P., and Surprenant, A. (2008). Facilitation of P2X7 Receptor Currents and Membrane Blebbing via Constitutive and Dynamic Calmodulin Binding. *J. Neurosci.* 28, 6393–6401.
- Roger, S., Gillet, L., Baroja-Mazo, A., Surprenant, A., and Pelegrin, P. (2010). C-terminal Calmodulin-binding Motif Differentially Controls Human and Rat P2X7 Receptor Current Facilitation. *J. Biol. Chem.* 285, 17514–17524.
- Roger, S., Jelassi, B., Couillin, I., Pelegrin, P., Besson, P., and Jiang, L.-H. (2015). Understanding the roles of the P2X7 receptor in solid tumour progression and therapeutic perspectives. *Biochim. Biophys. Acta - Biomembr.* 1848, 2584–2602.
- Rump, A., Smolander, O.P., Rützel Boudinot, S., Kanellopoulos, J.M., and Boudinot, P. (2020). Evolutionary Origin of the P2X7 C-ter Region: Capture of an Ancient Ballast Domain by a P2X4-Like Gene in Ancient Jawed Vertebrates. *Front. Immunol.* 11, 1–15.
- Samata, A., Hughes, T.E.T., and Moiseenkova-Bell, V.Y. (2018). Transient Receptor Potential (TRP) Channels. In *Membrane Protein Complexes: Structure and Function*, J.R.

- Harris, and E.J. Boekema, eds. (Springer Singapore), pp. 141–166.
- Sander, S., Pick, J., Gattkowski, E., Fliegert, R., and Tidow, H. (2022a). The crystal structure of TRPM2 MHR1/2 domain reveals a conserved Zn²⁺-binding domain essential for structural integrity and channel activity. *Protein Sci.* *31*, 1–12.
- Sander, S., Müller, I., Garcia Alai, M., Nicke, A., and Tidow, H. (2022b). New insights into P2X7 regulation: Ca²⁺-calmodulin and GDP bind to soluble P2X7 ballast domain.
- Sano, Y., Inamura, K., Miyake, A., Mochizuki, S., Yokoi, H., Matsushime, H., and Furuichi, K. (2001). Immunocyte Ca²⁺ Influx System Mediated by LTRPC2. *Science* (80-.). *293*, 1327–1330.
- Scharenberg, A.M. (2005). TRPM2 and TRPM7: channel/enzyme fusions to generate novel intracellular sensors. *Pflügers Arch. - Eur. J. Physiol.* *451*, 220–227.
- Schiewer, M.J., and Knudsen, K.E. (2014). Transcriptional Roles of PARP1 in Cancer. *Mol. Cancer Res.* *12*, 1069–1080.
- Schmitz, C., and Perraud, A.-L. (2005). The TRPM cation channels in the immune context. *Curr. Pharm. Des.* *11*, 2765–2778.
- Sheldrick, G.M. (2008). A short history of SHELX. *Acta Crystallogr. Sect. A Found. Crystallogr.* *64*, 112–122.
- Shen, B.W., Perraud, A.L., Scharenberg, A., and Stoddard, B.L. (2003). The crystal structure and mutational analysis of human NUDT9. *J. Mol. Biol.* *332*, 385–398.
- Simon, F., Varela, D., and Cabello-Verrugio, C. (2013). Oxidative stress-modulated TRPM ion channels in cell dysfunction and pathological conditions in humans. *Cell. Signal.* *25*, 1614–1624.
- Singh, A.K., McGoldrick, L.L., Twomey, E.C., and Sobolevsky, A.I. (2018). Mechanism of calmodulin inactivation of the calcium-selective TRP channel TRPV6. *Sci. Adv.* *4*, 4–9.
- Slater, M., Danieletto, S., Gidley-Baird, A., Teh, L.C., and Barden, J.A. (2004). Early prostate cancer detected using expression of non-functional cytolytic P2X7 receptors. *Histopathology* *44*, 206–215.
- Song, K., Wang, H., Kamm, G.B., Pohle, J., Reis, F. d. C., Heppenstall, P., Wende, H., and Siemens, J. (2016). The TRPM2 channel is a hypothalamic heat sensor that limits fever and can drive hypothermia. *Science* (80-.). *353*, 1393–1398.
- Starkus, J., Beck, A., Fleig, A., and Penner, R. (2007). Regulation of TRPM2 by extra- and intracellular calcium. *J. Gen. Physiol.* *130*, 427–440.
- Sun, Y., Sukumaran, P., Schaar, A., and Singh, B.B. (2015). TRPM7 and its role in neurodegenerative diseases. *Channels* *9*, 253–261.
- Surprenant, A., and North, R.A. (2009). Signaling at Purinergic P2X Receptors. *Annu. Rev. Physiol.* *71*, 333–359.
- Surprenant, A., Rassendren, F., Kawashima, E., North, R.A., and Buell, G. (1996). The Cytolytic P2Z Receptor for Extracellular ATP Identified as a P2X Receptor (P2X7). *Science* (80-.). *272*, 735–738.

- Svergun, D. (1992). Determination of the regularization parameter in indirect-transform methods using perceptual criteria. *J. Appl. Crystallogr.* *25*, 495–503.
- Svergun, D., Koch, M.H.J., Timmins, P.A., and May, R.P. (2013). *Small Angle X-Ray and Neutron Scattering from Solutions of Biological Macromolecules* (Oxford University Press).
- Tan, C.H., and McNaughton, P.A. (2016). The TRPM2 ion channel is required for sensitivity to warmth. *Nature* *536*, 460–463.
- Tidow, H., and Nissen, P. (2013). Structural diversity of calmodulin binding to its target sites. *FEBS J.* *280*, 5551–5565.
- Togashi, K., Hara, Y., Tominaga, T., Higashi, T., Konishi, Y., Mori, Y., and Tominaga, M. (2006). TRPM2 activation by cyclic ADP-ribose at body temperature is involved in insulin secretion. *EMBO J.* *25*, 1804–1815.
- Tong, Q., Zhang, W., Conrad, K., Mostoller, K., Cheung, J.Y., Peterson, B.Z., and Miller, B.A. (2006). Regulation of the Transient Receptor Potential Channel TRPM2 by the Ca²⁺ Sensor Calmodulin. *J. Biol. Chem.* *281*, 9076–9085.
- Tóth, B., and Csanády, L. (2010). Identification of Direct and Indirect Effectors of the Transient Receptor Potential Melastatin 2 (TRPM2) Cation Channel. *J. Biol. Chem.* *285*, 30091–30102.
- Tóth, B., Iordanov, I., and Csanády, L. (2015). Ruling out pyridine dinucleotides as true TRPM2 channel activators reveals novel direct agonist ADP-ribose-2'-phosphate. *J. Gen. Physiol.* *145*, 419–430.
- Tóth, B., Iordanov, I., and Csanády, L. (2020). Selective profiling of N- and C-terminal nucleotide-binding sites in a TRPM2 channel. *J. Gen. Physiol.* *152*, 1–13.
- Uchida, K., and Tominaga, M. (2014). The role of TRPM2 in pancreatic β -cells and the development of diabetes. *Cell Calcium* *56*, 332–339.
- Valera, S., Hussy, N., Evans, R.J., Adami, N., North, R.A., Surprenant, A., and Buell, G. (1994). A new class of ligand-gated ion channel defined by P2X receptor for extracellular ATP. *Nature* *371*, 516–519.
- Varadi, M., Anyango, S., Deshpande, M., Nair, S., Natassia, C., Yordanova, G., Yuan, D., Stroe, O., Wood, G., Laydon, A., et al. (2022). AlphaFold Protein Structure Database: massively expanding the structural coverage of protein-sequence space with high-accuracy models. *Nucleic Acids Res.* *50*, D439–D444.
- Venkatachalam, K., and Montell, C. (2007). TRP channels. *Annu. Rev. Biochem.* *76*, 387–417.
- Vennekens, R., Mesuere, M., and Philippaert, K. (2018). TRPM5 in the battle against diabetes and obesity. *Acta Physiol.* *222*, e12949.
- Vinayagam, D., Quentin, D., Yu-Strzelczyk, J., Sitsel, O., Merino, F., Stabrin, M., Hofnagel, O., Yu, M., Ledebuer, M.W., Nagel, G., et al. (2020). Structural basis of TRPC4 regulation by calmodulin and pharmacological agents. *Elife* *9*, 1–26.
- Di Virgilio, F., Schmalzing, G., and Markwardt, F. (2018). The Elusive P2X7 Macropore.

Trends Cell Biol. 28, 392–404.

Wang, L., Fu, T.-M., Zhou, Y., Xia, S., Greka, A., and Wu, H. (2018). Structures and gating mechanism of human TRPM2. *Science* (80-.). 362, eaav4809.

Wehage, E., Eisfeld, J., Heiner, I., Jüngling, E., Zitt, C., and Lückhoff, A. (2002). Activation of the Cation Channel Long Transient Receptor Potential Channel 2 (LTRPC2) by Hydrogen Peroxide. *J. Biol. Chem.* 277, 23150–23156.

Wehrhahn, J., Kraft, R., Harteneck, C., and Hauschildt, S. (2010). Transient Receptor Potential Melastatin 2 Is Required for Lipopolysaccharide-Induced Cytokine Production in Human Monocytes. *J. Immunol.* 184, 2386–2393.

Wilson, H.L., Wilson, S.A., Surprenant, A., and North, R.A. (2002). Epithelial Membrane Proteins Induce Membrane Blebbing and Interact with the P2X7 Receptor C Terminus. *J. Biol. Chem.* 277, 34017–34023.

Winkler, P.A., Huang, Y., Sun, W., Du, J., and Lü, W. (2017). Electron cryo-microscopy structure of a human TRPM4 channel. *Nature* 552, 200–204.

Wood, W.B. (1966). Host specificity of DNA produced by *Escherichia coli*: Bacterial mutations affecting the restriction and modification of DNA. *J. Mol. Biol.* 16, 118–133.

Wright, D.J., Simmons, K.J., Johnson, R.M., Beech, D.J., Muench, S.P., and Bon, R.S. (2020). Human TRPC5 structures reveal interaction of a xanthine-based TRPC1/4/5 inhibitor with a conserved lipid binding site. *Commun. Biol.* 3, 704.

Yamaguchi, S., Tanimoto, A., Iwasa, S., and Otsuguro, K. (2019). TRPM4 and TRPM5 Channels Share Crucial Amino Acid Residues for Ca²⁺ Sensitivity but Not Significance of PI(4,5)P₂. *Int. J. Mol. Sci.* 20, 2012.

Yamamoto, S., Shimizu, S., Kiyonaka, S., Takahashi, N., Wajima, T., Hara, Y., Negoro, T., Hiroi, T., Kiuchi, Y., Okada, T., et al. (2008). TRPM2-mediated Ca²⁺ influx induces chemokine production in monocytes that aggravates inflammatory neutrophil infiltration. *Nat. Med.* 14, 738–747.

Yan, Z., Li, S., Liang, Z., Tomić, M., and Stojilkovic, S.S. (2008). The P2X7 Receptor Channel Pore Dilates under Physiological Ion Conditions. *J. Gen. Physiol.* 132, 563–573.

Yang, W., Manna, P.T., Zou, J., Luo, J., Beech, D.J., Sivaprasadarao, A., and Jiang, L.H. (2011). Zinc inactivates melastatin transient receptor potential 2 channels via the outer pore. *J. Biol. Chem.* 286, 23789–23798.

Ye, M., Yang, W., Ainscough, J.F., Hu, X.-P., Li, X., Sedo, A., Zhang, X.-H., Zhang, X., Chen, Z., Li, X.-M., et al. (2014). TRPM2 channel deficiency prevents delayed cytosolic Zn²⁺ accumulation and CA1 pyramidal neuronal death after transient global ischemia. *Cell Death Dis.* 5, e1541.

Yin, Y., Wu, M., Zubcevic, L., Borschel, W.F., Lander, G.C., and Lee, S.-Y. (2018). Structure of the cold- and menthol-sensing ion channel TRPM8. *Science* (80-.). 359, 237–241.

Yin, Y., Wu, M., Hsu, A.L., Borschel, W.F., Borgnia, M.J., Lander, G.C., and Lee, S.-Y. (2019a). Visualizing structural transitions of ligand-dependent gating of the TRPM2 channel. *Nat. Commun.* 10, 3740.

- Yin, Y., Le, S.C., Hsu, A.L., Borgnia, M.J., Yang, H., and Lee, S.-Y. (2019b). Structural basis of cooling agent and lipid sensing by the cold-activated TRPM8 channel. *Science* (80-.). 363.
- Yu, P., Xue, X., Zhang, J., Hu, X., Wu, Y., Jiang, L.-H., Jin, H., Luo, J., Zhang, L., Liu, Z., et al. (2017). Identification of the ADPR binding pocket in the NUDT9 homology domain of TRPM2. *J. Gen. Physiol.* 149, 219–235.
- Yu, P., Liu, Z., Yu, X., Ye, P., Liu, H., Xue, X., Yang, L., Li, Z., Wu, Y., Fang, C., et al. (2019). Direct Gating of the TRPM2 Channel by cADPR via Specific Interactions with the ADPR Binding Pocket. *Cell Rep.* 27, 3684-3695.e4.
- Yu, X., Xie, Y., Zhang, X., Ma, C., Liu, L., Zhen, W., Xu, L., Zhang, J., Liang, Y., Zhao, L., et al. (2021). Structural and functional basis of the selectivity filter as a gate in human TRPM2 channel. *Cell Rep.* 37, 110025.
- Zhang, H., Zhao, S., Yu, J., Yang, W., Liu, Z., and Zhang, L. (2020). Medicinal chemistry perspective of TRPM2 channel inhibitors: where we are and where we might be heading? *Drug Discov. Today* 25, 2326–2334.
- Zhang, Z., Tóth, B., Szollosi, A., Chen, J., and Csanády, L. (2018). Structure of a TRPM2 channel in complex with Ca²⁺ explains unique gating regulation. *Elife* 7, 1–22.
- Zheng, H., Cooper, D.R., Porebski, P.J., Shabalín, I.G., Handing, K.B., and Minor, W. (2017). CheckMyMetal: a macromolecular metal-binding validation tool. *Acta Crystallogr. Sect. D, Struct. Biol.* 73, 223–233.
- Zocchi, E., Franco, L., Guida, L., Benatti, U., Bargellesi, A., Malavasi, F., Lee, H.C., and Deflora, A. (1993). A Single Protein Immunologically Identified as CD38 Displays NAD⁺ Glycohydrolase, ADP-Ribosyl Cyclase and Cyclic ADP-Ribose Hydrolase Activities at the Outer Surface of Human Erythrocytes. *Biochem. Biophys. Res. Commun.* 196, 1459–1465.

7 SAFETY AND DISPOSAL

All chemicals that were used during the experimental work for this thesis were handled and disposed according to their GHS safety and precautionary statements. Contaminated waste and solvents were stored in designated canisters and disposed according to the safety instructions. Genetically modified organisms and the related liquid as well as solid waste was autoclaved for 20 minutes at 121°C and 5 bar according to the German “Gentechnikgesetz” before disposal. All experiments for this thesis with genetically modified organisms were approved and performed under biosafety level 1 (BSL1) regulations. All hazardous and toxic chemicals that were used within this study are listed in Table 7.1 with their GHS hazard symbols, hazard statements and precautionary statements.

Table 7.1: Hazardous and toxic chemicals. Compounds are listed alongside their CAS numbers and safety information.

Compound	CAS-No.	GHS hazard	Hazard statements	Precautionary statements
Chloramphenicol	56-75-7	GHS06, GHS08	H318, H351, H361	P202, P280, P305 + P351 + P338, P308 + P313
2-Mercapto ethanol	60-24-2	GHS06, GHS09	H302, H411, H315, H335, H311, H319	P280, P312, P302 + 350, P261, P273, P301 + 312, P305 + 351 + 338
Acetic acid, 96 %	64-19-7	GHS02, GHS05	H226, H314	P280, P305 + 351 + 338, P310
ADPR sodium salt	68414-18-6	GHS07	H315, H319, H335	P261, P305 + P351 + P338
Ampicillin	69-52-3	GHS08	H317, H334	P280, P261, P302 + 352, P342 + P311
Boric acid (H ₃ BO ₃)	10043-35-3	GHS08	H360FD	P201, P308 + P313
CaCl ₂	10043-52-4	GHS07	H319	P305 + P351 + P338

Compound	CAS-No.	GHS hazard	Hazard statements	Precautionary statements
CoCl ₂	7791-13-1	GHS07, GHS08, GHS09	H302, H317, H334, H341, H350i, H360F, H410	P273, P280, P301 + P312, P302 + P352, P304 + P340 + P312, P308 + P313
CuCl ₂	10125-13-0	GHS05, GHS07, GHS09	H302 + H312 - H315, H318, H410	P264, P273, P280, P301 + P312, P302 + P352 + P312, P305 + P351 + P338
CuSO ₄	7758-98-7	GHS07, GHS09	H302, H315, H319, H410	P264, P270, P273, P301 + P312, P302 + P352, P305 + P351 + P338
DTT	578517	GHS07	H302, H315, H319, H335	P302 + P352, P305 + P351 + P338
EDTA	60-00-4	GHS07	H319	P305 + P351 + P338
Ethanol	64-17-5	GHS02	H225	P210
FeCl ₃	7705-08-0	GHS05, GHS07	H290, H302, H315, H318	P234, P264, P280, P301 + P312, P302 + P352, P305 + P351 + P338
Gentamicin-sulfate	1405-41-0	GHS08	H317, H334	P261, P280, P284, P272, P302 + P352, P333 + P313, P342 + P311, P362 + P364, P304 + P340, P501
HCl, 36 %	7647-01-0	GHS05, GHS07	H290, H314, H335	P280, P303 + P361 + P353, P305 + P351 + P338 + P310
Imidazole	288-32-4	GHS05, GHS06, GHS08	H301, H314, H361	P260, P281, P303 + P361 + P353, P301 + P330 + P331, P305 + P351 + P338, P308 + P313
Isopropanol	67-63-0	GHS02, GHS07	H225, H319, H336	P210, P233, P305 + P351 + P338
Kanamycin-sulfate	25-389-04-0	GHS08	H360	P201, P308 + P313

Compound	CAS-No.	GHS hazard	Hazard statements	Precautionary statements
KOH	1310-58-3	GHS05, GHS07	H290, H302, H314	P260, P280, P301 + P312 + P330, P303 + P361 + P353, P304 + P340 + P310, P305 + P351 + P338
Seleno- Methionine	3211-76-5	GHS06, GHS08, GHS09	H301 + H331, H373, H410	P260, P264, P273, P301 + P310, P304 + P340, P330
Methanol	67-56-1	GHS02, GHS06, GHS08	H225, H301 + H311 + H331, H370	P210, P280, P302 + P352 + P312, P304 + P340 + P312, P370 + P378, P403 + P235
MnCl ₂	7773-01-5	GHS02, GHS06	H301, H318, H373, H411	P273, P280, P301 + P310 + P330, P305 + P351 + P338 + P310, P314
NaOH	1310-73-2	GHS05	H290, H314	P260, P280, P303 + P361 + P353, P304 + P340 + P310, P305 + P351 + P338
NH ₄ Cl	12125-02-9	GHS07	H302, H319	P301 + P312 + P330, P305 + P351 + P338
Penicillin- Streptomycin	-	GHS07	H315, H317, H334, H335	P280, P261, P264, P284, P271, P302 + P352, P333 + P313, P304 + P340, P342 + P311, P312, P403 + P233, P501
PMSF	329-98-6	GHS05, GHS06	H301, H314	P260, P264, P270, P280, P304 + P340, P301 + P310, P311, P305 + P351 + P338, P301 + P330 + P331, P303 + P361 + P353, P363,
SDS	151-21-3	GHS02, GHS06	H228, H302, H311, H315, H319, H335	P210, P261, P280, P312, P305 + P351 + P338

Compound	CAS-No.	GHS hazard	Hazard statements	Precautionary statements
Tetracycline	60-54-8	GHS07, GHS08	H319, H361	P201, P202, P264, P280, P305 + P351 + P338, P308 + P313, P337 + P313, P501
Triton X-100	9002-93-1	GHS05, GHS07, GHS09	H302, H318, H411	P270, P273, P280, P305 + P351 + P338, P310
Trypsin	9002-07-7	GHS07, GHS08	H315, H319, H334, H335	P261, P280, P284, P304 + P340, P337 + P313, P342 + P311
Uranyl formate	16984-59-1	GHS06, GHS07	H301 +H331	P280, P280A, P285, P301A, P302 + P352, P340, P351
ZnCl ₂	7646-85-7	GHS05, GHS07, GHS09	H302, H314, H410	P260, P273, P280, P301 + P330 + P331, P303 + P361 + P353, P305 + P351 + P338
ZnSO ₄ heptahydrate	7446-20-0	GHS05, GHS07, GHS09	H302, H318, H410	P273, P280, P305 + P351 + P338, P501
X-Gal	7240-90-6	GHS07	H302, H312, H332	P301 + P330 + P331, P302 + P 352

ABSTRACT (DEUTSCH)

Die Ionenkanäle TRPM2 (*Transient Receptor Potential Melastatin 2*) und P2X7 (*P2X Purinoreceptor 7*) spielen Schlüsselrollen in Immunitätsreaktionen und Entzündungsprozessen. Beide werden durch Adenin-Nukleotide aktiviert: TRPM2 durch Adenosindiphosphat-Ribose (ADPR) und P2X7 durch Adenosintriphosphat (ATP).

TRPM2 ist maßgeblich am intrazellulären Ca^{2+} -Signaling beteiligt und enthält zwei Nukleotid-Bindungsdomänen: Die N-terminale MHR1/2-Domäne (*TRPM homology region 1/2*) mit einer konservierten ADPR-Bindungsstelle und die C-terminale NUDT9-H-Domäne (*NUDT9 homology*), welche in verschiedenen TRPM2-Orthologen unterschiedliche Funktionen hat. Die zugrunde liegenden Mechanismen sind nicht gänzlich geklärt.

In dieser Dissertation wurden beide Domänen in isolierter, löslicher Form exprimiert, gereinigt und biophysikalisch charakterisiert. Weitere Experimente mit MHR1/2 aus Zebrafisch-TRPM2 (*drMHR1/2*) zeigten, dass die ADPR-Derivate 2'-desoxy-ADPR (ein Superagonist von menschlichem TRPM2) und 8-Br-ADPR (ein Antagonist von menschlichem TRPM2) an die isolierte Domäne binden, cADPR (*cyclic ADPR*) und 8-Br-cADPR jedoch nicht, obwohl Interaktionen beider zyklischen Substanzen mit TRPM2 zuvor diskutiert worden waren. Die Ergebnisse zeigten außerdem, dass 2'-desoxy-ADPR kein Superagonist von Zebrafisch-TRPM2 ist. Mithilfe einer Kristallstruktur von isoliertem *drMHR1/2* wurde eine neue Zn^{2+} -Bindestelle identifiziert, die innerhalb der TRPM-Familie konserviert und für die strukturelle Integrität und Funktion von TRPM2 essenziell ist, worauf elektrophysiologische Experimente hindeuteten. Darüber hinaus wurde gezeigt, dass Calmodulin (CaM) an *drMHR1/2* bindet, was ein bekanntes *IQ-like* Bindemotiv von menschlichem TRPM2 bestätigt.

P2X7 ist essenzieller Bestandteil der purinerger Signaltransduktion und umfasst eine einzigartige C-terminale Ballast-Domäne (P2X7BD), die für die zytotoxische Wirkung des Rezeptors entscheidend ist, aber nicht an der Kanal-Aktivierung beteiligt ist. Das Zusammenspiel mit den Liganden GDP (Guanosindiphosphat) und CaM, sowie die modulierende Rolle für die P2X7-Funktion sind nicht vollständig verstanden.

In dieser Arbeit wurden durch einen peptidbasierten Bindungsansatz zwei mutmaßliche CaM-bindende Regionen innerhalb von P2X7BD identifiziert und es wurde gezeigt, dass isoliertes menschliches P2X7BD Ca^{2+} -CaM bindet. Während diese Wechselwirkung die Domäne destabilisierte und ihren trimeren Zustand auflöste, wie durch SAXS gezeigt wurde, stabilisierte GDP P2X7BD. Dies deutet darauf hin, dass beide Liganden in einem Gleichgewicht reversibel an die isolierte Domäne binden, was eine mögliche Grundlage für die Regulierung des P2X7-Rezeptors bildet.

Insgesamt haben die Ergebnisse dieser Dissertation neue Eigenschaften wichtiger Liganden-Bindungsdomänen von TRPM2 und P2X7 offenbart, was Raum für weiterführende Forschung hinsichtlich funktioneller Implikationen für die jeweiligen Vollängen-Kanäle bietet.

DANKSAGUNG

Allen voran möchte ich mich bei meinem Doktorvater Henning bedanken. Seine Art der Betreuung hat mir immer genug Freiraum geboten, ohne dass ich mich jemals allein gelassen gefühlt habe. Ich glaube, von seinem Zeitmanagement, seiner Begeisterung für die Wissenschaft und seinen Führungsqualitäten können sich einige Gruppenleiter/innen eine Scheibe abschneiden.

Neben Henning war die gesamte AG Tidow immer für mich da. Auch wenn die Gruppe immer kleiner wurde, der fachliche/experimentelle Input wird wohl immer als Paradebeispiel für gute Zusammenarbeit in meinem Kopf bleiben. Und ganz nebenbei sind noch einige ziemlich gute Freundschaften dabei rumgekommen, inklusive dem einen oder anderen Beer-Friday, der auch mal auf dem Kiez enden konnte... Danke an Kesha, Ellen, Katha, Anne, Dominique, Katharina, Yasser und meine beiden Masterstudierenden Hanna und Jonas!

Ich möchte mich bei Ralf für seinen Input hinsichtlich der Patch-Clamp-Experimente bedanken. Außerdem hat er mich immer wieder mit seinem TRPM2-Wissen beeindruckt. Wenn jemand alle Hintergründe verstanden hat, dann er. Auch seine Gruppe am UKE hat mich immer unterstützt, danke vor allem an Jelena, Winnie und Max!

Annette Nicke und ihre Gruppe an der LMU München, vor allem Isabel Müller, waren maßgeblich am P2X7-Projekt beteiligt, vielen Dank dafür. Sönke von der Massenspektrometrie-Core-Facility am UKE war immer ein unkomplizierter Ansprechpartner bei allen MS-Analysen. Ebenso alle Mitarbeiter der EMBL SPC-, SAXS- und Kristallografie-Teams, ohne deren technische Hilfe viele Experimente nicht möglich gewesen wären.

Zuletzt sind da natürlich meine Familie, Freunde und Bastian. Ob beim Frühstück in Bad Oldesloe mit Mama, Papa und Christin, beim Ultramotivierten-Stammtisch mit Basti, Tess, Moataz, Greta, Anna und Rike, beim Badminton mit Mehran, Moritz und Tim oder beim Chor-Stammtisch mit Carlotta, Maxi, Silke und Anna, ohne euren Rückhalt wäre das hier wirklich nicht möglich gewesen! ♥

Danke!

EIDESSTATTLICHE VERSICHERUNG

Hiermit versichere ich an Eides statt, die vorliegende Dissertation selbst verfasst und keine anderen als die angegebenen Hilfsmittel benutzt zu haben. Die eingereichte schriftliche Fassung entspricht der elektronisch übermittelten PDF-Datei. Ich versichere, dass diese Dissertation nicht in einem früheren Promotionsverfahren eingereicht wurde.

Hamburg, 18.05.2022

A handwritten signature in black ink, consisting of a series of loops and a long horizontal stroke at the end.